

2019 ▶ 02

April Volume 2 Issue 2
ISSN 2630-5119 (Online)

Journal of Atmospheric Science Research



**BILINGUAL
PUBLISHING CO.**

Pioneer of Global Academics Since 1984

Editor-in-Chief

Dr. José Francisco Oliveira Júnior

ICAT/ UFAL, Brazil

Editorial Board Members

Fan Ping, China	Sarvan Kumar, India
Marko Ekmedzic, Germany	Abderrahim Lakhout, Canada
Xuezhi Tan, China	B.T. Venkatesh Murthy, India
Hirdan Katarina de Medeiros Costa, Brazil	Olusegun Folarin Jonah, United States
Chuanfeng Zhao, China	Amos Apraku, South Africa
Suleiman Alsweiss, United States	Foad Brakhasi, Iran
Aditi Singh, India	Debashis Nath, India
Boris Denisovich Belan, Russian Federation	Chian-Yi Liu, Taiwan
Perihan Kurt-Karakus, Turkey	Mohammad Moghimi Ardekani, South Africa
Hongqian Chu, China	Yuzhu Wang, China
Isidro A. Pérez, Spain	Zixian Jia, France
Mahboubeh Molavi-Arabshahi, Iran	Md. Mosarraf Hossain, India
Tolga Elbir, Turkey	Prabodha Kumar Pradhan, India
Junyan Zhang, United States	Tianxing Wang, China
Thi Hien To, Vietnam	Bhaskar Rao Venkata Dodla, India
Jian Peng, United Kingdom	Lingling Xie, China
Zhen Li, United Kingdom	Kazi Sabiruddin, India
Anjani Kumar, India	Nicolay Nikolayevich Zavalishin, Russian Federation
Bedir Bedir Yousif, Egypt	Xizheng Ke, China
assan Hashemi Hassan Hashemi, Iran	Alexander Ruzmaikin, United States
Mengqian Lu, Hong Kong	Peng Si, China
Lichuan Wu, Sweden	Zhaowu Yu, Denmark
Raj Kamal Singh, United States	Manish Kumar Joshi, United Kingdom
Zhiyong Ding, China	Aisulu Tursunova, Kazakhstan
Elijah Olusayo Olurotimi, South Africa	Enio Bueno Pereira, Brazil
Jialei Zhu, United States	Samia Tabassum, Bangladesh
Xiying Liu, China	Donglian Sun, United States
Naveen Shahi, South Africa	Zhengqiang Li, China
Netrananda Sahu, India	Haider Abbas Khwaja, United States
Luca Aluigi, Università di Modena e Reggio Emilia	Haikun Zhao, China
Daniel Andrade Schuch, Brazil	Wen Zhou, Hong Kong
Vladislav Vladimirovich Demyanov, Russian Federation	Suman Paul, India
Jingsong Li, China	Katta Vijaya Kumar, Sri Venkateswara University
Priya Murugasen, India	Mohammed Adnane Douar, Algeria
Nathaniel Emeka Urama, Nigeria	Chunju Huang, China
Barbara Małgorzata Sensuła, Poland	Habibah Lateh, Malaysia
Service Opare, Canada	Meng Gao, China
Che Abd Rahim Bin Mohamed, Malaysia	Bo Hu, China
Maheswaran Rathinasamy, India	Akhilesh Kumar Yadav, India
Masoud Rostami, Germany	Archana Rai, India
Oswaldo Luiz Leal De Moraes, Brazil	Pardeep Pall, Norway
Ranis Nail Ibragimov, United States	Upaka Sanjeewa Rathnayake, Sri Lanka
Masoud Masoudi, Iran	Yang Yang, New Zealand
Pallav Purohit, Austria	Somenath Dutta, India
B. Yashwansingh Surnam, Mauritius	Kuang Yu Chang, United States
Alexander Kokhanovsky, Germany	Sen Chiao, United States
Lucas Lavo Antonio Jimo Miguel, Mozambique	Mohamed El-Amine Slimani, Algeria
Nastaran Parsafard, Iran	

Volume 2 Issue 2 • April 2019 • ISSN 2630-5119 (Online)

Journal of Atmospheric Science Research

Editor-in-Chief

Dr. José Francisco Oliveira Júnior



**BILINGUAL
PUBLISHING CO.**

Pioneer of Global Academics Since 1984

Contents

Article

- 1 **Main Characteristics of Dust Storm sand Their Radiative Impacts: With a Focuson Tajiki-
stan**
Sabur.F.Abdullaev, Irina.N.Sokolik
- 22 **Land-use Changes Alter Energy and Water Balances on an African BrachiariaPasture
Replacing a Native Savanna in the Orinoco llanos**
José San-José, Rubén Montes, Rafael Herrera, Jair M. Maia, Nina Nikonova
- 37 **Climatology of Winter Extratropical Cyclones over the Coastal Waters of China**
Naru Xie, Meng Gao, Zhiqiang Gao
- 51 **Microbial Community Diversity and Vertical Distribution in a Columnar Sediment of
Maluku Strait**
Yan Wang, Fuchao Li, Jin Zhao, Huaxin Chen, Peng Jiang, Xuexi Tang

Review

- 46 **Exploration and Research on Fault Maintenance System of New Generation Weather
Radar**
Haitao Yan

Copyright

Journal of Atmospheric Science Research is licensed under a Creative Commons-Non-Commercial 4.0 International Copyright (CC BY- NC4.0). Readers shall have the right to copy and distribute articles in this journal in any form in any medium, and may also modify, convert or create on the basis of articles. In sharing and using articles in this journal, the user must indicate the author and source, and mark the changes made in articles. Copyright © BILINGUAL PUBLISHING CO. All Rights Reserved.



ARTICLE

Main Characteristics of Dust Storms and Their Radiative Impacts: With a Focus on Tajikistan

Sabur.F.Abdullaev^{1*} Irina.N.Sokolik²

1. Physical-Technical institute Academy of Sciences of Republic of Tajikistan, Ayni str.299/1, Dushanbe, ZIP-734063, Tajikistan

2. School of Earth and Atmospheric Sciences Georgia Institute of Technology, Atlanta, 311 Ferst Drive Atlanta, GA 30332-0340, USA

ARTICLE INFO

Article history

Received: 11 November 2018

Accepted: 6 April 2019

Published Online: 12 April 2019

Keywords:

Dust storms

Dust haze

Temperature effect of aerosol

Aerosol optical thickness

Desert zone

Arid zone

Dust aerosol

ABSTRACT

Dust storms are commonly occurring phenomena in Tajikistan. The known aridity of the region is a major factor in promoting numerous dust storms. They have many diverse impacts on the environment and the climate of the region. The classification of dust storms and synoptic conditions related to their formation in Central Asia are discussed in the content of their diverse impact. We address dust optical properties that are representative of the region. Dust storms significantly reduce visibility and pose a human health threat. They also cause a significant impact on the radiative regime. As a result, dust storms may cause a decrease in temperature during daytime of up to 16 °C and an increase in temperature during night time from up to 7 °C compared to a clear day.

1. Introduction

Tajikistan is situated in the global dust belt on the way of transport routes of dust from some major dust sources like the Aralkum desert of the desiccating Aral Sea, the Kyzyl-Kum and Karakum deserts east of the Caspian Sea, the Iranian Dasht-e-Kavir and Dasht-e-Lut deserts and the deserts in Afghanistan, Sahara and Taklamakan desert^[1-4] (Figure 1). Therefore, Tajikistan is frequently affected by severe dust events every year (from April until November) and is a net accumulator of dust. Tajikistan is a country with a dry climate and benefits

from its water resources in the mountainous Pamir region, which are stored in a large part in glaciers. Furthermore, Central Asia and especially Tajikistan are highly affected by climate change. For example, the dramatic glacier shrinking took place in the last decades, which has also an effect on the water resources of Tajikistan and the whole Central Asian area. Since the trans-regionally important rivers as Amu Darya and Syr Darya are fed by glacier melt water, which were originally feeding the Aral Sea, which now became itself a strong dust source^[1-4]. On the other hand, deposited dust itself can accelerate glacier

*Corresponding Author:

Sabur.F.Abdullaev,

Physical-Technical institute Academy of Sciences of Republic of Tajikistan, Ayni str.299/1, Dushanbe, ZIP-734063, Tajikistan;

Email: sabur.f.abdullaev@gmail.com

melt by altering the glacier's surface albedo^[3].



Figure 1. Geographical map with desert regions (black text), dust belt (bright green dotted line), measurement site in Dushanbe, Tajikistan (red text) highlighted (<http://naturalearth.springercarto.com>, adapted)^[4]

It should be noted that in the period up to 1990th (September 20, 1989 to October 15, 1990), predominantly strong dust storms with the subsequent precipitations were observed. These dust storms had a duration of 6-8 hours and were accompanied by a decrease in the horizontal visual range down to 50 meters^[5,6].

After 1990s, the duration of dust hazes increased to 3 to 8 days (sometimes for a week). They often created a pulsating change in the range of the horizontal visibility, and, most importantly, were not accompanied by a precipitation. In the summer-autumn period of 2001 dust hazes reached the record frequency. It occurred almost daily with 29 days of dust haze stay in Dushanbe city between July-August. On November of 2007 (from 8 to 24), the dust haze covered the whole territory of southern Tajikistan. Sometimes, the horizontal visibility was less than 200-500 m. In August 2008 (from 4 to 15), and August of 2009 (from 25 to 29), pulsating dust episodes were observed, causing a deterioration of the horizontal visual range down to 200 meters. Often after prolonged dust haze episodes, dust particles were deposited on the ground without any precipitation. These deposits result in very high pollution levels in the surface layer^[6]. Thus, it is important to study dust storms in Tajikistan that provide the motivation for this work. The goal of this paper is to provide a comprehensive characterization of dust storms in Tajikistan by linking the environmental conditions, dust properties, and dust diverse impacts.

Aerosol plays an important role in the formation of weather and climate, both regionally and globally. Aerosol is frequently generated by dust storms (DS) in the atmosphere of the arid zone. The fine particle fraction (with a diameter $<1 \mu\text{m}$) may be transported with the air flow far enough away from the source and it may remain long time in the atmosphere. Atmospheric dust is the aerosol, which significantly absorbs solar radiation and also interact with

thermal radiation^[7]. The extent of the observed effects is determined by the microphysical properties of dust particles, namely, by their complex refractive index, particle size distribution, shape, density, and their total concentration in the atmosphere that all control the dust optical properties and dust radiative impacts.

The fine particle fraction (with a diameter $<1 \mu\text{m}$) may be transported with the air flow far enough away from the source and it may remain long time in the atmosphere. Atmospheric dust is the aerosol, which significantly absorbs solar radiation and also interact with thermal radiation^[7]. The nature of the observed effects is determined by the microphysical properties of dust particles, namely, by their complex refractive index, particle size distribution, shape, density, and their total concentration in the atmosphere that all control the dust optical properties and dust radiative impacts.

Depending on the concentration of dust and its vertical profile, time, and duration of the residence of dust in the atmosphere, it may have diverse effects on the air temperature and the land surface vegetation^[7-12]. For particle sizes of the order of a few micron or less, which determine the opacity of the dust storms or dusty haze, the visible radiation is absorbed stronger than thermal^[11,13]. Therefore, in the afternoon we can expect a decrease in the surface temperature under dusty atmosphere conditions, and at night - a warming in the comparison with normal conditions, since the thermal radiation from the surface will be partially absorbed by a dusty atmosphere and reradiated back. Dust can increase the albedo of the system^[8-11].

One of the effective way of determining the optical characteristics of atmospheric aerosol is a photo metric method of direct and diffuse solar radiation. Currently, the most advanced system in the automation of the measurement efficiency of obtaining data and global coverage is network of AERONET aerosol observations (<http://aeronet.gsfc.nasa.gov>)^[14]. In Dushanbe, the study of the AOT (aerosol optical thickness) of atmosphere using the AERONET program was held in July 2010 in the regular mode measurements by the AERONET network with the support of collaborators from the United States, France, and Portugal^[13].

For this research the data were taken from the archive of Agency on Hydrometeorology of Tajikistan and website www.r5.ru.

https://rp5.ru/Weather_in_Dushanbe ;

https://rp5.ru/Weather_in_Termez ;

https://rp5.ru/Weather_in_Repetek ;

https://rp5.ru/Weather_in_Bayramaly ;

[https://rp5.ru/Weather_in_Qurghonteppa_\(airport\)](https://rp5.ru/Weather_in_Qurghonteppa_(airport)) ;

2. Classification of Dust Storms and Synoptic Conditions Related to Their Formation in Central Asia

A dust storm is a phenomenon of strong gusty winds that bring into the air large amounts of dust, sand and other particles that are then suspended in the air, causing a decrease in a horizontal visibility down to from 1-2 km to several hundred meters ^[12,15]. In Central Asia (CA), the main centers of dust storms are the Kyzylkum desert and the Karakum desert. In Tajikistan, dust storms occur most frequently in southern valleys of the Lower Kafirnigan, Vakhsh, Kyzyl-Su, and Yakhsu ^[16].

A dusty haze is a phenomenon, in which solid particles are suspended in the air and the horizontal visibility is limited to 2-4 km. Dust particles can travel hundreds and even thousands kilometers from the point of their initiation during dust storms. In the case of the turbulent state of the atmosphere, dust can be transported to the heights of 3-4 km, and more. The thickness of the layer of dust haze depends on the wind speed and the vortex structure. Ascending air currents lead to dust haze being lifted up to 5-7 km.

The initiation and spread of dust storms depend on the following two conditions: the presence of suitable materials (dust, sand) and strong winds, which capable to carry particles horizontally and vertically. Favorable conditions for dust storm are created by prolonged dry periods, the presence of loess soils in the foothills, loose sand in the desert, and frequent gales. In Tajikistan, especially the strong dust storm or the so-called "Afghan" occurs in warm seasons (June-September).

The Kyzyl-Kum Desert, Karakum Desert and Aral-Kum are known local sources of dust in the Central Asian region.

The Kyzylkum Desert is the 11th largest desert in the world. Its name means "red sand" in Uzbek and Kazak languages. The desert is located in Central Asia in the flood plain between the rivers Amu Darya and Syr Darya, and is divided between Kazakhstan, Uzbekistan, and Turkmenistan. The desert occupies about 298000 square kilometers.

The Karakum Desert) occupies about 70%, or the 350000 km² area of Turkmenistan. The desert located to the east of the Caspian Sea, with the Aral Sea in the north and the Amu Darya River and the Kyzylkum desert in the north-east. The Murghab River and Tedjen River flow from Hindu Kush Mountains in the south and through the desert, providing water for irrigation purposes. The largest irrigation canal in the world is the Karakum Canal that crosses the desert.

An additional source of dust, the Aral Sea, arose in the last quarter of the last century. During the hot season (June-September), the surface is heated by the solar radiation. The moisture evaporates and the upper layer of soil is converted into a friable mass of sand, which is capable of moving by winds, and transferring the fine material from the surface into the atmosphere. Strong winds, especially in the summer, often form dust storms. Note that dust, salt, and sand storms cause extensive ecological and economic damages, especially to the vegetation, agricultural lands, and industrial facilities. They also pose a serious health threat.

It is advisable to consider first not the genetic classification of dust storms (DS), which is rather difficult, but a classification according to some external features. From the point of view of the duration of dust storms and visibility, they ^[17] propose the following main types:

(1) Short-term dust storms with a relatively small deterioration in the visibility. Their duration often does not exceed several minutes, very often these are dust storms caused by purely local wind features.

(2) Short-term dust storms with a strong deterioration in the visibility. The duration of these dust storms are the same as the first type, but they can cause a drop in the visibility to one kilometer, and sometimes less than a kilometer (to 100 - 200 m) ^[17].

(3) Long-lasting and pulsating dust storms with a relatively small deterioration of the visibility (2-4 or more kilometers) ^[17]. Dust storms can last for several hours or even days and are generated by stable pressure fields with large horizontal gradients. Particularly dangerous and difficult the dust storms with pulsating visibility.

(4) Long-lasting severe dust storms with a large deterioration of the visibility (1 - 2 km or less). These are the most dangerous dust storms when you consider that they usually have a greater vertical power ^[17].

(5) Dusty or sandy storms drifts represent the phenomenon of the transfer of dust and sand in a layer not more than 2 m from the soil surface. In general, dust drifting in its pure form is extremely rare ^[17].

Dust storm (dust haze) leads to a decrease in the horizontal visibility range. To determine the degree of a reduction of the horizontal visibility range, weather conditions with a relative humidity of less than 50% were chosen, which is typical of the situation associated with DH in Tajikistan. Figure 2 shows the frequency of the horizontal visibility range (in%) is less than 1 km and 10 km in Dushanbe for the period 1950-2014. As one can see, after the 1970s, aerosol pollution associated with dust storms prevails in the atmosphere.

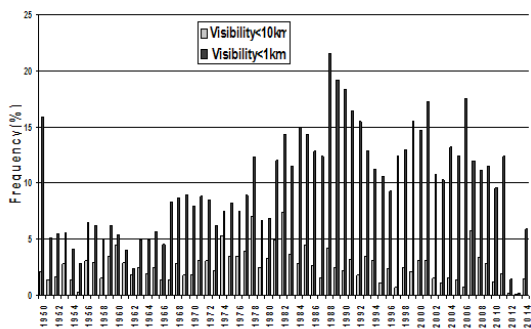


Figure 2. The frequency of repeat ability of the horizontal visibility range (in%) is less than 1 km and less than 10 km in Dushanbe city for the period 1950-2014

A long rainless period of summer months in Central Asia and in the foreign territory adjacent to it leads to a strong degradation of the soil surface, as a result of which DS can occur even at low wind speeds (7-10 m / s). If the air mass, moving over the Central Asian deserts, loses contrast in the surface air layer and atmospheric fronts pass through the territory of Tajikistan in a weakened form, then dust storms do not occur. However, dust, reaching a vertical height of 5 km (Figure 3) [5], even from remote sources of DS, can be brought into the territory of Tajikistan in the form of the dust haze (DH) from the desert zone (Figure 4) [5].

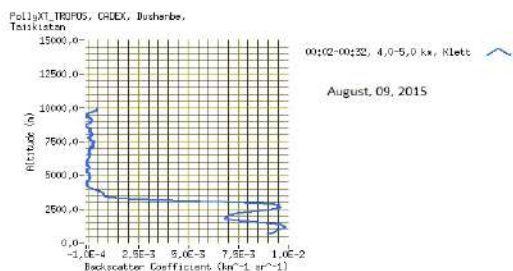


Figure 3. The vertical profile of the back scatter coefficient recorded using the Lidar complex Polly XT - TROPIS during the dust haze period of August 9, 2015 as part of the CADEX project

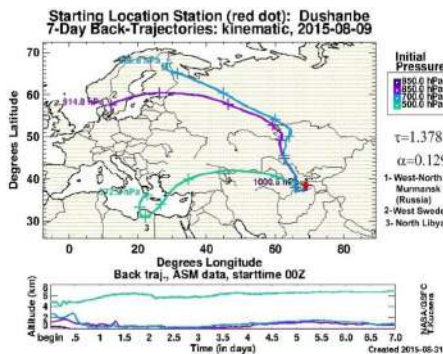


Figure 4. The back trajectory of air masses during the formation of DH

In the case of intense invasions of cold air with the rapid mixing of atmospheric fronts, strong winds arise, causing DS and DH both outside Tajikistan and in its valleys along the route of the air flow. Orography features also contribute to the strengthening of winds in the south-western regions of Tajikistan, and the DS capacities in this zone are associated with the large reserves of loess soils and light gray soils (1000 square kilometers desert). Dust storms invade Tajikistan mainly from the south of the country (Ayvadh village), while the invasion through a narrow gorge in the south of the republic framed by low mountains (altitude 1100 m) creates an aerodynamic effect, the speed of the invasion can sometimes reach 25-30 m/sec, extending to Dushanbe. Since the Dushanbe city is covered from all sides by mountains, the dust haze may exist for a long time [5].

The Dushanbe city is located at an average elevation of 821 m above sea level, in the intermountain Gissar valley, surrounded from the north by the Gissar ridge, and from the south by the low Rangon mountains. The valley is open only from the western and eastern sides by narrow intermountain passes. The orographic isolation of the valley contributes to the increase of the air circulation, as a result of which windless weather prevails here and, accordingly, a stagnation of pollutants occurs [1-3].

One of the main factors causing the air stagnation is the anticyclonic circulation, which causes the development of powerful retention layers — the inversion layer, when the temperature rises with the height, or the is other mal layer, when the temperature in a certain surface layer remains constant. Inversions that have the most significant effect are formed on clear and cloudy nights due to the cooling of the surface air layer. In addition, during the winter period, the arctic front plays a role of the retaining layer, which penetrates into the valley and sharply cools the surface layer of the air at an altitude of 1-1.5 km.

As a result of these phenomena, there is a retention and accumulation of pollutants. Such substances include: particulate matter (dust, combustion products) and harmful gases (CO, ground-level ozone, NOx, etc.).

Some episodes of the dust haze for the period 2010-2015 are shown in Table 1 and Table 2, indicating the aerosol optical thickness (AOT) (at $\lambda = 1020, 500$ and 340 nm), water vapor amount (W, cm), Angstrom parameter $\alpha(\lambda)$, fine and coarse and total fractions of AOT at 500 nm, the number of measurements per day (N), the value of the daytime cooling and nighttime warming, as well as the mass concentration of particle matter less than 10 mm (PM10) for these days. For comparison, these characteristics are given for particularly clear days of this series [6].

Table 1. Some episodes of the dust haze for the period 2010-2012

Date	τ			W(cm)	$\alpha(\lambda)$	AOT (500nm)			N	dT _a	dT _n	PM10($\mu\text{g}/\text{m}^3$)
	1020nm	500nm	340nm			Total	Fine	Coarse				
06/14/2010	1.876	1.795	1.866	2.369	0.025	1.787	0.168	1.619	6	-2.6	3.3	748
08/23/2010	2.533	2.775	2.878	2.605	0.12	2.77	0.479	2.291	25	-1.3	4.2	1156
08/24/2010	0.846	0.934	0.959	1.41	0.1	0.932	0.151	0.781	16	-5.2	2.3	389
10/02/2010	0.03	0.053	0.07	0.431	0.553	0.052	0.021	0.031	59			22
10/13/2010	1.446	1.528	1.571	2.02	0.073	1.527	0.218	1.309	8	-2.3	5.2	637
10/22/2010	1.037	1.084	1.081	0.762	0.033	1.084	0.147	0.938	43	-12.2	5.4	452
01/21/2011	2.136	2.32	2.538	1.097	0.17	2.318	0.447	1.87	2	-2.8	6	967
01/30/2011	1.299	1.334	1.437	1.155	0.095	1.334	0.195	1.139	2	-2.8	5.5	556
03/06/2011	1.323	1.356	1.452	1.07	0.087	1.354	0.196	1.158	1	-2.5	6.8	565
03/23/2011	0.714	0.704	0.739	0.872	0.214	0.706	0.076	0.63	8	-1.8	1.2	293
08/08/2011	1.602	1.749	1.818	2.031	0.103	1.75	0.305	1.445	33	-3.8	1.1	729
08/26/2011	1.766	1.994	2.093	2.641	0.149	1.995	0.42	1.575	37	-4.4	1.6	831
10/06/2011	2.68	2.661	2.623	1.428	0.027	2.665	0.271	2.394	11	-4.3	3.7	1109
10/07/2011	1.415	1.4	1.416	1.578	0.011	1.401	0.129	1.272	36	-6.1	0.5	583
10/08/2011	0.862	0.896	0.947	1.537	0.068	0.896	0.125	0.771	30	-5.7	0.3	373
11/30/2011	0.03	0.069	0.11	0.52	1.427	0.557	0.452	0.104	11			29
05/16/2012	1.857	1.856	1.932	2.174	0.031	1.854	0.207	1.647	2	-4.5	1.6	773
07/13/2012	0.947	1.072	1.115	1.406	0.133	1.07	0.218	0.852	64	-2.8	0.8	447
08/25/2012	0.886	0.989	1.048	1.905	0.136	0.987	0.179	0.808	48	-6	3.6	412
12/21/2012	0.021	0.058	0.094	0.718	1.685	0.12	0.104	0.015	18			24

Table 2. Some episodes of dust haze for the period 2013-2015

Date	τ			W(cm)	$\alpha(\lambda)$	AOT_500nm			N	dT _d	dT _n	PM10($\mu\text{g}/\text{m}^3$)
	1020nm	500nm	340nm			Total	Fine	Coarse				
02/07/2013	0.018	0.047	0.071	0.291	1.562	0.114	0.103	0.011	9			20
02/09/2013	2.506	2.539	2.694	1.211	0.059	2.534	0.325	2.209	1	-3.4	3.3	1058
02/27/2013	1.774	1.959	2.132	0.929	0.186	1.955	0.401	1.554	1	-11.2	9.3	816
03/01/2013	1.17	1.129	1.162	0.879	0.016	1.129	0.096	1.033	2	-14.4	6.3	470
03/22/2013	1.487	1.423	1.429	0.87	0.036	1.42	0.098	1.323	12	-1.4	3	593
05/19/2013	0.581	0.633	0.686	1.902	0.108	0.632	0.099	0.533	25	-6.5	4.6	264
07/05/2013	0.333	0.451	0.585	1.942	0.55	0.448	0.146	0.302	32	-1.9	2.9	188
08/01/2013	0.509	0.795	1.053	2.586	0.684	0.789	0.359	0.431	2	-5.9	0.9	331
08/07/2013	0.35	0.489	0.645	2.209	0.518	0.486	0.169	0.317	35	-2.7	1.5	204
11/05/2013	1.254	1.306	1.349	1.551	0.075	1.305	0.185	1.12	1	-2.2	7.2	544
11/23/2013	0.865	1.062	1.253	0.991	0.367	1.06	0.312	0.749	1	-1.8	1.6	443
07/02/2014	1.393	1.516	1.619	2.275	0.122	1.516	0.243	1.273	50	-4.6	3.4	632
07/25/2014	0.565	0.644	0.708	1.493	0.149	0.644	0.117	0.527	60	-2.9	2	268
07/26/2014	0.449	0.537	0.627	1.679	0.233	0.536	0.119	0.417	58	-3	0.6	224
07/30/2014	0.505	0.655	0.803	2.185	0.367	0.654	0.187	0.466	30	-6.5	6.2	273
08/15/2014	0.941	1.055	1.123	1.481	0.141	1.054	0.196	0.858	11	-7.6	4.6	440
09/28/2014	1.021	1.1	1.138	1.749	0.074	1.1	0.162	0.938	36	-5	3.2	458
11/19/2014	1.047	1.209	1.387	0.961	0.412	1.206	0.287	0.92	5	-4.8	3.8	504
11/20/2014	0.488	1.25	1.791	1.311	1.285	1.239	1.116	0.123	2	-8.9	0.8	521
12/27/2014	0.017	0.045	0.067	0.298	1.333	0.382	0.049	0.333	8			19
01/01/2015	0.088	0.161	0.23	0.418	0.942	0.078	0.033	0.045	14			67
07/06/2015	1.106	1.208	1.247	1.655	0.088	1.208	0.204	1.004	27	-5	7	503
07/21/2015	1.112	1.253	1.357	2.441	0.171	1.252	0.241	1.011	33	-7	3	522
08/09/2015	1.212	1.378	1.43	1.383	0.129	1.377	0.28	1.097	54	-5	6	574

The high values of AOT, PM10 and low values of the Angstrom parameter indicate the presence of the dust. The duration of dust in the atmosphere of Dushanbe due to the city's relief is alarming^[6]. Table 1 and Table 2 present

episodes of pure dust cases ($\tau \geq 0.4$; 0.2) and some data of the clean atmosphere ($\tau < 0.2$; 1.5). In the spring, the Iranian branch of the polar front begins to shift to the north and passes through Central Asia. At this time, temperature

contrasts at the front reach their maximum value, which leads to an increase in the intensity of cyclones. The cyclonic activity in the southern areas of Central Asia, including Tajikistan, causes a pronounced early spring (March - April) maximum in the precipitation [13,14,17,18].

In the valleys of Tajikistan, the dust haze may be a result of the dust storm. This dust haze is delayed by the high mountains more than 2000 m high and lasts from a few days up to a several weeks. Over the last 20-30 years, a number of dust haze events in Tajikistan has increased. In addition, the haze may come from other areas: from the southwest, and south (from April till November every year). The wind that brings it has received a local name of "Afghan". The "Afghan" is of a gray color, reminiscent of fog or haze. The name of the "Afghan" has no scientific evidence as most dust invasions of Tajikistan have a long-term source such as the Sahara deserts east of the Caspian Sea, the Iranian Dasht-e-Kavir and Dasht-e-Lut deserts, the Aralkum desert of the desiccating Aral Sea, the Kyzyl-Kum and Karakum and the deserts in Afghanistan, and Taklamakan desert. The Afghans call this dust invasions "Shuravi" (mean dust come from Soviet Union) as the dust invasions enter Afghanistan through the desert zone of Uzbekistan [5].

Besides the "Afghans", in rare cases that occur (ones every 5-10 years), a dust haze can be transferred from the east of the Taklamakan Desert (China). As a result, the glaciers and snowfields are painted by the light orange color. The local name of this dust haze is "Chinese". This type of dust haze is observed in springs (March - April). This dust haze reaches eastern Tajikistan, and very rarely, once in 20-30 years, it carries over to western Tajikistan. Dust storms in the Taklamakan desert occur on the southern periphery of a strong anticyclone centered in the region of the Lake Balkhash [5].

3. The Number and Duration of Dust Haze Episodes

The bulk of the Central Asian dust storms develops over its lowland area, where the most favorable conditions occur. However, the distribution of dust storms in different parts of Central Asia is extremely uneven. It varies greatly and depends on the place of the origin, the type of synoptic processes, seasons and local topography.

The Figure 5 shows the number of days with the dust haze in Termez, Shaartuz, Kurgan-Tube, and Dushanbe in the period between 2000 and 2014. The average annual number of days with the dust haze in Dushanbe is 12, with seven of which having a strong dust haze, when the visibility is less than 2 km.

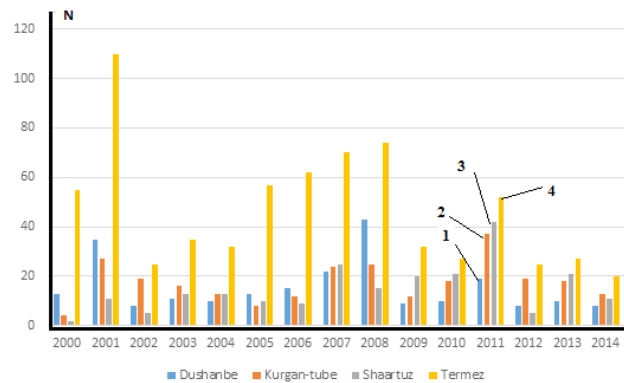


Figure 5. The number of episodes of the dust hazes during the 2000-2014 period at stations: Dushanbe (1), Kurgan-tube(2), Shaartuz(3), and Termez (4)

In the early 1990s, short term dust hazes that lasted 5-7 hours were very strong. In the later part of the 1990s, dust hazes sometimes lasted several weeks, with a visibility of less than 2 km. For example, in 2001, dust hazes reached the record frequency, with an almost daily occurrence in Dushanbe between June and August. There was 29 days continuously dust haze stay in the atmosphere of Dushanbe between July to August 2001.

Our studies [19-22] have confirmed that a dust haze leads to a daytime cooling of air by 3-8°C and a nighttime warming by 2-5°C compared with a clear weather condition. Between November 12 - 20th of 2007, the dust haze covered the whole territory of southern Tajikistan. Sometimes, the horizontal visibility was less than 200-500 m. It should be noted that in the period from September 20, 1989 to October 15, 1990, predominantly strong dust storms with the subsequent precipitations were observed. These dust storms had a duration of 6-8 hours and were accompanied by a decrease in the horizontal visual range down to 50 meters. After 1990s, the duration of dust hazes increased to 3 to 8 days. They often created a pulsating change in the range of the horizontal visibility, and, most importantly, were not accompanied by a precipitation event. In the summer-autumn period of 2001, November of 2007 (from 5 to 24), August 2008 (from 4 to 15), and August of 2009 (from 25 to 29), pulsating dust episodes were observed with a deterioration in the horizontal visual range down to 200 meters. Often after prolonged episodes of the dust haze, dust particles were deposited on the ground without any precipitation. These deposits result in very high pollution levels in the surface layer.

Figure 6 shows the results of our analysis of the duration of dust haze episodes. The trend in the number of dust episodes is similar for all stations. The duration of the dust haze over 2005-2014 was uneven in its nature,

showing a varying dust activity with time.

A seasonal change in the duration of episodes of the dust haze for each observation point (Figure 6) shows some peculiar features. Months of the clean atmosphere or "dusty" months remain overlap for each meteorological station. These features are consequence of station geographical locations. The maximum duration of the dust haze for all meteorological points was observed in the summer time [19-22]. Durations of the dust haze in Dushanbe are more than in other sites because the city is surrounded by hills and mountains.

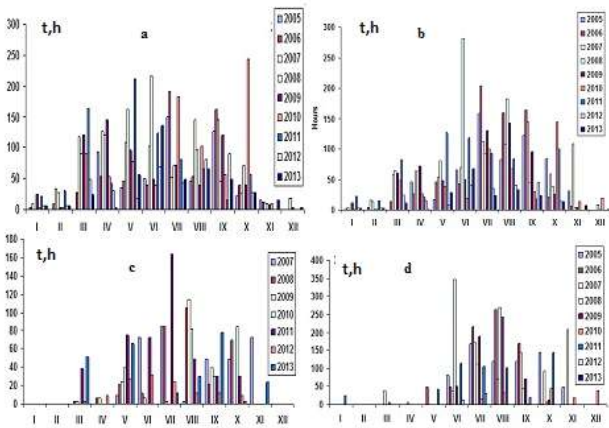


Figure 6. Duration of dusty haze episodes (in hours) in the period 2005-2014 at four stations by month: Termez (a); Shaartuz (b); Kurgan-Tube (c); and Dushanbe (d)

During the instrumental observations 1961-2013, we have found an increase in a decade the mean annual temperature of 0.7-1.2°C in the lowland areas of Tajikistan. A temperature increase (about 0.1-0.7°C) was observed in the southern regions of the country. In the mountains of central Tajikistan, Rushan, and the lowland of the Zarafshan, there was a small reduction of temperature of 0.1-0.3°C.

In large cities, the growth of the temperature was especially significant and reached 1.2-1.9°C, an effect that is clearly associated with the urbanization (building heating, roads, buildings, the impact of transport, businesses, etc.).

Figure 7 shows the dynamics of the average annual temperature in Dushanbe for the last 60 years. Our analysis of the meteorological data indicates a trend of an increase in the mean annual air temperature. Over 60 years for the Kurgan-Tube (elevation 426 m) an increase was 1.9°C, for Dushanbe (803 m), - 1.72°C, for Haramkul (2800 m) - 1.33°C, for the glacier Fedchenko (elevation 4169 m) - 0.73°C. In 1997, the widely observed increase in the average annual temperature was 1-2°C, in 1999 it was 1.2-2.1°C, and in 2000, it was 1.5°C over the long-

term average temperature. These increases have a significant impact on the state of glaciers and water resources of the region.

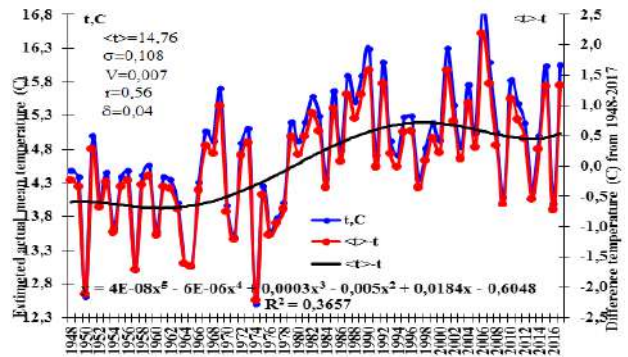


Figure 7. Dynamics of changes in mean annual surface air temperatures in Dushanbe

The highest temperatures were observed in 1990, 1992, 2001, 2006 and 2007. Figure 7 shows that for these years the mean annual temperature was always greater than 16°C. The period between 1950 and 1974 was the coldest of the last century. Most recently, the coldest winter was during 2007-2008. It was the coldest winter of the last 25 years, with the seasonal mean temperature dropping to -5°C, which is significantly lower than the average for 60 years. Since the end of the 1970s over the whole of Tajikistan, a lot of the forest area was cut, creating favorable conditions for the development of semi-arid areas in the country. The reconstruction of forests will take several decades [16].

The increase of air temperature on the plain regions of Tajikistan constituted, on the average, 0.1-0.2°C in a decade. The biggest increase for the 65-year period is noted in Dangara (1.2°C) and Dushanbe (1.0°C), for the rest of the territory it constitutes 0.5-0.8°C, in Khujand it is 0.3°C (Figure 8). An insignificant increase of temperature in Khujand is most likely related to the development of irrigation and building of the Kayrakkum water reservoir. The increase of the annual mean temperature in mountainous areas constituted 0.3-0.5°C in the 60-year period, except separate isolated canyons where the trends are less notable or negative. The biggest increase of annual mean temperature in the mountainous zone (1.0°-1.2°C) was observed in Khovaling, Faizabad and Ishkashim. In altitudinal zones (more than 2500 masl), the increase of temperature on average constituted 0.2-0.4°C and up to 0.6°C in Djavshangoz. The decrease of temperature (-1.1°C) during this period is noted in the kettle of the Bulunkul Lake, which could be related to the characteristic features of climate in the Eastern Pamir [3].

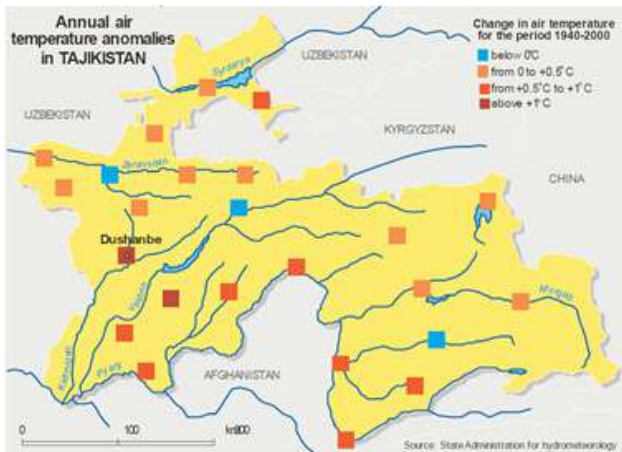


Figure 8. Annual air temperature anomalies in Tajikistan for the period 1940-2000 ^[3]

An analysis of the meteorological data for the last thirty years shows that around the 1980s, Tajikistan observed strong dust storms, especially in September 1989 and October 1990 that were 7 to 11 hours long. Over the last thirty years, observed dust hazes typically last 4 to 15 days, and are accompanied by a pulsating change in the visibility, typically ending without a rain. Several strongest dust hazes occurred in the summer-autumn of 2001 (dust stays in the atmosphere for 29 days during July-August 2001), November (5 to 24) of 2007 and August (from 4 to 15) of 2008, August of 2010, and July-August of 2011. They pulsed with the horizontal visibility range down to 200 meters. After the dust haze ends, the rainfall does not occur and sub-micron dust particles remain in the atmosphere in the surface layer for a long time ^[5].

The climate warming in the next 50 years could lead to a global climate catastrophe. Under climate warming, arid zones in Tajikistan may experience drought and expansion of desert areas (desertification areas), which may lead to more frequent dust storms (or dust hazes) in the Central Asia region. Especially dangerous, the effect of warming could be on the glaciers, which are the main sources of fresh water in the region.

4. Aerosol Characteristics of Dust Storms in Tajikistan

The climatic effects of aerosol are primarily determined by the complex refractive index of the particles $m=n-ik$, which determine the ratio between absorption and scattering radiation by particles ^[9,11,23-26]. These aerosol characteristics affect the dust optical properties and hence dust radiative impacts.

Several methods are used to determine the real and imaginary parts of the refractive index of dust aerosol.

They can be divided into two groups ^[24]. The first group includes methods for determining the real, n , and imaginary, κ , parts based on measurements of optical and radiative characteristics of aerosol in the atmosphere by applying the inverse solution of problems ^[27]. The second group includes methods that involve the analysis of dust aerosol samples. These methods, in turn, can be classified as follows: modeling techniques, by using the modeling of known refractive indices of the main components of substances ^[9,11]; methods of the diffuse reflection, which is based on the theory of Kubelka – Munka ^[28,29]; the Kramers-Kronig method ^[30-36]; and diffuse transmission methods ^[36-38].

A characteristic feature of the first group of methods is that they allow to identify some of the effective value of the imaginary part of dust aerosol present in real atmospheric conditions ^[24]. For example, ^[39] describes a method for determining κ for atmospheric dust with respect to the direct and diffuse solar radiation reaching the Earth's surface. It is assumed that the particles are spherical and the size distribution of particle is precisely known, in particular, ^[40] use the Jungle distribution type. A determination result of is highly dependent on the choice of the surface albedo. In a slightly modified form, the method is used in ^[41], where for Saharan aerosol was obtained the values of $\kappa=0.0029$; 0.008; 0.018, respectively, for $\lambda=0.61$; 0.468; 0.375 μm , assuming that . The size distribution of the particles was determined experimentally.

Methods of the second group are associated with a number of technical difficulties encountered in their implementation. In addition, a potential drawback of these measurements may be that the selection and preparation of aerosol samples are distorted that affect measured optical characteristics ^[24]. The first approach of the second group classification discussed above found its development in ^[26,42,43]. It is based on an assumption that the effective refractive index of the material can be modeled by considering it as a mechanical mixture of compounds, which is established from the chemical analysis of aerosol samples. In particular, Andronova, Zhukovsky and Mandibles ^[42] describes a model of the aerosol chemical composition, which most closely matches the composition of the samples taken in the steppe and desert zones. Given values of are for the relative humidity of 18-25%, Andronova, Zhukovsky and Mandibles ^[42] showed that for this model of arid aerosol, an increase in the proportion to free water leads to a smoothing of the spectral variation of $n(\nu)$ and $\kappa(\nu)$; values of $n(\nu)$ in the visible region is reduced from $n=1.65$ when the relative humidity $f=18 \dots 25\%$ to $n=1.382$, $f=75 \dots 85\%$ ^[24].

Different approaches exist for estimating n and κ , consequently, κ , using R. Authors of ^[28,41] present a com-

monly used approach, based on the Kubelka-Munk theory. According to this theory, one does not need any prior information on the properties of the particle sample. Data for κ , obtained in these studies are presented in [23].

Another approach to define m from the measured reflection is the Kramers-Kronig relations, developed in [30]. The essence of the method is as follows: the measured reflection spectrum $R(\nu)$ (ν - frequency) is used to calculate the phase shift $\Theta(\nu_0)$ using the dispersion relations

$$\Theta(\nu_0) = -\nu_0/\pi \int_0^\infty \ln R(\nu) / (\nu^2 - \nu_0^2) d\nu \quad (1)$$

This method allows to define the complex amplitude reflection coefficient

$$r(\nu_0) = R(\nu_0)^{0.5} \exp(i\Theta(\nu_0)) \quad (2)$$

Then, using the Fresnel formulas one can determine the complex refractive index $m(\nu_0)$ and, therefore, determine the characteristics of $n(\nu_0)$ and $\kappa(\nu_0)$ [24]. To determine the optical constants of dust aerosol, we use the infrared spectrum (IR), where the diffuse transmittance is usually applied. In general, these methods differ in the preparation of the samples. The most widely used method is preparing tablets of KBr [31,42,44]. In this method, the dust aerosol powder mixed with KBr or other alkali metal halide, is compressed into a tablet form. The essential requirements of this approach are: a limit on the size of the particles of the substance ($r < \lambda$), where λ is the wavelength, and the proximity of the refractive index of the alkali metal halide to the index of the refraction of the analyzed material in the transparency window.

An application of the method on a KBr tablet to the study of dust aerosol has yielded spectra of n and κ in the IR [31,44]. The values of the real part were calculated by the Fresnel formulas based on the found range of κ . A slightly modified version of the method was used to determine the optical constants of the samples of soil and dust [44]. The average value of κ for eight different types of dust is presented in [23,24].

In September of 1989, on the territory of Tajikistan, the Soviet-American complex experiment was held to study the lifting of dust, chemical, microphysical, and optical properties of dust aerosol and its impact on local weather conditions and climate [45]. The experiment took place in the framework of the Soviet-American agreement on the environmental protection plan for the Working Group VIII. In addition, experiments were conducted in the Karakum Desert, based in the Repetek sand-desert reserve in 1970. They provided the important data on the profile of solar and thermal radiation. More detailed studies of the optical characteristics of dust were carried out during the

Global aerosol-radiation experiment (GAREKS) in 1977 and 1979 [46].

Golitsyn [45] describes the objectives and the plan of the conducted experiment that took place in the south of Tajikistan in the fall of 1989, see Figure 11. The objectives included the study of the characteristics of dust aerosol and its impact on the radiative fluxes, and consequently on the local weather conditions and climate. Synoptic conditions during the experiment were described in [47]. During the experiment, a satellite observation [48] and airborne sensing [49] were also conducted. The study on the deposition of dust showed that in Shaartuz, 10-30 dust storms were observed per year, and measured average annual values of the intensity of deposition of dust aerosol were 206-617 g/(m² year).

The model of deposition and transport of desert dust for the Valley of the Kafirnigan River (Figure 9) was constructed using the results of the study of the dust storm that occurred on September 16 and 20, 1989 in Shaartuz [45]. In [50], an analysis is presented of the temperature in the atmosphere surface layer in September 1989 during the Soviet-American experiment, showing that there is a marked cooling of the air under the dust haze layer. Experimental evidences suggest that the decrease in temperature and amplitude of its diurnal oscillations coincide with a decrease in the visibility range. A significant increase in the optical thickness during the dust storm was observed [51].

The result of dust microphysical studies were presented in [45]. This study reported that in the arid zone of Shaartuz, the particle size distribution in the range of 0.1-2 microns can be approximated by the Young's distribution, and in the range of 2-20 microns, it can be represented by the lognormal distribution. Results of the measurement of the optical thickness of the atmospheric aerosol obtained by the Soviet and American experiments are shown in [45].

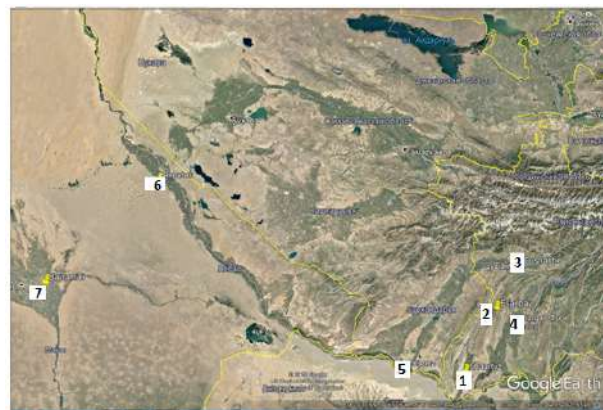


Figure 9. Scheme of the Kafirnigan valley in the southwest of Tajikistan, 1, 2, 3, - ground station data collection: Shaartuz, Esanbay, Dushanbe, respectively, 4-Kurgan-Tube, 5-Termez, 6-Repetek, 7-Bayramali

The altitude range of transport of arid aerosol largely depends on the source of the dust, and on the set of atmospheric processes. It is believed that the transcontinental transport of dust from the Taklimakan Desert occurs just under tropopause layer (~ 10 km)^[38,52]. Over Japan Asian dust aerosols observed in a wide range of heights from 6 to 10 km^[43].

5. Temperature Effects of Dust Storms in Southern Tajikistan

In this section, we analyze changes in surface air temperatures during a dust haze event in the atmosphere over Dushanbe, Shaartuz, and Esanbay, in September 1989. We also present quantitative estimates of the cooling of the air that reduces the amplitude of the daily temperature fluctuation with the reduction of the horizontal visibility range. For these estimates, measurements of the direct solar radiation, taken by an actinometer, and the attenuation coefficient of air photoelectric aerosol turbidity (by using photoelectric aerosol Nephelometer (PhAN)) are being used.

Golitsyn and Shukurov^[10] studied the effects of dust on the temperature using the example of dust storms in the south-western region of Tajikistan. Their study focused on the relationship between the temperature of the surface air layer and the horizontal visibility S_m , based on the data from five weather stations - Ayvaj, Shaartuz, Kurgan-Tube, Sanglok, and Dushanbe, which are located in the direction of south-to-north, similar to the movement of the air in the periods of dust storms. A distance from Ayvaj to Dushanbe is about 250 km. The data are from 10 days of strong dust hazes, which occurred in the July-August 1976, 1979, 1980, and 1984 with the vertical thickness of the dust layer reaching 1.2-2.5 km, S_m values ranged from 0.2 km to 10 km. In the daily course often, almost in all cases, there was a decrease of temperature during the daytime, and an increase in the temperature at night in comparison with clear conditions. The temperature was measured 8 times a day, every 3 hours (Moscow time: GMT+3, day starts with 00 hours).

All analysis gave the same results: a reduction in average daily temperature with decreasing S_m . This fact suggested the possibility to consider a dust haze as a natural analogue of the smoke haze in the study of climate effects of nuclear war fires^[53-55].

Our study describes a detailed analysis of the temperature data obtained at the meteorological stations: Dushanbe, Shaartuz, and Esanbay. We investigated actinometrical atmospheric transparency P_a by aerosol, the attenuation coefficient in the atmospheric boundary layer σ_a , km^{-1}

and temperature effects for each episode of the dust haze. During the experiment, there were only two episodes of dust: the moderate haze during September 16-18, 1989 (the 1st episode) and the thick haze on September 20-21, 1989 (the 2nd episode). Synoptic conditions during the experiment described in^[47]. The values of the average daily drop of the temperature (ΔT) and the amplitude of the temperature oscillations (ΔT_A) in its daily course were evaluated only for the 1st day of the dust haze on 20 September. The results of measurements air temperature t ($^{\circ}\text{C}$) (see Figure 11), actinometrical transparency of the atmosphere in aerosol (P_a) and the attenuation coefficient σ_a , as well as obtained from these data values of the aerosol optical thickness of the atmosphere, $\tau_a = -\lg P_a$ and σ_a , are shown in Figure 12.

Figure 10 (a) dots denote: I – values t , measured at the meteorological station Dushanbe; II – value t , which could be realized in 09 hours on September 20 in the absence of the dust haze; III – value t which could only be realized due to the arrival of the cold air mass. The envelope line of I held on the maximum t in the non-dust days 15, 19, and 28 September; the envelope-line II – done with the minimum night t in the non-dust days of 25 and 28 September; the envelope line III – done with maximum daily values of t in clear days 25 and 28 September; the vertical dashed line IV is in the period 09 hours, close to the time of the invasion of the cold air mass in the range of Dushanbe; poly line V – conducted by the values t measured in the term of 09 hours to determine the day with a maximum turbidity of the air.

The solid vertical lines denote the beginning and end of the precipitation event. Oblique dashed line shows a designated intervals maximum t , day at 12 and 15 hours and the minimum in 00 hours and 03 hours. Due to the lack of value of t , 15 and 21 h points are joined by a dotted line.

As can be seen from Figure 10, the main features in the behavior of day and night, $^{\circ}\text{C}$, when the dust haze agreement with the data^[10] days, temperature values t fall due to the general weakening of the solar radiation in the visible and infrared radiation emitted from the earth surface caused by dust hazes. The absolute values of the daytime cooling of the air are higher than its night time warming. The same result can be seen for meteorological stations Shaartuz and Esanbay.

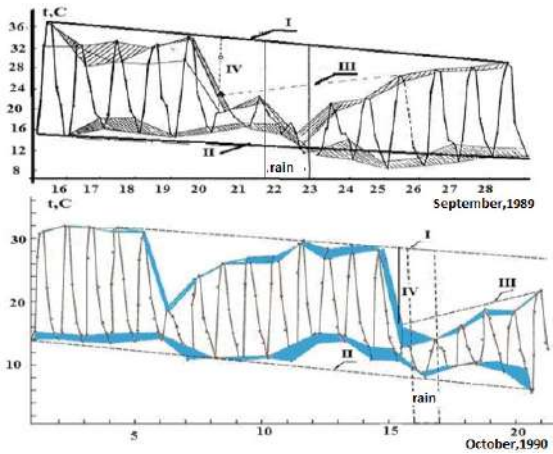


Figure 10. Variations surface air temperature in Dushanbe during the dust storms: a - in September 1989, b - in October 1990

During the second episode of the dust storm, with the arrival of the cold air mass between the 06 and 09 hours on September 20, within 09 hours according to Figure 10, the temperature was reduced by about 10^0 (Figure 10 shows the difference in t , °C, levels 3 and point 1 of the envelope). This finding is consistent with the data [56]: the intrusion of the cold air on the territory of Tajikistan (Weather data in Ayvaj) 02 hours on September 20, causes a sharp decrease in the air temperature.

The line I (Figure 11) indicates a monotonic decrease in t , °C from 15 to 29 September by about 10^0 °C, which in overall agree with many years of average data on the temperature in this period by about 6^0 °C.

Thus, the analysis of the results showed that for the first dust episode (September 17) daytime temperature dropped relative to the line I is for Dushanbe - 2.4^0 °C, for Shaartuz - 5.5^0 °C, and for Esanbay - 5^0 °C. The nighttime temperature is increased relative to the line II, respectively 2^0 °C, 3^0 °C, and 1.3^0 °C.

For the second dust episode on September 20, the daytime temperature dropped to the line I is 14^0 °C for Dushanbe, 11^0 °C for Shaartuz, and 12.4^0 °C for Esanbay. The night temperature increased relative to the line II of the 2.4^0 °C, 3^0 °C and 2^0 °C, respectively.

Figure 11 (dots) denotes 1 - P_a values of the transparency of the atmosphere, according to solar radiation measurements (angular height of the Sun on September 15-20 was 53^0 , the number of air masses, respectively, $m=1.2$). Dots 2 show value of S_m , calculated as $S_m=3.9/\sigma_a$. Dots 3 show values of the optical thickness of the atmosphere in aerosol conditions obtained from the relationship; Dots 4 show values of σ_a .

As noted above, σ_a was measured on September 17 and 20, the rest of the values σ_a reconstructed from the σ_a

comparison with τ_a the values measured at noon on September 15-19. The numerical values of these quantities are given in Table 1, indicating the value of the mean-square deviation and relative errors.

The value of P_a , σ_a , and τ_a refer to the effective wave length $\lambda=0.5\mu m$. Evaluation of the vertical thickness of 1 dusty haze of the 1st episode of the ratio $\tau_a=\sigma_a L$ gives $L=0.9$ in the direction of the sun. This result is consistent with the conclusion of [10], if we consider that Dushanbe is located at a height $H=0.821$ km above sea level.

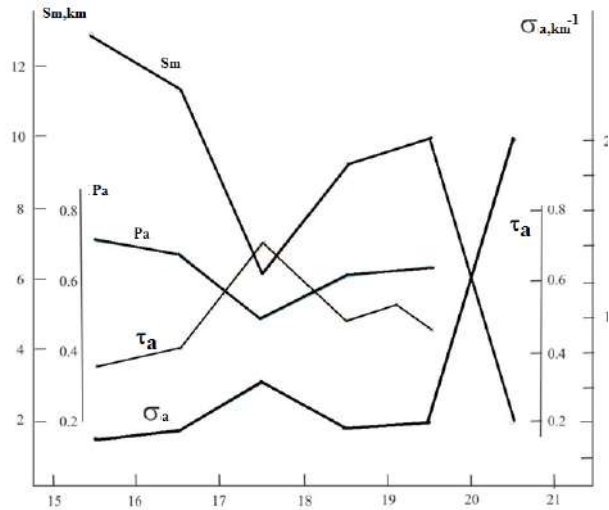


Figure 11. Diurnal variation of different optical parameters of the atmosphere during the first and the second dust episodes: S_m – horizontal visibility, σ_a – back scattering coefficient, P_a – transparency of atmosphere, τ_a – aerosol optical thickness (on the X axis - days, September 1989)

As can be seen from Figure 11 and Table 3 the value of S_m in the period of the 1st episode of the dust varied in a range from 6.3 km to 13 km, which is consistent with the assessment of the values of S_m for the 1st episode at the meteorological station, in which $S_m=4-10$ km. According to measurements with PhAN, a value of September 20 is 2 km, which gives the value of $S_m=2$ km. However, according to all meteorological stations (Shaartuz, Esanbay, and Dushanbe), as noted in [57], the values of S_m fall to 0.5 km.

The data processing procedure is somewhat different from that used in [10]. However, the average daily temperature for the

$$t_d = \sum_{i=1}^6 t_i / 6 \quad \text{06 - 21 hours period and average night } t_n = \sum_{i=1}^2 t_i / 2 \quad \text{for the period 00 and 03 hours,}$$

then everyday, starting from September 15 to September 20, inclusive, were determined by the total temperature $t_c=t_d+t_n$. The further procedure of the data processing is shown in Figure 14, where the straight lines 1 and 2 are plotted as envelopes according to the values of t_c at noon on

September 19 and 15, on midnight on September 15 and 18 in the clear day.

Table 3. The mean values of P_a, τ_a, σ_a (km^{-1}). The columns are standard deviations for the P_a and τ_a . The relative errors of σ_a and $P_a \cdot S_m$ for 17 and 20 September 5% for σ_a, S_m 15, 16, 18, September. The values of $\Delta T, K$ and $\Delta T_a, K$ obtained by the envelope method.

N	Day	P_a	$\delta P_a / 10^3$	τ_a	$\delta \tau_a / 10^3$	σ_a	S_m	$\Delta T, ^\circ K$	$\Delta T_a, ^\circ K$
1	09/05/89	0.70	7	0.35	1	0.305	12.8	0	13.6
2	09/16/89	0.67	9	0.40	1	0.330	11.8	0.9	9.6
3	09/17/89	0.49	3	0.71	5	0.616	6.3	2.2	6.4
4	09/18/89	0.62	30	0.48	4	0.400	9.8	2.1	9.0
5	09/19/89	0.63	20	0.47	4	0.380	10.3	0.4	12.2
6	09/20/89	-	-	-	-	2.00	1.95	6.7	2.8

Lines shown on Figure 12 were drawn from the values of the daily average temperature t_d and the night average temperature t_n , values $\Delta T, ^\circ K$, are the daily cooling temperature under a layer of haze estimated as $\Delta T = \Delta T_d + \Delta T_n$, where ΔT_d is the difference between the values t_d and $t_{skirting}$ envelope on the line 1 (see explanatory notes to). ΔT_n is the difference of values between t_n and $t_{skirting}$ on the envelope line 2 values, ΔT_n is defined as the temperature difference between noon and midnight smoothed lines 1 and 2 (envelope method discussed in further details in [50]).

The Figure 12 presents the main results of this analysis. Dots denote the 1-values T. These values are assigned to each episode as a dust-to-one in general; 2-values of $\Delta T, ^\circ K$, according to the present study-prepared by the method of envelopes (see interpretation of Figure 14).

The results of this study confirm the main conclusions of [10], the system decrease in T , at the earth's surface and the amplitude of the diurnal oscillations with decreasing S_m .

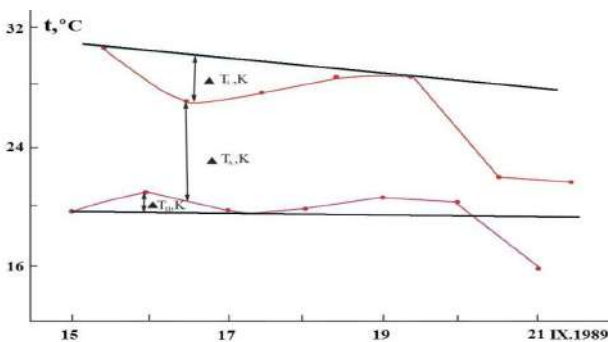


Figure 12. Explanation of the definition of the envelope method ΔT value and ΔT_a at the different S_m .

Taking into account the data of this work and that of [10], it can be argued that values of $\Delta T, \Delta T_a$ and S_m have a fairly definite relationship in the range of S_m minimal to

$S_m = 12 \text{ km}$. When $S_m > 12$ values ΔT are negligible and close to ΔT_a during clean days.

It should be noted that in October 1990, two episodes of the strong dust storm (October 6, 1990 and October 15, 1990) were observed. Dust storms led to a sharp decrease in the daily temperature and a warming in the night temperature. Meteorological visibility reached 0.5 - 1 km. The moderate dust haze on October 12, 1990, led to a decrease in the daily temperature and an increase in the night temperature.

When comparing the amplitude of the temperature of the clean day before the dust storm and the clean day after the dust storm, we obtain the night warming up to 8 °C and the daytime cooling to -16 °C (Figure 13a). When comparing the amplitude of the temperature of the clean day before dust haze and clean day after the dust haze, we obtain some night warming up to 4 °C, and the daytime cooling to 3 °C (Figure 13b).

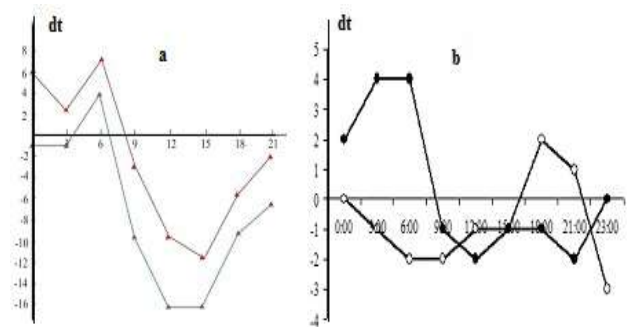


Figure 13. Comparison of the amplitude of the temperature of the clean day before the dust storm and clean day after the dust storm (September 20, 1989) (a): Comparison of the amplitude of the temperature of the clean day before the dust haze and the clean day after the dust haze (August 09, 2015) (b)

6. The Temperature Effect of Dust Aerosol during a Dust Haze Event in the South of Tajikistan

The data on meteorological parameters of the atmosphere were obtained from the site <http://www.rp5.ru>. For the analysis of the meteorological data, we collected the data in the period from November 8 to November 21, 2007, when there were a few interesting dust episodes. The values of ΔT and ΔT_a , the average daily temperature drop and the amplitude of the oscillations in its daily course, were evaluated for all episodes of November 08 to November 21, 2007 (see Figure 14).

The results of temperature measurements and measurements of the aerosol scattering coefficient, σ_a , and obtained from these data values of the aerosol optical depth

$\tau_a = -\lg P_a$ and σ_a shown in Table 2, the temperature settings are shown in Table 3. P_a is the aerosol transparency of the atmosphere.

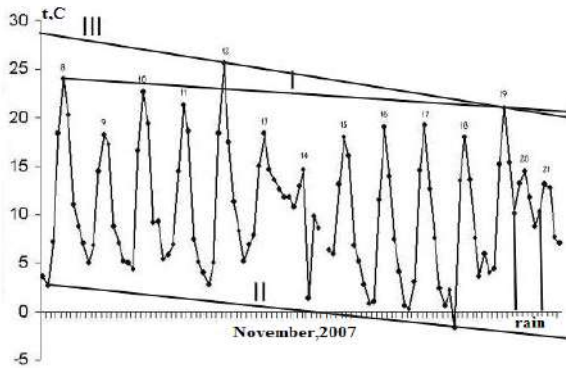


Figure 14. Variations in the surface air temperature in Dushanbe during the dust haze in November 2007

Values of σ_a were measured on November 8 and 12, the rest of the values reconstructed from the measured values of σ_a and τ_a in the afternoon of November 9, 10, 13...21. The value σ_a for dust episodes that occurred on November 9, 13, 14, 15 and the data, τ_a on these days were measured. The values of S_m , km, calculated from the data σ_a with the ratio of $S_m = 3.9/\sigma_a$ from the measured values of the aerosol scattering coefficient, σ_a . Evaluations of the vertical thickness of the dust haze in the first episode give $L = 1.9$ km in the direction of the Sun.

Figure 14 shows the line I, which is computed with maximum temperatures of the clean days of November 8 and 19; the line II is computed with a minimum night temperature in the clean days of November 8 and 18; the line III is computed with maximum daily values of the air temperature in the clean days of November 12 and 19; the vertical line represents the time 08 hours, close to the time of the invasion of the cold air mass within the Dushanbe. The solid vertical lines denote the beginning and end of precipitation.

Table 4. The mean values of P_a , τ_a and σ_a km⁻¹ and temperature settings.

Days	S_m	σ_a	τ_a	P_a	$\langle t_a \rangle$	$\langle t_n \rangle$	ΔT_1	t_{md}	t_{mn}	ΔT_2
11/08/07	51	0.07	0.1	0.93	5.62	17.45	11.83	24	8.8	15
11/09/07	0.5	7.82	-	-	7.6	14.15	6.55	18.2	7	11
11/10/07	2	1.95	1.8	0.17	7.9	15.75	7.85	22.6	9.3	13
11/11/07	4	0.97	0.9	0.41	5.97	15.3	9.33	21.3	5.1	16
11/12/07	51	0.07	0.1	0.87	7.46	16.6	9.14	25.6	8.3	17
11/13/07	0.5	7.82	-	-	9.58	17.45	7.87	18.4	13	5.8
11/14/07	0.5	7.82	-	-	10.5	9.92	-0.58	14.6	8.6	6
11/15/07	0.2	19.6	-	-	6.13	13.27	7.14	18	5.2	13
11/16/07	2	1.96	1.8	0.17	3.8	13.7	9.9	19	4.1	15

11/17/07	4	0.97	0.9	0.41	3.43	12.35	8.92	19.2	2.4	17
11/18/07	4	0.97	0.9	0.41	3.5	10.9	7.4	18	3.6	14
11/19/07	4	0.97	0.9	0.41	8.3	14	5.7	21	13	7.8
11/20/07	10	0.39	0.4	0.7	10.23	11	0.77	13.1	7	6.1
11/21/07	51	0.07	0.1	0.93	9.75	14.75	5	20.4	16	4.4

*

Note: S_m - horizontal visibility range

σ_a - aerosol scattering coefficient

τ_a - aerosol optical thickness

P_a - transparency of the atmosphere

$\langle t_a \rangle$ - average daytime temperature

$\langle t_n \rangle$ - average night time temperature

t_{md} - midday temperature

t_{mn} - midnight temperature

As can be seen in Figure 15, the main features in the behavior of the daytime and nighttime temperatures in the dust haze correspond to the data of [10], i.e., daily temperature drops due to the general weakening of the solar radiation by the dust haze in the visible and infrared radiation.

Absolute values of the day time cooling of the air are more than the absolute value of nighttime warming. The same result can be seen from measurements of air temperatures at the meteorological station in Termez (Uzbekistan).

Line 1 (Figure 15) indicates a monotonic decrease in the temperature from November 8 to November 21 of about 3.1°K. For all episodes of the dust haze, the analysis of the results is shown in Table 4.

The data processing procedure is somewhat different from that used in [10]. However, as in [10], we determined the average daily temperature $t_d = \sum_{i=1}^4 t_i / 4$ in the period from 08 to 17 hours and average night $t_n = \sum_{i=1}^4 t_i / 4$ for the period from 20 to 05 hours. Then everyday, beginning from November 8 to November 21, we determined the total temperature $t_s = t_d + t_n$. The further procedure of the data processing is shown in Figure 17, where the straight lines 1 and 2 are shown as envelopes according to the values at noon's on November 8, 21, and t_n - at midnight on November 11 and 17.

Lines 1 and 2 were drawn from the values of day t_d and night t_n . The values of ΔT , which are daily cooling temperatures under the haze layer were estimated as $\Delta T = \Delta T_d + \Delta T_n$, where ΔT_d is the difference between the values t_d and t_{env} shown by the line 1, ΔT_n is the difference between the quantities t_d and t_{env} , shown by the line 2. The values ΔT were determined as the difference between the temperature at noon and at the midnight. Numerical values of T and T_A are shown in Table 5.

Figure 15 and Table 5 present the main results of this analysis. The points marked 1 give ΔT values obtained by

the 1st data processing method of comparing the total daily temperatures.

Table 5. Average values of temperature parameters

Days	$\langle t_n \rangle$	$\langle t_d \rangle$	T_1	t_{md}	t_{mn}	T_2	ΔT_1	ΔT_2	$T(K)$	$T_A(K)$
08/11/2007	5.62	17.45	12	24	8.8	15	0	2.5	2.5	-2.5
09/11/2007	7.6	14.15	6.6	18.2	7	11	-5.76	1.2	-4.6	-6.96
10/11/2007	7.9	15.75	7.9	22.6	9.3	13	-1.15	4.2	3.05	-5.35
11/11/2007	5.97	15.3	9.3	21.3	5.1	16	-2.3	0	-2.3	-2.3
12/11/2007	7.46	16.6	9.1	25.6	8.3	17	2.7	2.3	5	0.4
13/11/2007	9.58	17.45	7.9	18.4	12.6	5.8	-2.3	10.8	8.5	-13.1
14/11/2007	10.5	9.92	-0.6	14.6	8.6	6	-8.1	3.46	-4.6	-11.6
15/11/2007	6.13	13.27	7.1	18	5.2	13	-4.61	2.3	-2.3	-6.91
16/11/2007	3.8	13.7	9.9	19	4.1	15	-3.1	1.5	-1.6	-4.6
17/11/2007	3.43	12.35	8.9	19.2	2.4	17	-2.7	0	-2.7	-2.7
18/11/2007	3.5	10.9	7.4	18	3.6	14	-3.5	1.92	-1.6	-5.42
19/11/2007	8.3	14	5.7	21	13.2	7.8	0	12.3	12.3	-12.3
20/11/2007	10.23	11	0.8	13.1	7	6.1	8.1	6.54	14.6	1.56
21/11/2007	9.75	14.75	5	20.4	16	4.4	0	16.15	16.2	-16.2

Note: $\Delta T_1 = t_{md} - t_{env}$; $\Delta T_2 = t_{md} - t_{env}$

Dust storms and haze events are the essential meteorological factors in Central Asia. An average annual number of days with haze events in Dushanbe is about 15-20, with seven days of a strong haze when visibility values becomes less than 2 km. The year of 2001 is the record. During that year, in the period from June to August, the weak haze in Dushanbe was almost daily. A number of days with the moderate to severe haze in the period from June to November was 29 days. Note that in the summertime, there is a cooling of the air by 3-8 degrees compared with clear weather days [58,59].

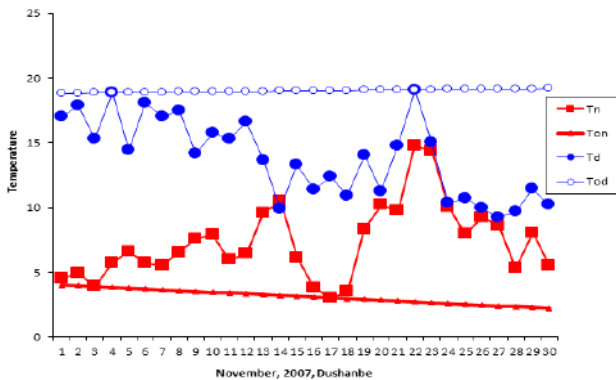


Figure 15. Explanation of the variables defined by the envelope $\Delta T(K)$ and $\Delta T_A(K)$ for various S_m

In 2007, during the study period from November 8 to November 21, there were a few days of dust haze events of various magnitudes. A detection processes brought a dust haze resulting in a drop of the visibility range from

10 km to 0.2 km (see Figure 17). Our analysis of several episodes of the dust storm (dust haze) shows that for an average dust haze ($S_m=8-10\text{km}$), the amount of the daily cooling of the air temperature at all studied stations is on average $\Delta T=2^\circ\text{K}$, in the case of strong dust storm ($S_m<1-2\text{km}$) is $\Delta T=4.5^\circ\text{K}$. (Figure 18)

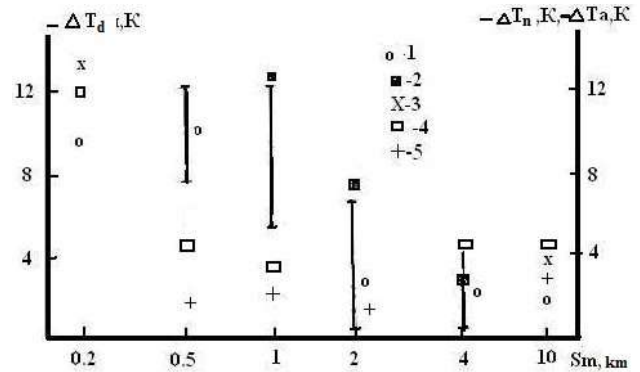


Figure 16. Comparison of the $\Delta T(K)$ depending on the range of visibility S_m

The absorption by dust particles in the infrared range is especially important in the area of a transparency window of 8-13 μm , where dust and main atmospheric gases significant absorbs the thermal radiation. This is precisely the wavelength region where the distribution function of the Planck thermal radiation has a maximum for common terrestrial temperatures. Therefore, the loss of heat in the space of the thermal radiation emitted by the soil is reduced due to the presence of dust particles (the coarse fraction), having strong absorption bands in this spectral range near 10 μm . In this case, almost all the energy of the absorbed particles of the solar and thermal radiation is converted to heat of the air. At the night, the heat absorbed by dust particles (especially, by coarse fraction), transfers to the air and heats it. As a result, the total daytime air temperature in a dusty atmosphere is lower than in a clean day and the nighttime temperature is a bit higher than in a clean night. The particle size distribution function has a bimodal character with maximum in the range of 0.5-10 and 0.05-0.5 microns (Figure 17). One can see the difference between clear and dust haze days, although the distribution of particles is always bimodal. During the invasion of the dust haze, particles of the coarse fraction predominate. The proportion of the coarse fraction gradually increases with increasing aerosol optical thickness in case of the dust intrusion and low values of the Angstrom parameter indicate the presence of coarse particles.

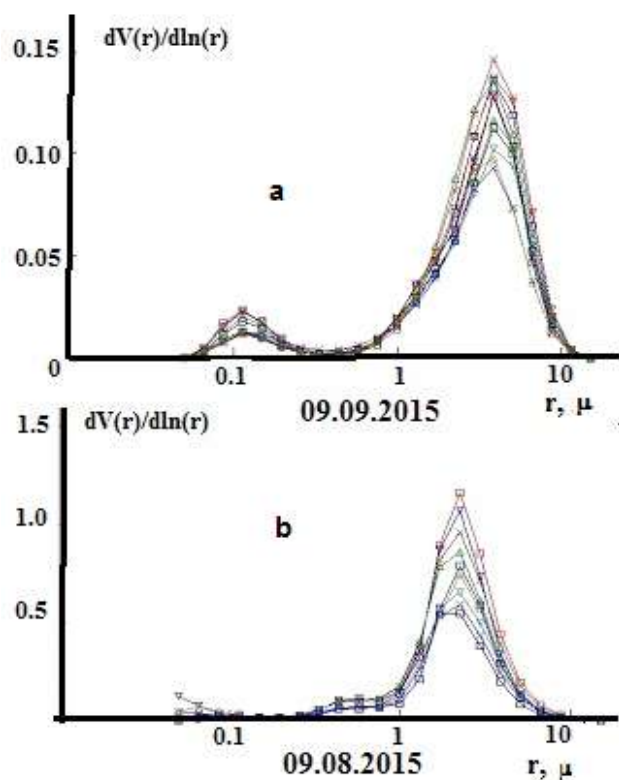


Figure 17. Changes in the size distribution function of aerosol particles in the atmosphere of Dushanbe city: a - in the usual situation (09/09/2015); b – case dust haze (08/09/2015)

Dust particles can participate in two events, leading to opposite changes in the temperature. We can identify the critical parameters that determine the transition from one effect to another. Figure 18 shows the dependence of the average daily air temperature in dusty and clean atmospheres on the concentration of dust (based on our experimental results).

To clarify the role of dust aerosol in the long-term changes of the air temperature, it is necessary to analyze and separate the contributions of aerosols in the greenhouse and anti-greenhouse effects. This can be achieved by using decades-long measurements of air temperatures at various meteorological stations in Tajikistan. A trend of the mean annual temperature is different for the measurement points located at different altitudes. Figure 18 shows an increase in the mean annual temperature over 100 years at altitudes ranging from 426 m (Kurgan-Tube) to 4260 m (Fedchenko). The higher the observation point above sea level, the less of the warming effect is observed. In the arid zone, where Tajikistan is located, dust particles are constantly present in the atmosphere with a background value of about 100 mg/m^3 . The greater is the height of the observation point, the lower is the concentration of the

background aerosol and dust.

Studies [50,58] have reported the effect of dust storms on the temperature regime of the atmospheric boundary layer and found that dust storms lead to a decrease in the air temperature at the surface layer of the atmosphere, but an explanation of the effect of the dusty haze on the temperature regime of the surface layer is not yet available. For the further clarification of the influence of the dusty haze on the temperature regime of the surface layer, we studied data on temperature changes obtained at meteorological stations in Dushanbe, Termez, Bayramali, and Repetek for the period 2005-2010 and for the Kurgan-Tube for the 2008-2010 year.

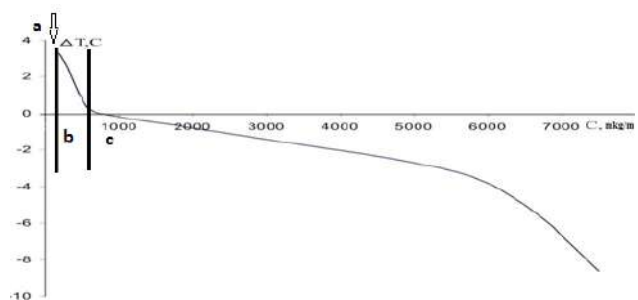


Figure 18. The dependence of the average daily air temperature shifts on the concentration of dust aerosol (a – background; b- dust haze and c-dust storm).

In the study of temperature measurements during a few months at Dushanbe, Termez, Bayramali, Repetek and Kurgan-Tube we detected the exceeding value of the night warming and the daily cooling. This fact suggests that, under certain weather conditions in the surface layer of the dust haze warming occurs. Such a mechanism could proceed as follows: in the presence of a dusty haze in the surface layer of the atmosphere, when the transparency of the atmosphere $P > 0.3$ and the concentration of dust particles is less than $170 \text{ } \mu\text{g/m}^3$, the absorption in the infrared region of the spectrum occurs [15]. At the nighttime, the heat is absorbed by the aerosol particles and the surface of the soil. Thus, there is some heating of the surface layer of the atmosphere at nights.

The portion of the line above the x-axis in Figure 19 corresponds to the greenhouse effect due to the presence of the atmospheric dust haze. The curve, which is below the x-axis, corresponds to the anti-greenhouse effect during the dust storm. An intersection with the x-axis at the almost linear section allows one to define a critical value of the concentration corresponding to the transition from the greenhouse to the anti-greenhouse effect, which is $750 \text{ } \mu\text{g/m}^3$.

Figure 19 shows the intensity of the direct solar radi-

ation as a function of aerosol concentration. At low concentrations of dust aerosol (less than $160 \mu\text{g}/\text{m}^3$), which is almost always present in the atmosphere, dust does not contribute to the greenhouse effect, because the level of the heat transfer from the heated particles is at the level of the thermal noise in the air.

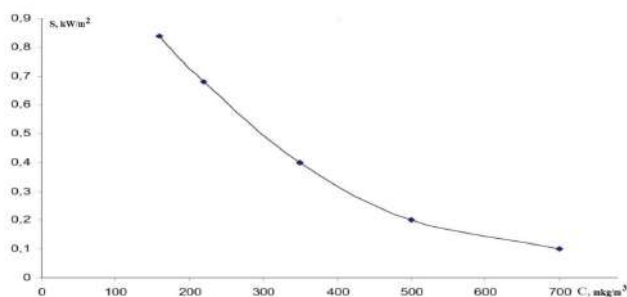


Figure 19. The dependence of the intensity of the direct solar radiation at the surface on the aerosol concentrations.

If the total contribution of the nighttime warming exceeds the total contribution of the daytime cooling, the dusty haze contributes to the greenhouse effect, and vice versa. If the total contribution of the nighttime warming is less than the total contribution of the daytime cooling, the dusty haze contributes to the anti-greenhouse effect. In the study of the temperature data, we found the both effects may occur in the arid (Termez, Bayramali and Repetek), and insub-arid zones (Dushanbe, Kurgan-Tube).

Figure 20a shows a typical example of the behavior of average night and average daily temperatures during a month. The corresponding data for the thermal effects of the dust storm for the same month are shown in Figure 20b. Envelope lines for average daily temperatures were constrained by the maximum values of daily maximum temperature, under an assumption of an absence of a dusty haze. The envelope lines of average nighttime temperatures are made for minimum nighttime temperatures. Value of the daytime cooling was defined as the difference between the average daytime temperature and the envelope of the line drawn by the maximum values of the maximum daytime temperature (in the absence of a dusty haze). Figure 20c shows the aerosol optical depth (Dushanbe, August 2010)

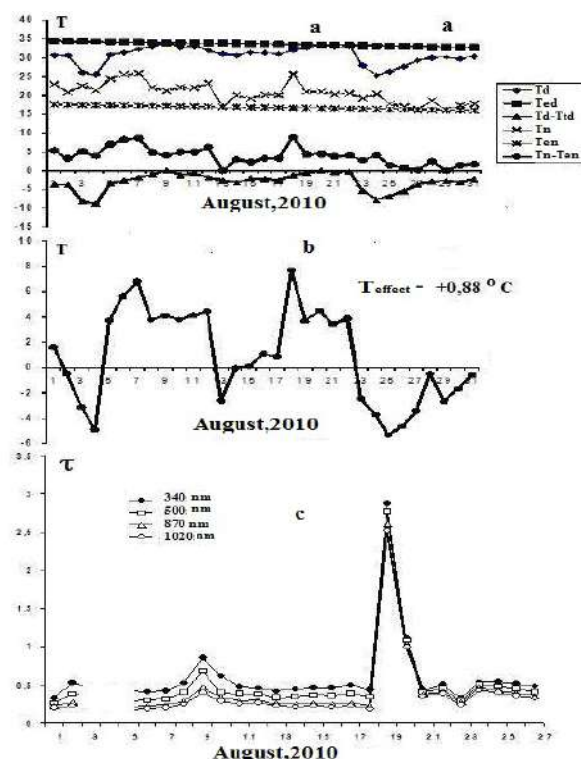


Figure 20. a - air temperature, b - average daily temperature differences due to dust, c - aerosol optical depth (Dushanbe, August 2010)

The magnitude of the night warming was defined as the difference between the temperature and the envelope averaged night line drawn for the minimum night temperature (assuming the absence of a dusty haze). The total value of these differences determines the effect dusty haze on the temperature during a month.

To determine the patterns of influence of dust aerosol on the temperature regime of the surface layer, we studied data on air temperatures, obtained from meteorological stations in Dushanbe, Termez, Bayramali and Repetek for the period 2005-2011 years, and Kurgan-Tube for the 2008-2011.

Table 6 AND Table 7 SHOW THE final results of the processing of the data on the thermal effects, averaged for each month of observation.

Table 6. Changing the daily average values of the temperature effect ($^{\circ}\text{C}$) for Kurgan-Tube and Dushanbe

Kur-gan-Tube	2005	2006	2007	2008	2009	2010	2011
V				3.01	-0.36	3.47	-0.6
VI				3.92	0.06	-2.25	-0.58
VII				0.12	2.24	2.71	0.26
VIII				4.43	0.32	1.07	0.01

IX				0.68	0.33	1.71	-0.71
X				0.71	-0.27	-0.86	
XI				0.98	0.25	-5.95	
Dushanbe	2005	2006	07	2008	2009	2010	2011
V	-2.1	-1.8	-1.23	-0.91	-0.84	-2.4	-2.75
VI	-0.5	-0.54	-2.57	-0.19	-0.64	-1.91	-0.59
VII	1.6	1.56	1.78	0.86	0.05	-2.05	-1.28
VIII	1.1	1.05	0.54	0.24	-0.06	0.88	-0.36
IX	1.2	0.51	-0.84	0.84	-0.95	-1.72	0.17
X	-1.2	1.266	-1.04	3.4	-1.15	-0.73	
XI	-2.6	-0.278	-0.95	-1.92	0.89	-1.42	

The analysis shows that the previously powerful dust storms, such as the September 20, 1989, and October 15, 1990, led to a sharp decrease in the daytime air temperature and an increase in nighttime temperatures. In general, this process clearly led to a sharp decrease in temperature in the lower atmosphere.

Comparing the heat haze effect in cities located in a very narrow range of the south-eastern part of Central Asia, one can discover an interesting pattern. In Dushanbe, Termez, Bayramali, and Repetek the positive thermal effect was observed in 45% of the total number of months that were followed, in the Kurgan-Tube in the last 2 years a positive effect was observed in 85% of the number of months. The average monthly value of the temperature effect, which characterizes the average change in the temperature associated with the dusty air, for Dushanbe (-0.15 °C), Termez (-0.23 °C), Bayramali (-0.35 °C), Repetek (-0.0065 °) and for Kurgan-Tube (+ 0.35 °C) is different.

To determine the reasons for differences in the magnitude of the thermal effect of the air caused by dust, we analyzed the geographical and physical features of the observation locations Repetek (38°34'N., 63°11'E. elevation 185 m), Bayramali (37°36'N., 62°11'E., elevation 241 m) and Termez (37°36'N., 62°11'E., elevation 302m) are in the arid zone in the open countryside. Dushanbe (38°33'N., 68°47'E., elevation 821 m) and Kurgan-Tube (37°50'N., 68°47'E., elevation 430 m) are located in mountainous areas, with blowing winds hindered by the mountains surrounding the valley, where these cities are located (Figure 9).

From the change in the scattering coefficient, one can derive the height of several diffusion layer switch different aerosol concentrations over the various points of the city. Sudden changes in aerosol concentrations correspond to changes in temperature of these layers.

Table 7. Changes of the daily average values of the temperature effect (°C) for Termez, Bayramali, and Repetek.

Termez	2005	2006	2007	2008	2009	2010	2011	2012	2013	2014
V	0.7	-0.36	0.76	-0.33	-0.73	2.11	0.96	0.44	0.64	-1.91
VI	-0.4	-1.49	-0.08	-1.87	0.02	1.8	-0.65	-0.38	-0.58	-2.67
VII	0.9	1.65	0.62	0.6	-0.02	-1.27	-1.07	0.2	0.18	-1.16
VIII	1	1.13	-0.39	0.01	0.05	-1.12	-0.55	0.02	0.08	-0.16
IX	-0.8	-1.67	-0.07	-1.83	-0.35	2.28	-0.34	-0.4	0.31	-1.97
X	-1	-0.85	-1.62	-1.09	-1.45	0	-0.56	-0.94	-0.94	-1.21
XI	-1.3	0.98	-0.68	0.42	1.46	-1.73	-0.69	-0.22	-0.22	
Bayramali	2005	2006	2007	2008	2009	2010	2011			
V	0.6	-1.35	-0.26	-1.81	-1.55	-1.45	-1			
VI	-2.7	0.44	-1.21	-1.65	1.06	-1.07	0.82			
VII	-0.9	2.33	-0.38	0.16	1.3	2.8	0.24			
VIII	-1.6	0.53	-0.11	-0.33	0.38	-3.4	1.2			
IX	1	2.061	-0.15	-0.14	0.11	1.15	0.03			
X	2.4	-0.07	-1.54	-3.36	0.76	4.65				
XI	-1.7	-0.62	-2.54	-2.2	0.59	-4.66				
Repetek	2005	2006	2007	2008	2009	2010	2011			
V	2	0.07	4.02	1.84	-1.97	-1.87	-0.74			
VI	1.2	-1.05	1.01	-0.52	1.14	1.66	0.09			
VII	0.6	1.32	-1	-0.44	0.48	-0.59	0.52			
VIII	-0.2	0.43	-1.07	-0.84	0.01	-0.16	0.39			
IX	1	1.29	-1.62	-1.01	0.44	-0.91	-0.45			
X	0.3	-0.13	0.68	-3.99	-2.26	-0.62				
XI	-3.1	-0.47	0.78	-0.15	0.89	-4.75				

During a dust storm in the surface layer of the atmosphere, the total content of aerosol increases by more than an order of magnitude. Figure 21 shows typical profiles of the scattering coefficient obtained in Dushanbe^[60]. Above the inversion layer, the scattering coefficient is about 10 times less than under the inversion layer (the scattering is shown by a family of curves 2 in Figure 21). In this layer, the absolute value increases as compared with a pure atmosphere average by an order of the magnitude (depending on the capacity of the dust removal).

This leads to a static situation, when the dust rises into the air and for a long time it does not settle and, thus, stabilizes the state of dust. This stabilization occurs by increasing the inversion layers that inhibit the spread of dust in the vertical direction and leads to a uniform mixing. A formation of diffusion layers with different concentrations of dust was recorded in 1989, through airborne measurements over Dushanbe^[60] (Figure 21). In period of Soviet-American experiments, a change in high-rise temperature (T) and the light scattering coefficient, which is proportional to the concentration of the aerosol, were observed^[60].

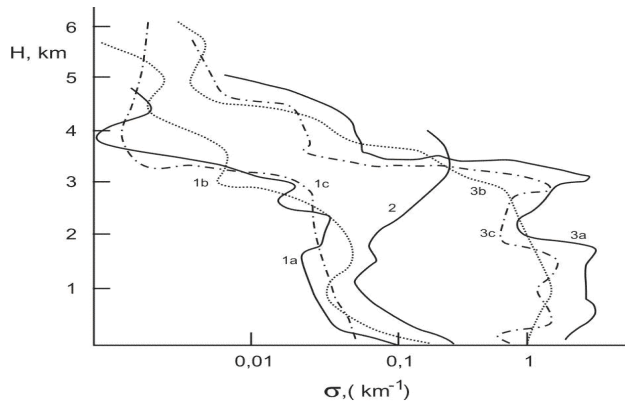


Figure 21. Vertical profiles of the scattering coefficient at a wavelength of $\lambda=0.52\mu\text{m}$ of Dushanbe: 1a, and in c, are for background conditions; 2 is during the dusty haze on September 16, 1989; and 3a, and in c, are during a dust storm on September 21, 1989^[60].

The results of the temperature effect of dust aerosols for five stations located along the path of the dust storms in the period 2005 to 2011 indicates that 41% of the dust aerosol event contributes to the greenhouse effect, and in 59% of the cases contributing to the anti-greenhouse effect.

The temperature inversion (temperature above the inversion layer above $1-1.5^\circ\text{C}$) at an altitude of 3400m (for Dushanbe) becomes more pronounced and has a locking action on the distribution of the aerosol up. Above the inversion layer, the scattering coefficient is only three times greater than the one for a pure atmosphere. The altitude of the temperature inversion for Kurgan-Tube increased more significantly than in Dushanbe.

During dust storms, the developed turbulent mode provides lower-level temperature inversion supporting a good mixing of the aerosol. At a height of $H=1400\text{m}$, well below the inversion layer, the scattering coefficients are practically constant^[60]. The formation of diffusion layers, which are characteristic of the dust haze, is often observed in the arid zones of Central Asia.

7. Conclusions

Tajikistan is located in the global dust belt on the way of transport routes of dust from some major dust sources like the Aralkum desert of the desiccating Aral Sea, the Kyzyl-Kum and Karakum deserts east of the Caspian Sea, the Iranian Dasht-e-Kavir and Dasht-e-Lut deserts and the deserts in Afghanistan and Sahara, and Taklamakan desert in China. Therefore, Tajikistan is frequently affected by severe dust events every year (from April until November) and is a net accumulator of dust. Tajikistan is a country with a dry climate and benefits from its water resources in

the mountainous Pamir region, which are stored in a large part in glaciers. Furthermore, Central Asia and, especially Tajikistan, is strongly affected by climate change. For example, the dramatic glacier shrinking took place in the last decades, which has also effected water resources of Tajikistan and the whole Central Asian region. On the other hand, deposited dust itself can accelerate glacier melt by altering the glacier's surface albedo.

Arid zones of Tajikistan are constantly exposed to the presence of dust particles that a result of dust storm and dust haze events, spreading over the thousands of kilometers. The strengthening of dust storms offset that leads to the distribution dust particles throughout the territory of Central Asia, causing the following consequences: a significant deterioration of public health and other living organisms: 50% reduction in bees and other beneficial insects; a reduction of direct solar radiation; significant weakening of the process of photo synthesis in the vegetation; change the melting regime of glaciers; territorial expansion of desert areas and soil degradation; and the quantity and quality of agricultural products.

In this manuscript, we have analyzed the classification of dust storms and synoptic conditions related to their formation in Central Asia. An analysis of the meteorological data for the last thirty years shows that around the 1980s, Tajikistan observed strong dust storms, especially in September 1989 and October 1990 that were 7 to 11 hours long. Over the last thirty years, observed dust hazes typically continues 4 to 15 days, and are accompanied by a pulsating change of the horizontal visibility, typically ending without rain. Several strongest dust hazes occurred in the summer-autumn of 2001, November (5 to 24) of 07 and August (from 4 to 15) of 2008, August of 2010, and July-August of 2011. They decreased the horizontal visibility range down to 200 meters. After the dust haze ends, the rainfall does not occur and sub-micron dust particles remain in the atmosphere in the surface layer for a long time.

Analyses of the number and duration of dust haze episodes in the period 2005-2014 at four stations: Termez and Shaartuz deserts; Kurgan-Tube rural and Dushanbe urban site show increasing the number and duration of dust haze episodes in 2001.

A comparison of the amplitude of the temperature of the clean day before the dust storm and the clean day after the dust storm was performed, revealing the night warming up to 8°C and the daytime cooling to -16°C . Comparisons of the amplitude of the temperature of the clean day before the dust haze and the clean day after the dust haze, revealed some night warming up to 4°C , and the daytime cooling to -3°C .

We studied the duration of the dusty haze at selected stations: Termez (Uzbekistan), Dushanbe (Tajikistan), determining the seasonal and annual variations of the dust haze using the database of meteorological parameters for Dushanbe (2000-2012), Bayramali and Repetek (2005-2012), Termez (2005-2014), Kurgan-Tube (2008-2012.). The results of the variation of surface temperature during the last century for Tajikistan was analyzed. The results of a detailed analysis of the temperature effect of dust aerosols at five stations, which are located in two neighboring states on the way of transportation of dust storms in the period 2005 to 2012, indicate that 41% of the dust event contributes to the greenhouse effect, and in 59% of the cases contributing to the anti-greenhouse effect.

The study of dust storms should be conducted in different world dust sources to comparatively examine the strength of the sources in terms of the dust flux emission, the initial height of dust plumes that controls the ability of dust plumes to be transported over long distances.

Dust optical properties and its radiative impacts vary from the source-to-source. For instance, the ability of dust to absorb sunlight strongly depends on the presence of certain minerals (e.g., iron oxides). The mineralogical composition varies from one dust emitted area to another. Thus, the world wide sources will need to be well-documented.

The diverse impacts of dust, including the radiative impact, the impact on vegetation, as well as, the adverse impact on human health will need to be examine in the synergistic fashion.

Acknowledgments

This work was supported by the LCLUC (NASA) project "Multicascade synthesis of land cover and land use, climatic and societal changes in drylands of Central Asia" NNX14AD88G and the ISTC project T-2076 «Dust storms and Waste Tailings isotope migration in Tajikistan»

References

- [1] Makhmadaliev, B.; Novikov, V. The First National Communication of the Republic of Tajikistan to the United Nations Framework Convention on Climate Change; Dushanbe, Tajikistan, 2002.
- [2] Makhmadaliev, B.; Kayumov, A.; Novikov, V.; Mustaeva, N.; Rajabov, I. The second national communication of the Republic of Tajikistan under the United Nations framework convention on climate change; Dushanbe, 2008.
- [3] Kayumov, A.; Novikov, V. Third National Communication of the Republic of Tajikistan under the United Nations Framework Convention on Climate Change. 2014.
- [4] Hofer, J.; Althausen, D.; Abdullaev, S.F.; Makhmudov, A.N.; Nazarov, B.I.; Schettler, G.; Engelmann, R.; Baars, H.; Fomba, K.W.; Müller, K. Long-term profiling of mineral dust and pollution aerosol with multiwavelength polarization Raman lidar at the Central Asian site of Dushanbe, Tajikistan: case studies. *Atmospheric Chemistry and Physics* 2017, 17, 14559.
- [5] Nazarov, B.I.; Abdullaev, S.F.; Maslov, V.A. Dynamic processes during dust incursions in Central Asia Irfon: Dushanbe, 2016.
- [6] Nazarov, B.I.; Abdullaev, S.F.; Maslov, V.A. Atmospheric aerosol of Central Asia; Donish: Dushanbe, 2017.
- [7] Zuev, V.E. Atmospheric Transparency in the Visible and the Infrared; Israel Program for Scientific Translations; [available from the US Department of Commerce, Clearinghouse for Federal Scientific and Technical Information, Springfield, Va., 1970.
- [8] Kondratyev, K.Y. Climate and aerosol. *Trudy GGO* 1976, 3-36.
- [9] Ivlev, L.S. The chemical composition and structure of atmospheric aerosols; Leningrad State University: Leningrad, 1982: 368.
- [10] Golitsyn, G.S.; Shukurov, A.K. Temperature effects of dust aerosol as exemplified by dust storms of Tadzhikistan. In *Proceedings of Doklady- earth science sections*. Silver Spring MD: 46-49.
- [11] Ginzburg, A.S.; Sokolik, I.N. The transmission and reflection of light by a homogeneous layer of an absorbant aerosol. *Akademiia Nauk SSSR Fizika Atmosfery i Okeana* 1989, 25: 954-959.
- [12] Goody, R.M. Atmospheric Radiation [Russian translation], 1966.
- [13] Romanov, N.N. Dust storms in Central Asia; Tashkent, 1960: 198.
- [14] Bugaev, V.A.; Georgia, V.A.; Kozin, B.M. Synoptic processes in Central Asia; Tashkent, 1957: 67.
- [15] Abdullaev, S.F. The impact of global climate change and adaptation measures to climate change. In *Nature and Us: Questions of environmentally sustainable development in Tajikistan*, Dushanbe, 2009: 155-184.
- [16] Nazarov, B.I.; Abdullaev, S.F. Aerosol pollution under arid and mountainous areas of Tajikistan. In *Proceedings of International Expert Meeting on the environment*: 60-62.
- [17] Karetnikova, K.A. Synoptic conditions for the occurrence of the "Afghans" and some of the features of this phenomenon. *Journal of Geophysics* 1985, 5: 36-80.

- [18] Dzhorzhdio, V.A. In Guide to short-term weather forecasts, Tashkent, 1954: 73-77.
- [19] Abdullaev, S.F.; Nazarov, B.I.; Sharifov, D.M. Modeling of transport process and distribution of arid aerosol. In Proceedings of XIII Joint International Symposium "Atmospheric and ocean optics. Atmospheric physics.", Tomsk, Russia.
- [20] Nazarov, B.I.; Salikhov, D.K.; Abdullaev, S.F. The description of moving of atmospheric particles in the near earth layer. In Proceedings of Russian-Canadian Workshop Modeling atmospheric dispersion of weapons agents, Moscow: 137-139.
- [21] Nazarov, B.I.; Abdullaev, S.F.; Maslov, V.A. Laws of dusty haze - the number of episodes and duration. In Proceedings of Problems of modern physics, Dushanbe; pp. 65-68.
- [22] Abdullaev, S.F.; Nazarov, B.I.; Madvaliev, U. Climate change in condition of arid and of high mountain regions of Tajikistan. In Proceedings of XVIIth International Energy and Environment Fair and Conference, Istanbul: 277-278.
- [23] Dovgalyuk, Y.A.; Ivlev, L.S. Physics of Water and Other Atmospheric Aerosols, 1998.
- [24] Sokolik, I.N.; Andronova, A.; Johnson, T.C. Complex refractive index of atmospheric dust aerosols. Atmospheric Environment. Part A. General Topics 1993, 27: 2495-2502.
- [25] Kondratyev, K.Y.; Moskalenko, N.I.; Pozdnyakov, D.V. Atmospheric aerosols.; Gidrometeoizdat: Leningrad, 1983: 224.
- [26] Bohren, C.F.; Huffman, D.R. Absorption and scattering of light by small particles; John Wiley & Sons: 2008.
- [27] Herman, B.M.; Browning, R.S.; De Luisi, J.J. Determination of the effective imaginary term of the complex refractive index of atmospheric dust by remote sensing: The diffuse-direct radiation method. Journal of the Atmospheric Sciences, 1975, 32: 918-925.
- [28] Lindberg, J.D.; Laude, L.S. Measurement of the absorption coefficient of atmospheric dust. Applied optics, 1974, 13: 1923-1927.
- [29] Lindberg, J.D.; Gillespie, J.B. Relationship between particle size and imaginary refractive index in atmospheric dust. Applied optics, 1977, 16: 2628-2630.
- [30] Hale, G.M.; Holland, W.E.; Querry, M.R. Kramers-Kronig analysis of relative reflectance spectra measured at an oblique angle. Applied optics, 1973, 12: 48-51.
- [31] Volz, F.E. Infrared optical constants of ammonium sulfate, Sahara dust, volcanic pumice, and flyash. Applied Optics 1973, 12: 564-568.
- [32] Volz, F.E. Infrared absorption by atmospheric aerosol substances. Journal of Geophysical Research, 1972, 77: 1017-1031.
- [33] Volz, F.E. Infrared optical constants of aerosols at some locations. Applied optics 1983, 22: 3690-3700.
- [34] Darmenova, K.; Sokolik, I.N.; Darnenov, A. Characterization of east Asian dust outbreaks in the spring of 2001 using ground-based and satellite data. In J. Geophys. Res., AGU: 2005, 110: D02204.
- [35] Sakai, T.; Nagai, T.; Nakazato, M.; Mano, Y.; Matsu-mura, T. Ice clouds and Asian dust studied with lidar measurements of particle extinction-to-backscatter ratio, particle depolarization, and water-vapor mixing ratio over Tsukuba. Applied Optics 2003, 42: 7103-7116.
- [36] Liu, Z.; Sugimoto, N.; Murayama, T. Extinction-to-backscatter ratio of Asian dust observed with high-spectral-resolution lidar and Raman lidar. Applied Optics 2002, 41: 2760-2767.
- [37] Iwasaka, Y.; Shi, G.; Trochkin, D.; Matsui, A.; Kim, Y.; Yamada, M.; Nagatani, T. Processes of Background KOSA Outbreak. Proceedings of the EMEA 2005 in Kanazawa, 2005, Intern. Sympos. on Environmental Monitoring in East Asia—Remote Sensing and Forests, 2005, 20-36.
- [38] Uno, I.; Eguchi, K.; Yumimoto, K.; Takemura, T.; Shimizu, A.; Uematsu, M.; Liu, Z.; Wang, Z.; Hara, Y.; Sugimoto, N. Asian dust transported one full circuit around the globe. Nature Geoscience, 2009, 2: 557.
DOI: 10.1038/NGEO583
- [39] Andronova, A.V.; Minashkin, V.M. Study microphysical and optical characteristics of dust aerosols of different regions of the USSR. Izvestiya Acad.Sci., Atmos. and Oceanic Physics 1989, 25: 40-44.
- [40] Ivlev, L.S. Aerosol atmospheric model. Problems of Atmospheric Physics 1969, 8: 125-160.
- [41] Kortum, G. Reflectance Spectroscopy: Principles Methods, Applications; New York, 1969.
- [42] Andronova, A.V.; Zhukovsky, D.A.; Mandibles, V.F. Chemical and microphysical characteristics of aerosols on the measuring sites and Shaartuz Esanbay. In Soviet-American experiment on arid aerosol, SPA "Typhoon": St. Petersburg, 1992.
- [43] Zuev, V.E.; Ivlev, L.S.; Kondratyev, K.Y. The new findings of aerosols. Izvestiya USSR Acad.Sci., Atmos. and Oceanic Physics 1973, 9: 371-385.
- [44] Patterson, E.M.; Gillette, D.A.; Stockton, B.H. Complex index of refraction between 300 and 700 nm for Saharan aerosols. Journal of Geophysical Research, 1977, 82: 3153-3160.
- [45] Golitsyn, G.S. Soviet-American experiment on arid aerosol; NGO "Typhoon": St. Petersburg, 1992: 208.

- [46] Kondratyev, K.Y.; Jvalev, V.F. First Global Experiment PIGAP "Aerosol and climate"; Gidrometeoizdat: Leningrad, 1976: 239.
- [47] Krapivtseva, G.M.; Krivchikova, T.V.; Shukurov, A.K. On the synoptic conditions during the period of Soviet-US dust experiment in Tajikistan in September 1989. In Soviet-American experiment on arid aerosol, Hydrometeoizdat: St.Petersburg, 1993: 20-24.
- [48] Mack-Cynon, D. Satellite data on dust storms in Tajikistan. In Soviet-American experiment on arid aerosol, Hydrometeoizdat: St.Petersburg, 1993: 25-26.
- [49] Belan, B.D.; Kabanov, D.M.; Panchenko, M.V. Aircraft sounding of atmospheric parameters in the dust experiment. In Soviet-American experiment on arid aerosol, Hydrometeoizdat: St.Petersburg, 1993: 26-28.
- [50] Golitsyn, G.S.; Shukurov, A.K.; Abdullaev, S.F.; Nazarov, B.I. On the surface are cooling due too dust atmospheric turbidity. In Soviet-American experiment on arid aerosol, Hydrometeoizdat: St.Petersburg, 1993: 67-78.
- [51] Shukurov, A.K.; Nazarov, B.I.; Abdullaev, S.F. On optical depth ratios of dust aerosol in visible and infrared spectra regions. In Soviet-American experiment on arid aerosol, Hydrometeoizdat: St.Petersburg, 1993: 83-88.
- [52] Eguchi, K.; Uno, I.; Yumimoto, K.; Takemura, T.; Shimizu, A.; Sugimoto, N.; Liu, Z. Trans-pacific dust transport: integrated analysis of NASA/CALIPSO and a global aerosol transport model. *Atmospheric Chemistry and Physics*, 2009, 9: 3137-3145.
- [53] Cess, R.D.; Potter, G.L.; Ghan, S.J.; Gates, W.L. The climatic effects of large injections of atmospheric smoke and dust: A study of climate feedback mechanisms with one-and three-dimensional climate models. *Journal of Geophysical Research: Atmospheres* 1985, 90: 12937-12950.
- [54] Budyko, M.I.; Golitsyn, G.; Israel, Y.A. Global climate catastrophe; Gidrometeoizdat: Leningrad, 1986: 160.
- [55] Thompson, S.L.; Schneider, S.H.; Golitsyn, G.S.; else, S.b. Environmental Consequences of Nuclear War. *Environment*, 1986, 28.
- [56] Alperovich, L.I.; Latifov, S.; Mamchenko, T.B. Determining the optical constants of dispersive media in the infrared region. *Colloid Journal* , 1984, 46: 999-1001.
- [57] Nazarov, B.I.; Abdullaev, S.F.; Maslov, V.A. Influence of dust storms on climate change. In Proceedings of International Conference "Problems of modern physics.", Dushanbe: 50-54.
- [58] Nazarov, B.I.; Abdullaev, S.F.; Maslov, V.A. Studies of Temperature Effects of Dust Storms. *Izvestiya. Atmospheric and Oceanic Physics*, 2010, 46: 475-481.
- [59] Abdullaev, S.F.; Nazarov, B.I.; Maslov, V.A. Some results of the aerosol influence of air pollution on climate change. In Proceedings of International Conference "Problems of modern physics.", Dushanbe: 40-44.
- [60] Pachenko, M.V.; Terpugova, S.A.; Bodhaine, B.A.; Isakov, A.A.; Sviridenkov, M.A.; Sokolik, I.N.; Romashova, E.; Nazarov, B.; Shukurov, A.; Chistyakova, E.I. Optical investigations of dust storms during USSR-US experiments in Tadzhikistan, 1989. *Atmospheric Environment, Part A. General Topics* 1993, 27: 2503-2508.



ARTICLE

Land-use Changes Alter Energy and Water Balances on an African *Brachiaria* Pasture Replacing a Native Savanna in the Orinoco llanos

José San-José¹ Rubén Montes^{2*} Rafael Herrera¹ Jair M. Maia³ Nina Nikonova¹

1. Ecology Center, Venezuelan Institute for Scientific Research, AP 20632, Caracas 1020-A, Venezuela

2. Environment Studies Department, Simón Bolívar University, AP 89000, Caracas 1080-A, Venezuela

3. Escola Normal Superior, Universidade do Estado do Amazona, Manaus, Brazil

ARTICLE INFO

Article history

Received: 22 February 2019

Accepted: 5 April 2019

Published Online: 12 April 2019

Keywords:

Energy balance

Seasonal effect

Orinoco lowlands

ABSTRACT

The seasonal changes in the energy balance after the substitution of a herbaceous savanna by a *Brachiaria* field located in the Orinoco lowlands were assessed over an entire year using the eddy covariance technique. Simultaneously, an herbaceous savanna was monitored as a control. This work provides evidence that the vegetation replacement lead to different patterns of energy and water balance. The seasonal trends of the latent heat flux (λE) to available energy (R_a) ratio tended to decrease as senescence increased due to seasonal influence of air humidity mole fraction deficit and soil water content on leaf area index (LAI) and surface conductance (gs). Therefore, the partitioning of the available energy depended on both climatological (i.e., solar radiation, volumetric soil water content and air humidity mole fraction deficit) and biological variables (i.e., conductance behavior and LAI) which were stress-induced. For the wet season, the seasonally averaged daily λE in the *Brachiaria* field (i.e., $0.8 \pm 0.1 \text{ mm d}^{-1}$) was 1.3-fold higher than that in the herbaceous savanna (i.e., $0.6 \pm 0.1 \text{ mm d}^{-1}$) (Mann-Whitney U-test). For the dry season, the value was 2.7 ± 0.6 and $2.2 \pm 0.4 \text{ mm d}^{-1}$, respectively, these means values were not significantly different. In the *Brachiaria* and herbaceous savanna stands, the annual evapotranspiration was 731 and 594 mm year^{-1} , respectively, and the annual ratio of evapotranspiration to precipitation was 0.52 to 0.42 respectively. In *Brachiaria* field, the deep drainage was relatively lower (43% of total precipitation) than that in the herbaceous savanna stand (53%) leaving a similar amount of water to increase soil storage. The current shift in land cover decrease deep drainage and increased λE by water uptake from a pasture with high belowground phytomass and LAI.

1. Introduction

Savannas are a major component of the world's vegetation covering one-sixth of the land surface^[1] and supporting most grazing lands^[2]. In these lands, the

major areas dedicated to extensive beef production are the Neotropical and Australasian savannas. The well-drained Neotropical savannas are characterized by a marked seasonal decrease in dry matter accumulation and palatability as the transpiring surfaces are reduced^[3]. As a result,

*Corresponding Author:

Ruben Montes,

Environment Studies Department, Simón Bolívar University, AP 89000, Caracas 1080-A, Venezuela;

Email: ramontes@usb.ve

constraint on livestock production is evident. Therefore, strategies have been developed to improve land management on the basis of replacing 250×10^6 ha of native vegetation by drought-resistant African pastures in the last 30 years^[4,5,6,7,8]. Specifically, *Brachiaria* is estimated now to cover 20-30 % of South American savannas^[9]. The consequences of this extensive replacement have scarcely been documented^[10]. However, there is major concern over accelerated land degradation and reduced water availability following inadequate pasture management^[11]. The overall aim of this study is to compare the effect of seasonal conditions on the water vapour fluxes of two contrasting surface forcing conditions, as represented by a cultivated *Brachiaria* field and a native savanna side by side under the environment of the Orinoco lowlands. The *Brachiaria* field presents a mat-forming surface and the savanna features an open and erect canopy. This situation might have a disproportionate influence on the surface-forcing condition of the Neotropical plains.

This paper focuses on one dimension of vegetation hydrology: evapotranspiration. To accomplish this task, the micrometeorological approach is suitable^[12,13,14,15,16]. Comparing measurements of water flux vapour as a function of contrasting canopy features and environmental conditions revealed the genetic potential and highly successful adaptation of *Brachiaria* to the Neotropical savanna environment.

This study was carried out within the Orinoco basin (1.1×10^{12} m²), which extends from the northern region of South America ($10^\circ 56' N$; $67^\circ 25' W$) to the Orinoco River in the south ($7^\circ 46' N$; $64^\circ 25' W$). In this regional environment, the patchiness of *Brachiaria* fields and herbaceous savannas provides favorable circumstances for undertaking a comparative study of the water vapour fluxes. Specifically, we considered that if seasonal water demand and supply are determinant of vegetation functioning, then replacing savanna forcing conditions by changes in land use should modify water balance. By contrast, if resources such as soil water and holding capacity turned out not to limit forage development, then we could expect other factors to be determinants.

The aims of the present work were to: 1) understand favorable circumstances for undertaking a comparative study of energy and water vapour fluxes between *Brachiaria* field and herbaceous savanna stand in the Orinoco lowlands using the eddy covariance method; 2) evaluate the processes controlling water vapour transfer as generated by different canopy forcing conditions; and 3) compare the water balance as based on the mass curves, Karelitiotis' approach, between the *Brachiaria* field and the surrounding herbaceous savanna stand. The described

processes and controls might be representative of major Neotropical savannas.

2. Materials and Methods

2.1. Description of the Study-sites and Treatments

At the Experimental Station of Eastern University ($9^\circ 45' N$, $63^\circ 27' W$) in Monagas State, Venezuela, a 40-ha plot covered with herbaceous savanna (i.e., savanna with less than 3% of woody cover) was selected. The infertile soil is a sandy loam belonging to the Maturin series, which is within the oxic-paleustults as classified by Espinoza^[17] in accordance with the U.S. Taxonomy^[18]. The soil infiltration rate ranges from 26 to 36 mm hr⁻¹^[19]. The annual mean precipitation is 1014 mm; the growing season spans May to November with 885 mm. The annual mean class A pan evaporation is 2226 mm and the annual mean temperature is 25.9 °C. Those variables correspond to 38-year mean.

The 40-ha plot was divided into two sub-plots of 20 ha each. A sub-plot was plowed and a field fertilized with 400 kg ha⁻¹ of 12-12-17 NPK and *Brachiaria decumbens* (L.) Staff was planted (August, 16th 2000) to monoculture at a density of 2,000 viable seeds per m². Because of its dense, rigorous mat-forming surface, the *B. decumbens* formed a sward with a closed canopy throughout the year. The carrying capacity of this stand was 1.0 Animal Unit (AU) ha⁻¹. In the other 20-ha sub-plot, the herbaceous savanna (< 3% tree cover) forms an open canopy dominated by species of the genus *Trachypogon* and *Axonopus* with upright tillers.

Previous to the experimental setup, the *Brachiaria* field and the herbaceous savanna sub-plots were regularly grazed under conditions representative of those under normal use in the Orinoco lowlands. At the beginning of the dry season (2008), before microclimatological measurements, the plots were excluded from grazing.

2.2. Leaf Area Index and Belowground Dry Mass

At each sub-plot, the leaf area index was determined monthly with a plant canopy analyzer (LI-2000, LICOR, Lincoln, Nebraska, USA). Ten 1 m x 1 m soil samples were selected monthly at random and the soil was excavated down to 0.5 m. The below-ground phytomass was separated by the flotation method^[20] and oven-dried at 80°C until constant dry mass.

2.3. Measurement Systems

At each sub-plot, energy and water vapour flux densities were measured continuously by the eddy flux covariance

(EC) method^[21,22] using an open path infrared gas analyzer (LI-COR 7500, Lincoln, NE) coupled with a 3D sonic anemometer (Solent A1003R, Gill Instruments, Lymington, UK) at 2 m above the ground for the *Brachiaria* and herbaceous savanna stands. EC was processed every 30 minutes with the EdiRe software (version 1.4.3 1167, R Clement, University of Edinburgh) including despiking, double rotation for deviation of time lag spectral corrections, Webb's corrections^[23] and the atmosphere stability test. Weekly clearing frequency limited the problem of optical contamination to a minimum. Total incoming and outgoing radiation was measured with pyrrometers (S.R.I.4 Solar Radiation Instruments, CSIRO, Victoria, Australia). Short wave solar radiation (R_s) over the vegetation was measured with two pyranometers (LI-200X, LI-COR, Lincoln, NE and CM3 Kipp and Zonen, Delft, Holland), and the albedo with a pyranometer (CM3 Kipp and Zonen). The net radiation (R_n) (i.e., net all-wavelength radiation balance) over the canopy was determined with two net radiometers (Funk-type, model S.R.I.4 Solar Radiation Instruments and Q-7.1 Campbell Scientific, Logan, UT). Net radiation at the soil surface (R_{no}) was measured with a tube radiometer (TRL/M3, Delta-T Devices, Cambridge, U.K.) and a net pyrrometer (S.R.I.4 Solar Radiation Instruments, CSIRO, Victoria, Australia). Measurements were recorded every second and averaged every minute on a Datalogger (21X, Campbell Scientific). All times were local times.

Soil heat flux (G) was measured with a network of ten heat flux plates (S.R.I.9 Solar Radiation Instruments) placed 0.08 m below the soil surface. The net storage of energy (ΔS_E) in the soil column above each soil heat flux plate was determined from the temperature profile^[24] measured with 24 AWG copper-constantan thermocouples placed at 0.2 m intervals from each soil heat flux plate to the soil surface. Before field measurements, the full instrumentation was inter-compared to check for consistency.

At each sub-plot, all instruments were installed near the center. Height for the measurements of vertical fluxes of H_2O and momentum was maximized by using the model for source area/footprint analysis as outlined in^[25] and^[26]. The resulting measurement height over the sub-plots was 2.0 m. The cumulative normalized flux was 0.91 for H_2O .

Volumetric soil water content (θ) was measured daily from a depth of 0.45 m in 0.15 m intervals with a time-domain reflectometer (TDR) (6050X1 Trace System, Soil Moisture Equipment, Santa Barbara, CA). At each soil depth, three probes were buried horizontally and readings were taken with a multiplier (6022 Trace System). Water retention curves were established with a pressure apparatus membrane as outlined in Richards^[27]. Matric

potential ranging from -0.01 to -0.03 MP_a was determined with a porous funnel.

Ancillary meteorological characteristics were recorded above the canopy at the same height as the eddy covariance systems using an automatic weather station (CM6, Campbell Scientific).

Gaps in data were filled by standardized methods^[28,29], and the dataset was completed with measured ancillary data describing study sites, vegetation and climate. For the water and energy fluxes, symbols and notations follow Reifsnyder et al^[30].

The pathway for H_2O diffusion between canopy and atmosphere was described by surface (g_s) and aerodynamic (g_a) conductances. Canopy-to-air humidity mole fraction difference was estimated as the difference between the saturation humidity mole fraction at the canopy temperature (T_c)^[31] and the air humidity mole fraction at the canopy surface. This, in turn, is determined using the latent heat flux equation on the basis of measurements from vapour pressure at the weather station, the latent heat flux (λE) and the aerodynamic conductance.

To assess the effect of volumetric soil water content on the upper limit of the daily latent heat flux (λE) to available energy (R_a) ratio, a ben-cable form of a piece-wise linear model with nonlinear quantile regression^[32] was used. The 0.90 to 0.99 quantiles provide estimates near the upper boundary of the percentage of $\lambda E/R_a$ ratio as it varied with θ ^[33].

2.4. Aerodynamic and Surface Conductance

The pathway of the water vapour diffusion and heat between the atmosphere and the canopy was expressed by the aerodynamic (g_a) and surface (g_s) conductances. Aerodynamic conductance was estimated from the sonic anemometer measurements considering the additional boundary layer conductance to momentum flux and the atmosphere stability^[34,35] as:

$$g_a^{-1} = \frac{u}{u_\psi^2} + \frac{1}{ku_\psi} \left[\ln \left(\frac{Z_0}{Z_H} \right) + \Psi_H + \Psi_M \right] \quad (1)$$

Where u is the longitudinal wind speed at the reference height, u_* is friction velocity, k is on Karman's constant, Z_0/Z_H is the proportion of the momentum roughness lengths for momentum (Z_0) and heat (Z_H) transfer^[35] and Ψ_H and Ψ_M are the integrated adiabatic correction factors for heat and momentum, respectively^[36]. The proportion was taken as 10, a typical figure for a homogeneous canopy^[37].

Surface conductance was estimated by the inverse form of the Penman-Monteith equation^[38,39] using measure-

ment of latent (λE) and sensible (H) heat fluxes as well as specific humidity deficit (D) in the equation:

$$g_s^{-1} = \left[\frac{\varepsilon + 1}{g_a} \right] \left[\frac{\varepsilon A}{(\varepsilon + 1)(\lambda E)} \right] + \frac{\rho_a D}{E} \quad (2)$$

Where ε is the rate of change of saturate humidity with temperature, A is the addition of the available energy for the canopy (A_c) and soil (A_s) (i.e., $A = A_c + A_s$), ρ_a is the molar density of air and E is the evaporation rate.

2.5. Conductance and the Omega Factor

The degree of coupling (Omega factor, Ω)^[40] between the canopy and the atmosphere was calculated from the estimates of aerodynamic (g_a) and surface (g_s) conductances to examine the relative contribution of radiation and specific humidity deficit on transpiration using the following equation:

$$\Omega^{-1} = 1 + \left[\frac{\gamma}{\Delta + \gamma} \right] \left[\frac{g_a}{g_s} \right] \quad (3)$$

Where Δ is the slope of the saturation vapour pressure as a function of the air temperature and γ is the psychrometric constant.

This factor describes how closely the vapour pressure deficit at the canopy surface is linked to that in the air outside the canopy boundary layer. At the same time, it allows examination of the contribution of radiation and saturation deficit to the transpiration rate^[41]. Ω approaches 1 in well-watered and aerodynamically smooth canopies, where transpiration rate is driven by canopy to air saturation deficit. Thus, when $\Omega \approx 1$, LE tends to equilibrium evapotranspiration as described by the Priestley-Taylor equation. When $\Omega \approx 0$, LE is closely coupled to the atmospheric saturation deficit^[41].

2.6. Modeling Surface Conductance by Nonlinear Least Square-optimization

For the hourly data of the seasons, the g_s for the surfaces was expressed as a function of the ancillary meteorological measurements (Q_s = solar radiation, T_a = air temperature, D_a = air humidity mole fraction deficit, $\delta\theta$ = volumetric soil water content deficit and $\delta\theta_{max}$ = maximum value of $\delta\theta$) by nonlinear least-square optimization^[38,42,43]. An environmental variable analysis was performed to decrease the redundancy of the environmental variates. Thus, the variables were subject to a preliminary analysis by using the variance inflation factor of variables in a multiple regression equation^[44]. Collinear variables (i.e., solar radiation and air temperature) were deleted from the variable set. As a result, the best model was $g_s = g_{smax}$

$f_1(Q_s) f_2(D_a) f_3(\delta\theta)$, where g_{smax} was the maximum measured g_s and the equations

$$f_2(D_a) = 1 - K_3 D_a \quad (4)$$

$$f_3(\delta\theta) = 1 - e^{-K_4 \delta\theta} \quad (5)$$

$$K_4 = K_5 (\delta\theta - \delta\theta_{max}) \quad (6)$$

Where g_{smax} (i.e., K_1) and $K_2 - K_5$ were parameters.

2.7. Water Cycle Dynamics

The water cycle dynamic data was analyzed by using the Chow and Kareliotis' approach^[45] as based on the mass curves. Thus, the mass balance equation, in which the system component of precipitation (Pc), conceptual water storage (S), measured as temporal changes in the soil volumetric moisture content Θ , at deep layer 0.5 m evapotranspiration (λEc) and run off (Rt= zero in our case) are considered as stochastic processes. The water drained below the 0.5 m depth is considered as the differences of the three component stochastic processes (Pc- λEc -S)

3. Results

3.1. Physical Environment

Climatic seasonality was marked by 99.9 % of the total annual precipitation (i.e., 1397.8 mm) falling during the wet season (Figure 1A). During the dry season, the weather was usually stable with 85 days receiving 83% of the clear sky radiation. Maximum daily solar radiation increased from 20.3 MJ m⁻² day⁻¹ in the dry season to 21.1 MJ m⁻² day⁻¹ in the wet season (Figure 2A). On an annual basis, the stands received 5.9 GJ m⁻² yr⁻¹. Despite receiving equal annual sums of solar radiation, annual R_n was greater over the *Brachiaria* field (3.1 GJ m⁻² yr⁻¹) than over the herbaceous savanna stand (2.7 GJ m⁻² yr⁻¹). Daytime averaged hourly temperature ranged from 25.3 to 31.4 °C in the dry season and from 20.8 to 31.4 °C in the wet season (Figure 2B). During the wet season, there were days when the daytime and nighttime averaged hourly temperature overlapped from 0.5 to 1.5 °C. Air humidity mole fraction deficit increased during the dry season and reached a maximum of 24.9 mmol mol⁻¹ at the end of the season (Figure 1B).

The volumetric soil water content (θ) was integrated across the upper 0.45 m of the soil profile (Fig. 2C). The daily amount of soil water in the *Brachiaria* and herbaceous savanna stands remained different. With the onset of the dry season, vegetation and the atmosphere depleted water from the soil profile and the vegetation cover dried out. Thus, θ in the *Brachiaria* field was below wilting

point (WP) (i.e., $0.087 \text{ m}^3 \text{ m}^{-3}$) from March to April (i.e., 36 days). In contrast, in the herbaceous savanna stand, it was below WP only in April (i.e., four days). As a consequence, the LAI of the *Brachiaria* field and herbaceous savanna stand became reduced with plant senescence to 1.15 ± 0.08 and $0.45 \pm 0.06 \text{ m}^2 \text{ m}^{-2}$, respectively. This LAI of *Brachiaria* was significantly higher than that in herbaceous savanna stand (Mann-Whitney U-test in Sokal and Rohlf^[46]). The rapid decrease in vegetation growth was associated with low soil water-holding capacity of the sandy soils and a high air humidity mole fraction deficit (Figure 1B). As the vegetation growth proceeded during the wet season, θ for the *Brachiaria* field and herbaceous savanna stand reached a maximum of 0.327 and $0.339 \text{ m}^3 \text{ m}^{-3}$, respectively (Figure 2C). During the measuring period, θ in the *Brachiaria* and herbaceous savanna soils was above field capacity (i.e., $0.220 \text{ m}^3 \text{ m}^{-3}$) on 152 and 194 days, respectively. Distribution of rainfall and θ variability were determinants of the length of the growing season for both stands, which was shorter in this study (185 days) than that (220 days) for the 38-years average in the same area for prevailing conditions.

3.2. Radiation Balance

During the dry season, the seasonal average daily (R_n/R_s) ratio over the *Brachiaria* field was 0.55 ± 0.01 , 25 % higher than that in the herbaceous savanna stand (0.44 ± 0.02) (Mann-Whitney U-test). During the wet season, the value for the *Brachiaria* field (0.53 ± 0.02) was not significantly different from that for the herbaceous savanna stand (0.49 ± 0.063) (Mann-Whitney U-test). The difference (Mann-Whitney U-test) during the dry season between outgoing short wave radiation over both stands ($-2.4 \pm 0.3 \text{ MJ m}^{-2} \text{ d}^{-1}$ for the *Brachiaria* field and $-2.0 \pm 0.2 \text{ MJ m}^{-2} \text{ d}^{-1}$ for herbaceous savanna) and outgoing long-wave radiation ($-39.9 \pm 0.6 \text{ MJ m}^{-2} \text{ d}^{-1}$ for *Brachiaria* and $-41.9 \pm 0.7 \text{ MJ m}^{-2} \text{ d}^{-1}$ for herbaceous savanna stand) as well as during the wet season in outgoing short wave radiation over the stands ($-2.5 \pm 0.5 \text{ MJ m}^{-2} \text{ d}^{-1}$ for *Brachiaria* field and $-2.1 \pm 0.4 \text{ MJ m}^{-2} \text{ d}^{-1}$ for herbaceous savanna stand) and outgoing long-wave radiation ($-37.3 \pm 0.7 \text{ MJ m}^{-2} \text{ d}^{-1}$ for *Brachiaria* field and $-38.2 \pm 0.3 \text{ MJ m}^{-2} \text{ d}^{-1}$ for herbaceous savanna stand) were associated with site factors such as albedo and surface temperature.

3.3 Energy Balance Closure and Seasonal Energy Fluxes

In the *Brachiaria* field and herbaceous savanna stand, the sensible flux (H), latent heat flux (λE) and available energy (i.e., R_n) were determined concurrently and the

outcomes compared by regression statistics^[47]. For both study-sites, the relationships showed a high significant slope close to unit (i.e., 0.98 and 0.99, respectively) ($r^2 = 0.92$ and 0.91 , respectively) and the mean square error (RMSE) 18 and 19 Wm^{-2} , respectively.

A comparison between the *Brachiaria* field and herbaceous savanna stand in daily evapotranspiration (λE) and the effect of the seasonal conditions are shown in Figure 1A-D. During the dry season, λE over the two contrasting stands was less than 1.3 and 0.8 mm d^{-1} , respectively as soil water decreased. With onset of the wet season, λE at both stands increased day by day until peaking at 3.7 and 3.5 mm d^{-1} , respectively. Annual λE in the *Brachiaria* field was 731 mm and the herbaceous savanna stand was 594 mm .

3.4. Seasonal Partitioning of Available Energy

During the seasons, two typical daily trends of fluxes in the *Brachiaria* field and herbaceous savanna stand are shown in Figure 3A-B. After replacement of the herbaceous savanna, the changes in forcing surface conditions and water availability contribute to the measured differences. On the typical sunny day during the dry season (March, 12th), R_s over the *Brachiaria* field and herbaceous savanna stand increased to a maximum value of 966 Wm^{-2} . As a result of canopy senescence and decreased LAI, the ratio of R_n above to R_n below the canopy in both stands reached 0.33 ± 0.21 and 0.25 ± 0.16 , respectively. These values were not significantly different (Mann-Whitney U-test). The energy flux density of H and λE showed a sinusoidal trend; however, λE presented lower value than H from late morning to afternoon hours. During the midday hours, the H/R_n ratio over both stands reached 0.58 and 0.82 , respectively. Bowen ratio (β) over the stands reached a maximum of 2.7 and 8.9 , respectively. On a typical day during the wet season (October, 10th), the maximum R_s was 828 Wm^{-2} . The *Brachiaria* field and herbaceous savanna stand canopies heated and the Bowen ratio was positive for most daytime with figures related to site conditions. As λE increased over both sites, β reached values of 0.2 and 0.4 , respectively.

On the days during the dry and wet seasons hourly soil storage flux (ΔS_H) in the *Brachiaria* and herbaceous savanna stands (Fig. 3A-B) are a major component of R_n , but decreased during the afternoon hours. Around noon of the day during the dry season, the average daytime convective-to-conductive heat-sharing fraction ($\Delta S_H/R_n$) ratio ranged from 0.18 to 0.80 in the *Brachiaria* field and from 0.10 to 0.60 in the herbaceous savanna stand. On the day during the wet season, the $\Delta S_H/R_n$ ratio spanned from 0.07 to 0.60 and from 0.02 to 0.70 , respectively. These results indicated that soil

constituted a differential sink/source of heat.

In the *Brachiaria* and herbaceous savanna stands, the difference between the canopy and the air in temperature (Fig. 3E-F) reached up to 1.3 and 0.6 °C, respectively. On the day during the dry season, the canopy-to-air humidity mole fraction difference (D_a) rose through the morning hours from 1.9 and 1.4 mmol mol⁻¹ at predawn respectively, to 47 and 50 mmol mol⁻¹ at 12:00 and 14:00 hours, respectively. The variations of the fluxes indicate that λE was affected by both D_a and R_n . For both stands, the multiple regression of λE as a function of R_s and D_a was significantly fitted. In the case of the *Brachiaria* field, the expression was $\lambda E = 21.21 + 0.66 R_s + 1.40 D_a$, $p < 0.0001$ for the dry season. In the herbaceous savanna stand, the expression was $\lambda E = 14.51 + 0.01 R_s + 0.44 D_a$, $p < 0.0097$ for the dry season. Around noon, during the dry season, g_s in the *Brachiaria* field rose to reach its peak (i.e., 0.6 mol m⁻² s⁻¹) in the very early morning hours. Thereafter, it decreased rapidly to reach its lowest value during the rest of the day. For both stands, the multiple regression of λE as a function of solar radiation and air humidity mole fraction deficit was significantly fitted. Thus, in *Brachiaria* field, the relationship was $\lambda E = 27.2 + 0.06 R_s + 1.75 D_a$, $p < 0.0001$ for the wet season. In the herbaceous savanna stand, the expression was $\lambda E = -5.77 + 0.24 R_s + 2.12 D_a$, $p < 0.0001$ for the wet season. Surface conductance in the stands remained at low values (< 1.0 mol m⁻² s⁻¹). On the day during the wet season, g_s over the *Brachiaria* field increased in the daytime rising to a plateau (1.19 ± 0.40 mol m⁻² s⁻¹) between 7:00 and 15:00 hours. Thereafter, it decreased to low values during the nighttime. Over the herbaceous savanna stand, the course was different. In this stand, g_s increased to i.e., 0.9 – 1.9 mol m⁻² s⁻¹ during the very early morning hours. Thereafter, it decreased and reach values close to zero during mid-day hours. The trend of the surface conductance was associated with canopy-to-air mole fraction difference. On the day during the wet season, g_s over both stands increased with R_s and decreased with canopy-to-air humidity mole difference (D_a) (Fig. 3A-F). The trends of wind speed and aerodynamic conductance (g_a) (Fig. 3C-D) were relatively lower in the day during the wet season as compared to that in the day during the dry season. The magnitude of g_a (Fig. 3C-D) was always higher than that of g_s , except for the morning hours of the wet season.

3.5. Proportion of Daily Available Energy (R_a) Used for Evapotranspiration as a Function of Volumetric Soil Water Content, Leaf Area Index and Surface Conductance

The response of evapotranspiration in the *Brachiaria*

field and herbaceous savanna stand to θ was quantified by using the daily latent heat flux-to-available-energy ratio (Fig. 4) as originally outlined in Denmead and Shaw^[48]. Maximum daily $\lambda E/R_a$ ratio was represented by using a 99th quantile piece-wise linear regression. The results indicate that upper boundary of the *Brachiaria* field envelope was higher than that for the herbaceous savanna. The regression analysis identified the breakpoint (i.e., the critical θ at which maximum daily $\lambda E/R_a$ is attached) in the interval $0.110 \pm 0.022 \text{ m}^3 \text{ m}^{-3}$ and $0.105 \pm 0.021 \text{ m}^3 \text{ m}^{-3}$, respectively. The equation for the quantifying the upper bound on $\lambda E/R_a$ ratio between minimum and critical θ was daily $\lambda E/R_a = 13.480 \theta - 0.621$ for the *Brachiaria* field and daily $\lambda E/R_a = 19.989 \theta - 1.401$ for the herbaceous savanna stand. Therefore, the *Brachiaria* field transpired at a faster rate, despite lower θ .

In the *Brachiaria* and herbaceous savanna stands, the seasonal trend of the ratio $\lambda E/R_a$ was explained by the difference in LAI development (Fig. 5). Seasonal variations in LAI were coupled with changes in moisture availability. Maximum LAI for the *Brachiaria* was (i.e., $2.4 \pm 0.2 \text{ m}^2 \text{ m}^{-2}$) higher than that (i.e., $2.1 \pm 0.2 \text{ m}^2 \text{ m}^{-2}$) for the herbaceous savanna stand. These results indicated that $\lambda E/R_a$ was depressed at low θ because LAI decreased with θ .

Measuring hourly g_s ranges permitted assessing how variation in maximum hourly g_s affected the daily $\lambda E/R_a$ ratio. For both stands, data were fitted by a logarithmic relationship (Fig. 6). In *Brachiaria* field the ratio was less affected as maximum hourly g_s increased from 0.4 to 4.0 mol m⁻² s⁻¹. Below 0.4 mol m⁻² s⁻¹ (i.e., the critical conductance) the ratio experienced a sharp reduction as a function of the maximum hourly g_s . In the herbaceous savanna stand the ratio was slightly affected from 0.4 to 1.2 mol m⁻² s⁻¹, and the critical ratio was similar to that in *Brachiaria* field. However, there was a clear difference between stands in canopy roughness and physiological behavior, and these factors influenced energy exchange and partitioning.

3.6 Modeled Surface Conductance Versus Environmental Variables

The modeled surface conductance as a function of environmental variables indicated that the seasonal trend of g_s showed the influence of the air humidity mole fraction deficit (D_a) and soil water content deficit ($\delta\theta$). The model accounts for 68 % and 70% of the variance of g_s over the *Brachiaria* field and herbaceous savanna stand, respectively, as a function of maximum g_s , D_a and $\delta\theta$ (Table 1). Comparison of the parameters of the surface conductance model for the *Brachiaria* field and herbaceous savanna stand as determined by nonlinear square optimization in-

dicates that in the *Brachiaria* field, response of g_s to the changes in the volumetric soil water content deficit was higher than that in the herbaceous savanna stand.

3.7 Water Cycle Dynamics

The seasonal trends of cumulative precipitation and evapotranspiration (i.e., P_c and λE_c , respectively) and soil water storage (S) in the 0.0-0.5 m depth for the *Brachiaria* field and herbaceous savanna stand are shown in Figure 7. λE_c in the *Brachiaria* field (731 mm year^{-1}) was higher than herbaceous savanna stand (594 mm year^{-1}), respectively. Soil water storage and water drained below 0.5 m soil layer was lower in *Brachiaria* field (122 mm year^{-1} and $53.1 \text{ mm year}^{-1}$) than herbaceous savanna stand (135 mm year^{-1} and 63 mm year^{-1}), respectively.

4. Discussion

In this analysis, the effect of land-use changes from neotropical herbaceous savannas to cultivated paleotropical grass was evident on roughness-forcing conditions and energy partitioning. The seasonal dynamic of λE could be mainly attributed to the trend of atmospheric demand and water supply for vegetation development. Thus, temporal trends in demand (i.e., energy availability) and supply (i.e., soil water content and leaf-area index) were associated with this tendency.

4.1. Weather and Climate

Seasonal difference between the *Brachiaria* field and herbaceous savanna stand in R_n was due to albedo and surface heating (i.e., difference from incoming to outgoing long wave radiation). In the dry season, the seasonally averaged daily albedo in the stands was 0.15 ± 0.01 and 0.12 ± 0.02 , respectively. The divergence between stands in dry seasonally averaged daytime albedo was significantly different (Mann-Whitney U-test). In the wet season, the value was 0.16 ± 0.01 for the *Brachiaria* field and 0.14 ± 0.03 , for the herbaceous savanna stand. The deviation between stands in wet seasonally average daytime albedo was not significantly different (Mann-Whitney U-test). The seasonally averaged daily surface heating in the *Brachiaria* field and herbaceous savanna stand was -5.31 ± 0.25 and $-7.39 \pm 0.30 \text{ MJ m}^{-2} \text{ d}^{-1}$, respectively, for the dry season and -4.79 ± 0.20 and $-5.9 \pm 0.20 \text{ MJ m}^{-2} \text{ d}^{-1}$, respectively for the wet season. The difference between stands in the seasonally averaged daily surface heating was different significantly (Mann-Whitney U-test) for the dry and wet seasons, respectively. In the Orinoco lowlands, the contrast between the two key exotic grasses (i.e., *Brachiaria* as reported here) and *Andropogon* field (as outlined in San

José et al [3]) and the herbaceous savanna stand in albedo and surface heating values might lead to differences in mesoscale circulation and cloud convection as described by Keenan et al [49]. There is also evidence of a feedback mechanism between land use change and shifts in resultant climate. That is decline in rainfall over cleared and cropped landscape in Western Australia [50]. In the case of burned and unburned savannas in northern Australia, Beringer et al [51] have found that the consequent contrasting albedo and heating values may significantly modify precipitation patterns.

During the dry season, the mat-forming surface of *Brachiaria* field with high albedo absorbed less energy than that in the upright canopy savanna, where the canopy temperature was consequently higher. The difference in seasonal albedo was associated with the changes in LAI. Similar results have been reported for the African tall grass *Andropogon* field and herbaceous savanna stand of the Orinoco lowlands [3].

4.2 Evapotranspiration and Sensible Heat. Water Cycle Dynamic

The seasonally averaged daily H flux was the main source of the available energy (R_n) in the *Brachiaria* field ($7.036 \pm 1.186 \text{ MJ m}^{-2} \text{ d}^{-1}$) and herbaceous savanna stand ($4.843 \pm 1.008 \text{ MJ m}^{-2} \text{ d}^{-1}$) during the dry season and it was relatively higher in the *Brachiaria* field (Mann-Whitney U-test). By contrast, λE over both stands was the main component of the available energy during the wet season. However, seasonally averaged daily latent heat flux (λE) for the *Brachiaria* field (6.183 ± 1.427) was not significant different from that for the herbaceous savanna stand ($5.609 \pm 1.206 \text{ MJ m}^{-2} \text{ day}^{-1}$) (Mann-Whitney U-test). The results indicate that during the dry and wet seasons, the monthly averaged daily evapotranspiration rate in the *Brachiaria* field (i.e., 0.8 ± 0.1 and $2.7 \pm 0.6 \text{ mm day}^{-1}$, respectively) was 1.3- and 1.2-fold higher than those measured in the herbaceous savanna stand (i.e., 0.6 ± 0.2 and $2.2 \pm 0.2 \text{ mm day}^{-1}$, respectively) (Mann-Whitney U-test). In the climate seasonality marked conditions by 0.1% of total precipitation occurring during the dry season, the monthly averaged daily λE in the stands was lower than that measured over the Brazilian campo sujo, campo cerrado and campo denso (i.e., $1.1 - 2.5 \text{ mm day}^{-1}$) [52,53,54,55,56]. By contrast, the monthly averaged daily λE during the wet season was similar for the studied stands ($2.2 - 2.7 \text{ mm day}^{-1}$) and Brazilian cerrados (i.e., $2.2 - 3.7 \text{ mm day}^{-1}$) [57] with similar precipitation events.

For the *Brachiaria* field and herbaceous savanna stand, the annual evapotranspiration was 731 and 594 mm year^{-1} , respectively (Fig. 7). λE for both stands was similar

to that reported for a tall grass *Andropogon* field and a herbaceous savanna (721 and 538 mm yr⁻¹, respectively) occurring under similar environmental conditions [3]. By contrast, in the Brazilian cerrado denso and cerrado, the mean annual λE was 823 and 689 mm yr⁻¹, respectively [56]. For *Eucalyptus* open-forest savannas in northern Australia, λE was 870 mm yr⁻¹[58]. These differential responses could be related to woody cover density such as has been reported by Bucci et al [59] for a transpiration gradient along a tree increment in the cerrado and cerrado denso.

For the *Brachiaria* and herbaceous savanna stands, the annual ratio of evapotranspiration to precipitation was 0.52 and 0.42, respectively. This ratio for the *Brachiaria* field was similar to that reported for *Andropogon* field (0.49); whereas the herbaceous savanna stand ratio was lower than those in other herbaceous savannas (0.65) growing in the Orinoco lowlands which featured 1066 mm of precipitation [3]; and lower also than in the annual grasslands (0.54-0.58) in Ione, California with 559 mm of precipitation [60].

During the dry season, evapotranspiration of the stands proceeded according to the soil water storage levels (Fig. 7). When the rainfall period began, evaporation rose markedly and water drained from the upper (0.50 m) soil layers to layer soil > 0.5 m depth (i.e., $P_c - \lambda E_c - S$). In the *Brachiaria* field, 52 % of the precipitation returned to the atmosphere via evapotranspiration and a smaller amount of water entered soil storage as compared to the herbaceous savanna stand. In both stands, water storage increased from the beginning of the wet season until the middle of the season and λE depended on both precipitation and soil water storage.

The water drained below 0.5 m layer in *Brachiaria* field was relatively lower (43 % of total precipitation) than that in the herbaceous savanna stand (53 %). In the *Andropogon* field, the value was 42% [3]. As consequence, the available water for human consumption, industrial activities and food production was reduced in the exotic grass species by 16-17 %.

These results indicate that after savanna was replaced by *Brachiaria* field the regulation of λE by community functional features (i.e., surface conductance, LAI and root system), phenology and water supply determined a different water balance. Thus, water loss by evaporation in the replaced herbaceous savanna was increased 1.2-fold. In the case of *Andropogon* the value was 1.3 fold [3]. By contrast, after a native oak woodland was replaced by grasslands [61] evapotranspiration dropped from 513 to 378 mm yr⁻¹ (i.e., 26 %). In the cultivated Sahel, the fallow replaced by millet crops led to a water loss of 343 to 237 mm yr⁻¹ (i.e., 30 %) [62]. Similarly the hydrological cycle

of the cerrado savannas of central Brazil was modified as native woody vegetation was replaced by exotic grasses and agricultural crops [55]. The comparative differences might be related to tree density.

4.3 Processes and Controls

The partitioning of the available energy into λE and H , and the resulting effect on boundary layer processes depended on both biotic and abiotic factors. The relative control of the climatological variables was elucidated from volumetric soil water content and air humidity mole fraction deficit. The biological responses were adequately estimated by conductance behavior and leaf area index. As the dry season proceeded, the evaporation fraction of the available energy tended to decrease with increasing senescence due to the seasonal influence of control effects such as air humidity mole fraction deficit, and soil water content on leaf area index and surface conductance.

The annual variations in the daily $\lambda E/R_a$ ratio at each stand were in phase with variation in soil moisture content, LAI and surface conductance (Fig. 4-6). When the ratio was expressed as a function of θ , the upper bound of the envelope for the *Brachiaria* field (0.87) was greater than that for the herbaceous savanna stand (0.80). In the case of the herbaceous savanna stand, the seasonal averaged ratio for the wet season (0.68 ± 0.10) was similar as that reported for a tree and scrub woodland cerrados, accounting for 0.60 during the wet season [52]. In the *Brachiaria* field and herbaceous savanna stand, a sharp decrease in the ratio occurred below the critical soil water content (θ_c) at both stands (i.e., 0.111 ± 0.022 and 0.107 ± 0.021 m³ m⁻³, respectively). Thus, the *Brachiaria* field was more tolerant of low soil water potential than that in the herbaceous savanna stand. Similar results for *Brachiaria* have been reported by Mattos et al. [63]. The difference between stands in the response of the $\lambda E/R_a$ ratio as a function of θ was related to the total below-ground dry mass as *Brachiaria* partitioned a larger value (720 ± 65 gm⁻²) than that in the herbaceous savanna stand (379 ± 48 gm⁻²) (Mann-Whitney U-test). Therefore, the *Brachiaria* seems to withstand water-stressed conditions on the basis of an extensive root system exploring large soil volume over a long period. Furthermore, the root system of *Brachiaria decumbens* features height hydraulic conductivity under conditions of high evapotranspiration and water stress [63,64]. These traits are likely to delay the onset of the dry season.

Over the *Brachiaria* field and herbaceous savanna stand, the average daily $\lambda E/R_a$ ratio was 0.23 ± 0.04 and 0.21 ± 0.03 , respectively, during the dry season, and 0.66 ± 0.10 and 0.68 ± 0.09 , respectively, during the wet

season. Similar seasonal ratios have been reported for intensively farmed land in the paleotropical savannas of Eastern Burkina Faso^[65]. In this location, the $\lambda E/R_a$ ratio was 0.23 in the dry season and 0.71 in the wet season. This similarity between the Neotropical and Paleotropical sites in seasonal ratios might be related to a comparable development of the leaf area index. Here, monthly averaged daily $\lambda E/R_a$ ratio for both stands increased similarly as LAI does (Fig. 5). Thus, LAI development explained the seasonal changes of the ratio across the pasture-savanna mosaic. As θ directly affected the $\lambda E/R_a$ ratio more strongly when the soil was markedly dry. The difference between stands in the linear relationship of $\lambda E/R_a$ on LAI was not significant when the test of heterogeneity between the slopes was carried out^[46].

For the *Brachiaria* field and herbaceous savanna stand, the daily $\lambda E/R_a$ ratio was logarithmically related to maximum hourly g_s (Fig. 6). Similarly, the logarithmic increase of $\lambda E/R_a$ with increase in maximum hourly g_s has also been reported for a savanna woodland continuum^[3]. The short-closed canopy of *Brachiaria* with maximum hourly g_s exceeding the critical value $0.8 \text{ mol m}^{-2} \text{ s}^{-1}$ was less-coupled to the atmosphere as compared with the open tall savanna when the daytime averaged hourly Ω (Ω) was 0.21 ± 0.15 and 0.12 ± 0.05 , respectively, for the wet season. These values were significantly different (Mann-Whitney U-test). In the herbaceous savanna stand, the reduction in maximum hourly g_s of less than the critical value $0.4 \text{ mol m}^{-2} \text{ s}^{-1}$ was related to a sharp decrease in the ratio. In a tree and scrub woodland cerrado, similar critical values of g_s ($0.4\text{--}0.5 \text{ mol m}^{-2} \text{ s}^{-1}$) were reported during most of the daytime hours^[52]. This measured low critical g_s in the herbaceous savannas might be acting as a water limiting mechanism. Here the silica body deposited around the stomatal apparatus in the native grasses^[66] might contribute to decreased stomatal aperture. Low critical g_s in native grasses have been reported by Baruch et al.^[67]. They reported that at a leaf-air vapour pressure difference less than 1 KPa, g_s was 40% lower in the native grasses from the Orinoco lowlands than that in the exotic grasses from the Paleotropical savannas.

The modeled surface conductance was a function of the air humidity mole fraction deficit (D_a) and volumetric soil water content (θ). Similar explanatory factors have been reported for other Neotropical, Paleotropical and Australian savannas^[3,13,14,39,65,68,69,70]. Specifically, in *B. decumbens*, Mattos et al.^[63] have found that stomatal conductance varied directly with the volumetric soil water content. Whitley et al.^[71] compared the parameter values of a modified Jarvis-Stewart model applied across five contrasting Australian woodlands and forests. Similarly to

the Orinoco stands, they stressed the relative effects of the vapour pressure deficit and soil moisture on canopy water flux.

5. Conclusions

In this study, evidence is provided showing that replacement of the native herbaceous vegetation by a *Brachiaria* field led to different patterns of energy and water balance. Large expanses of savanna have been transformed into *Brachiaria* fields. Therefore, the future pasture-dominated ecosystem could come to occupy large areas of the savannas. We found that the current shift in land cover decreases soil water storage from 740 to 612 mm and increases λE because of more water uptake by the pasture due to *Brachiaria*'s denser root system and higher LAI. Considering that the Orinoco lowland vegetation is an herbaceous savanna-woodland continuum, the hydrological effect of savanna conversion seems to depend upon tree density. Thus, the renewal of herbaceous savanna by a *Brachiaria* and *Andropogon* fields^[3] contribute to an evapotranspiration increase of 1.23 and 1.31 fold-times, respectively. These conditions might affect 10% of the Orinoco lowlands^[72], whereas, the replacement of a savanna woodland by the African *Brachiaria* and *Andropogon*^[3] lead to an evapotranspiration decrease of 1.0 – 1.5%. Understanding water use efficiency of these vegetations could be important for delineating environmental changes and energy balance on the regional scale. Furthermore, these variations could have a modifying feedback on the climate^[73,74,75,76] and water budget^[77]. In contrast, models elaborated by Hoffmann and Jackson^[78] indicate that precipitation and evapotranspiration could be reduced by 10 % and 6%, respectively, whereas temperature could increase by 0.5°C , as could the frequency of dry periods. They have speculated that the regional conversion could increase deep soil water storage and reduce λE because of less water uptake by deep roots, especially during the dry season. As a consequence, in this scenario, the climate could become drier. In the particular case of the replacement of a herbaceous savanna by a grassfield, the relative response appears to depend upon the disturbance conditions of the displaced savanna.

Acknowledgements

This work was conducted as part of the Savanna Bio-productivity project (MAB/UNESCO) of 544 IVIC. We appreciate the technical assistance of Prof. Daniel Bailey (Simón Bolívar University).

Supplement

Table 1. Parameters (K_3 and K_6) of the surface conductance model (i.e., $g_s = g_{s,max} f_1(D_a) f_2(\delta\theta)$) for a *Brachiaria* field and a savanna of the Orinoco lowlands as determined by non-linear square optimization

Where $K_1 = g_{s,max}$ for *Brachiaria* and native savanna was 2.80 and 0.78, respectively. D_a = humidity mole fraction deficit and $\delta\theta$ = volumetric soil water content deficit. Level of confidence 95% ($\alpha = 0.050$)

Stand	Estimate	Standard Error	t-value	p-level	Low Conf. Limit	Upper Conf. Limit	
Brachiaria	K_3	0.025947	0.000904	28.71231	0.00	0.024175	0.027718
	K_6	1.729402	0.047656	36.28899	0.00	1.635964	1.822841
Savanna	K_3	0.022648	0.000536	42.26716	0.00	0.021597	0.023698
	K_6	2.393610	0.039077	61.25413	0.00	2.316996	2.470225

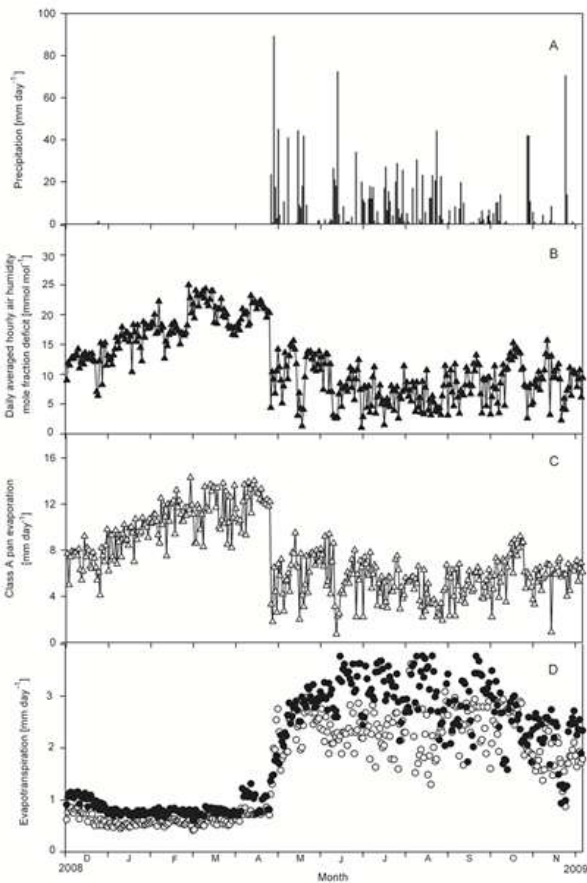


Figure 1

Figure 1. (A) Precipitation, (B) Daily averaged hourly air humidity mole fraction deficit, (C) Class A pan evaporation and (D) Evapotranspiration in a *Brachiaria* field (●) and a herbaceous savanna (○) of the Orinoco Lowlands.

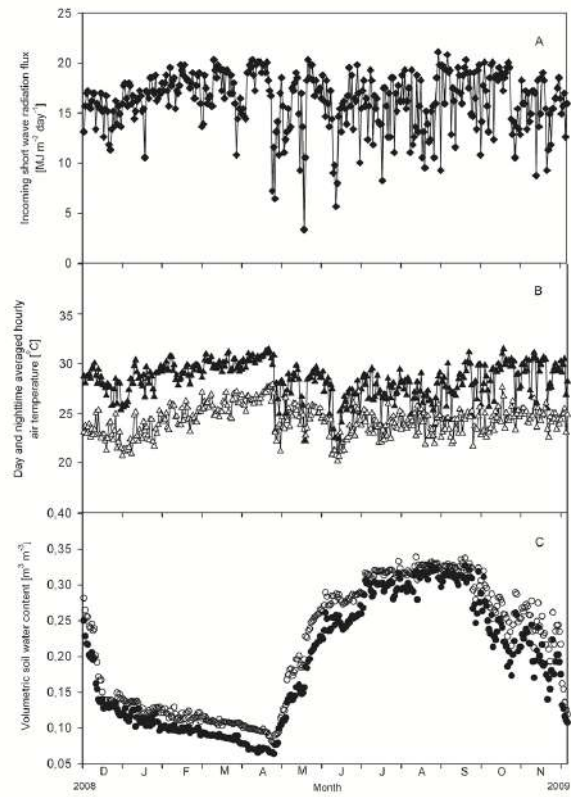


Figure 2

Figure 2. (A) Incoming short wave radiation flux, (B) Day (▲) and nighttime (△) averaged hourly air temperature, and (C) Volumetric soil water content in a *Brachiaria* field (●) and a herbaceous savanna (○) of the Orinoco lowlands.

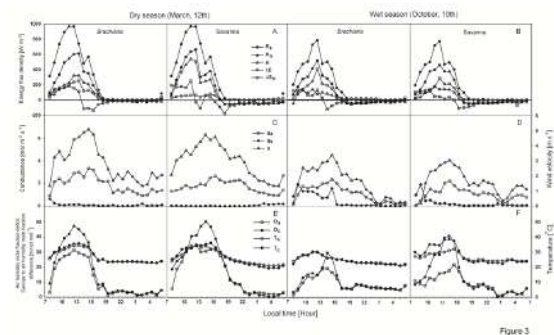


Figure 3

Figure 3. (A-B) Hourly values of energy budget components in a vegetational mosaic of the Orinoco lowlands. R_S = incoming short wave radiation; R_n = net radiation; H = sensible heat flux; λE = latent heat flux; ΔS_H = soil net storage heat flux. (C-D) Aerodynamic (g_a) and surface (g_s) conductances, and wind velocity (u). (E-F) Air humidity mole fraction deficit (D_a), canopy-to-air humidity mole fraction difference (D_c), air temperature (T_a) and canopy temperature (T_c). Measurements taken over a *Brachiaria* field and a herbaceous savanna in typical days during the dry and wet seasons of the Orinoco lowlands.

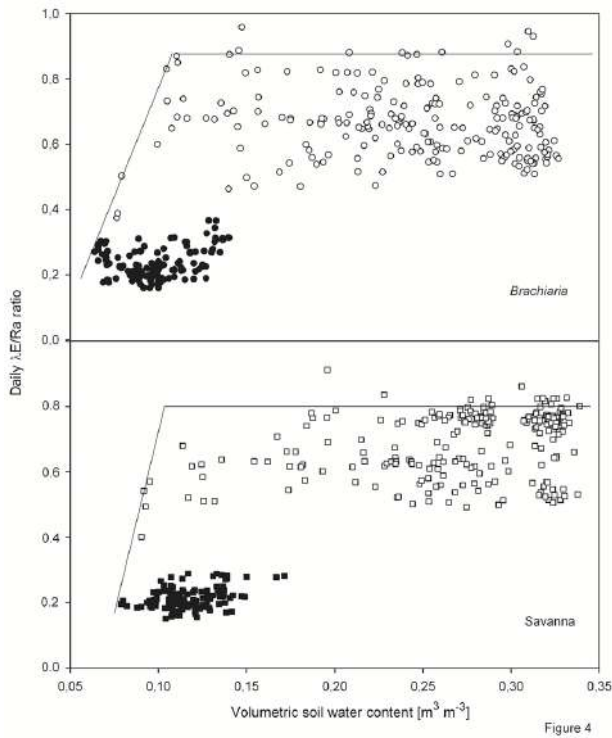


Figure 4. Daily latent heat flux to available energy ratio ($\lambda E/R_a$) as a function of volumetric soil water content (θ) in a *Brachiaria* field (A) and a herbaceous savanna (B) for the dry (●) and wet (○) seasons of the Orinoco lowlands. Maximum daily $\lambda E/R_a$ ratio is represented by using a 99th quantile piece-wise linear regression.

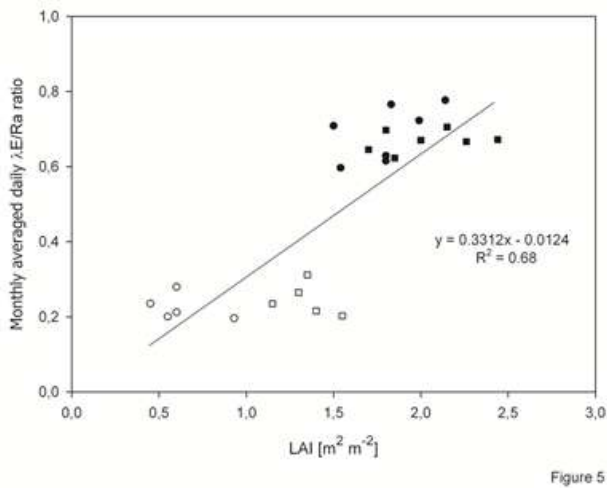


Figure 5. Monthly averaged diurnal latent heat flux to available energy ratio ($\lambda E/R_a$) as a function of leaf area index (LAI) in a *Brachiaria* field (□ dry season; ■ wet season) and a herbaceous savanna (○ dry season; ● wet season) of the Orinoco lowlands.

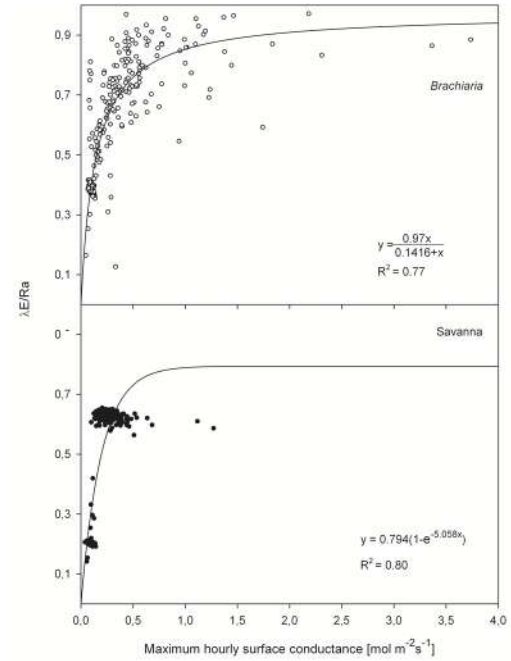


Figure 6. Daily latent heat flux to available energy ratio ($\lambda E/R_a$) as a function of maximum hourly surface conductance (g_s) in a *Brachiaria* field (A) and a herbaceous savanna (B) of the Orinoco lowlands.

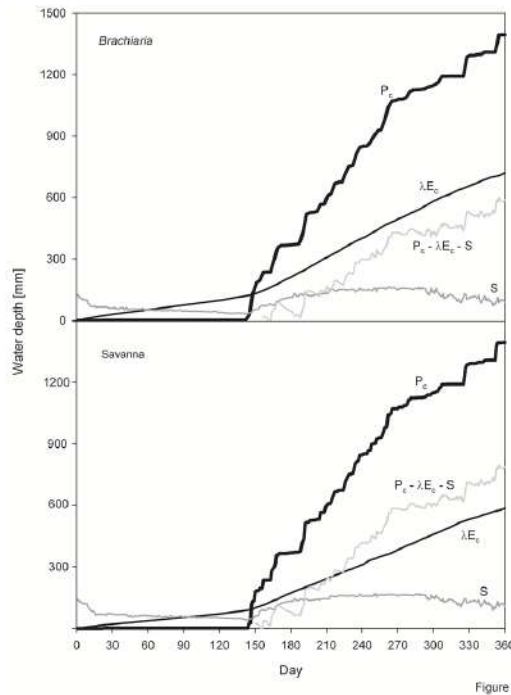


Figure 7. Trend of cumulative precipitation (P_c , thick black), cumulative evapotranspiration (E_c thin black), water storage in the first 0.5 m (S , dark grey) and balance of the previous terms ($P_c - \lambda E_c - S$, light grey) in a *Brachiaria* field (A) and a herbaceous savanna (B) of the Orinoco lowlands.

References

- [1] Grace, J., San Jose, J.J., Meir, P., Miranda, H.S. and Montes, R.A. "Productivity and carbon fluxes of tropical savannas", *J. Biogeogr.*, 2006, 33: 387-400
- [2] Young, M.D. and Solbrig, O.T. "The world's Savannas Economic Driving Forces, Ecological Constraints and Policy Options for Sustainable Land Use". *Man and The Biosphere Series, UNESCO. Vol. 12. The Parthenon Publishing Group, UK, 1993.*
- [3] San José, J.J., Montes, R.A., Grace, J., Nikonova, N. and Osio, A. "Land-use changes alter radiative energy and water vapor fluxes of a tall-grass *Andropogon* field and a savanna-woodland continuum in the Orinoco lowlands", *Tree Physiol.*, 2008, 28: 425-435
- [4] Loch, D.S.. "*Brachiaria decumbens* (signal grass). A review with particular reference to Australia", *Trop. Grasslands*, 1977, 11: 144-157
- [5] Thomas, D. and Grof, B.. "Some pastures species for the tropical savannas of South America". III. *Andropogon gayanus*, *Brachiaria* spp. and *Panicum maximum*. *Herb. Abstr.*, 1986, 56: 557-565
- [6] Humphreys, L.R.. "Tropical Pastures and Fodder Crops", second ed. Longman, New York, 1987.
- [7] CIAT.. "Informe anual del programa de pastos tropicales", (CIAT: Cali, Colombia), 1992.
- [8] Miles, J.W., Maass, B.L., do Valle, C.B. and Kumble, V.. *Brachiaria: Biología, Agronomía y Mejoramiento*, pp. 312 (CIAT-EMBRAPA: Colombia), 1998.
- [9] Pizarro, E.A., do Valle, C.B., Keller-Grein, G., Schultze, R. and Zimmer, A.H.. "Experiencia regional con *Brachiaria*: Región de América Tropical-Sabanas", In: Miles, J.W., Maass, B.L., do Valle, C.B., Kumble V. (Eds.), *Brachiaria: Biología, Agronomía y Mejoramiento*. CIAT-EMBRAPA, Colombia, 1998: 247-269.
- [10] San José, J.J., Nikonova, N. and Bracho, R.. "Comparison of factors affecting water transfer in a cultivated paleotropical grass (*Brachiaria decumbens* Stapt.) field and a neotropical savanna during the dry season of the Orinoco lowlands", *J. Appl. Meteorol.*, 1998, 37: 509-522
- [11] Vera, R.A., Hoyos, P. and Moya, M.C.. "Pasture renovation practices of formers in the Neotropical savannas", *Land Degrad.* 1998, 9: 47-56
- [12] Monteith, J.L. and Unworth, M.M.. "Principles of Environmental Physics", second ed. Edward Arnold, London, 1990.
- [13] Verhoef, A., Allen, S.J., De Bruin, H.A.R., Jacobs, C.M.J. and Heusinkveld, B.G.. "Fluxes of carbon dioxide and water vapour from a Sahelian savanna", *Agri. Forest Meteorol.*, 1996, 80: 231-248.
- [14] Miranda, A.C., Miranda, H.S., Lloyd, J., Grace, J., Francey, R.J., McIntyre, J.A., Meir, P., Riggan, P., Lockwood, R. and Brass, J.. "Fluxes of carbon, water and energy over Brazilian cerrado: an analysis using eddy covariance and stable isotopes", *Plant Cell and Environment*, 1997, 20: 315-328.
- [15] Cook, P.G., Hatton, T., Pidsley, D., Herczeg, A.L., Held, A.A., O'Grady, A.D. and Eamus, D.. "Water balance of a tropical woodland ecosystem, northern Australia: a combination of micro-meteorological, soil physical and groundwater chemical approaches", *J. Hydrol.*, 1998, 210: 161-177
- [16] Eamus, D., Hutley, L.B. and O'Grady, A.P.. "Daily and seasonal patterns of carbon and water fluxes above a northern Australian savanna", *Tree Physiol.*, 2001, 21: 977-988.
- [17] Espinoza, J.. "Estudio de las series de suelo y levantamiento agrologico del campo experimental agrícola de sabana de Jusepin", *Escuela de Ingeniería Agronómica, Núcleo Monagas/Jusepin, Universidad de Oriente*, 1970: 40.
- [18] Soil Survey Staff.. "Soil Taxonomy. A basic system of soil classification for making and interpreting soil survey", *USDA Agriculture Handbook No. 436. US Government Printing Office, Washington*, 1975.
- [19] Fermín, M.A.J.. "Algunas relaciones suelo-agua de la Estación Experimental Agrícola de Sabana", *Trabajo de grado, Universidad de Oriente, Jusepin, Monagas, Venezuela*, 1971.
- [20] McKell, C.M., Wilson, A.M. and Jones, M.B. "A flotation method for easy separation of roots from soil samples", *Agron.*, 1961, 53: 56-57
- [21] Moncrieff, J., Monteny, B., Verhoef, A., Friborg, T., Kabat, P., de Bruin, H., Soegaard, H., Jarvis, P.G. and Taupin, J.D.. "Spatial and temporal variations in net carbon flux during HAPEX-Sahel", *J. Hydrol.*, 1997, 188-189: 563-588.
- [22] Aubinet, M., Grelle, A., Ibrom, A., Rannik, U., Moncrieff, J., Foken, T., Kowalski, A.S., Martin, P.H., Berbigier, P., Bernhofer, C., Clement, R., Elbers, J., Granier, A., Grünwald, T., Morgenstern, K., Pilegaard, K., Rebmann, C., Snijders, W., Valentini, and R., Vesala, T.. "Estimates of the annual net carbon and water exchange of forests: the EUROFLUX methodology", *Adv. Ecol. Res.*, 2000, 30: 113-175.
- [23] Webb, E.K., Pearman, G.I. and Leuning, R.. "Correction of flux measurements for density effects due to heat and water vapour transfer", *Q. J. Roy. Meteor. Soc.*, 1980, 106: 85-100.
- [24] Fuchs, M. and Tanner, C.B.. "Calibration and field test of soil heat flux plates", *Soil Sci. Soc. Am. Pro.*, 1968, 32: 326-328

- [25] Schmid, H.P. and Oke, T.R.. “Estimating the source area of a turbulent flux measurement over a patchy surface”, In: Proceedings of the Conference on Turbulence and Diffusion. American Meteorological Society, San Diego, 1988: 123–126.
- [26] Schuepp, P.H., Leclerc, M.Y., Macpherson, J.I. and Desjardins, R.L.. “Footprint prediction of scalar fluxes from analytical solutions of the diffusion equation”, *Bound-Lay. Meteorol*, 1990, 50: 355–373.
- [27] Richards, L.A.. “Methods of measuring soil moisture tension”, *Soil Sci*, 1949, 68: 95–112.
- [28] Falge, E., Baldocchi, D., Olson, R.J., Anthoni, P., Aubinet, M., Bernhofer, C., Burba, G., Ceulemans, R., Clement, R., Dolman, H., Granier, A., Gross, P., Grünwald, T., Hollinger, D., Jensen, N.O., Katul, G., Keronen, P., Kowalski, A., Ta Lai, C., Law, B.E., Meyers, T., Moncrieff, J., Moors, E., Munger, J.W., Pilegaard, K., Rannik, Ü., Rebmann, C., Suyker, A., Tenhunen, J., Tu, K., Verma, S., Vesala, T., Wilson, K. and Wofsy, S.. “Gap filling strategies for defensible annual sums of net ecosystem exchange”, *Agri. Forest Meteorol*, 2001, 107: 43–69.
- [29] Reichstein, M., Falge, E., Baldocchi, D., Papale, D., Aubinet, M., Berbigier, P., Bernhofer, C., Buchmann, N., Gilmanov, T., Granier, A., Grünwald, T., Havránková, K., Ilvesniemi, H., Janous, D., Knohl, A., Laurila, T., Lohila, A., Loustau, D., Matteucci, G., Meyers, T., Miglietta, F., Ourcival, J.M., Pumpanen, J., Rambal, S., Rotenberg, E., Sanz, M., Tenhunen, J., Seufert, G., Vaccari, F., Vesala, T., Yakir, D. and Valentini, R.. “On the separation of net ecosystem Exchange into assimilation and ecosystem respiration: review and improved algorithm”, *Glob. Change Biol*, 2005, 11: 1424–1439
- [30] Reifsnnyder WE, McNaughton KG. and Milford, J.R.. “Symbols, units, notation. A statement of journal policy”, *Agri. Forest Meteorol*, 1991, 54: 389–397.
- [31] Adams, R.S., Black, T.A. and Fleming, R.L.. “Evaporation and surface conductance in a high elevation, grass-covered forest clear cut”, *Agr. Forest Meteorol*, 1991, 56: 173-193.
- [32] Koenker, R. and Park, B.J.. “An interior point algorithm for nonlinear quantile regression”, *J. Econometrics*, 1994, 71: 265-283.
- [33] Code, B.S. and Noon, B.R.. “A gentle introduction to quantile regression for ecologist” *Front. Ecol. Environ*, 2003, 1: 412-420.
- [34] Thom, A.S.. “Momentum, mass and heat exchange of vegetation”, *Q.J. Roy. Meteor. Soc*, 1972, 98: 124-134.
- [35] Verma, S.B.. “Aerodynamic resistances to transfer of heat, mass and momentum”, in: Black, T.A., Splittelhouse, D.L., Novak, M.D., Price, D.T. (Eds.), *Estimation of Areal Evapotranspiration*. International Association of Hydrological Science, Wallingford, UK, 1989: 13–20
- [36] Paulson, C.A.. “The mathematical representation of wind speed and temperature profiles in the unstable atmospheric surface layer”, *J. Appl. Meteorol*, 1970, 9: 857–861.
- [37] Garratt, J.R. and Hicks, B.B.. “Momentum, heat and water vapour transfer to and from natural and artificial surfaces”, *Q. J. Roy. Meteor. Soc*, 1973, 99: 680-687.
- [38] Kelliher, F.M., Leuning, R. and Schulze, E.D.. “Evaporation and canopy characteristics of coniferous forest and grasslands”, *Oecology*, 1993, 95: 153-163.
- [39] Kelliher, F.M., Leuning, R., Raupach, M.R. and Schulze, E.D.. “Maximum conductances for evaporation from global vegetation types”, *Agri. Forest Meteorol*, 1995, 73: 1-16.
- [40] McNaughton, K.G. and Jarvis, P.G.. “Predicting the effects of vegetation changes on transpiration and evaporation”. In: Kozlowski, T.T. (Ed.), *Water Deficits and Plant Growth*, Vol VII. Academic Press. New York, 1983: 1–47.
- [41] Jarvis, P.G. and McNaughton, K.G.. “Stomatal control of transpiration: scaling up from leaf to region”, *Adv. Ecol. Res*, 1986, 15: 1-49.
- [42] Stewart, J.B.. “Modelling surface conductance of pine forest”, *Agri. Forest Meteorol*, 1988, 43: 19–35
- [43] Gash, J.H.C., Wallace, J.S., Lloyd, C.R., Dolman, A.J., Sivakumar, M.V.K. and Renard, C.. “Measurements of evaporation from fallow Sahelian savannah at the start of the dry season”, *Q. J. Roy. Meteor. Soc*, 1991, 117: 745-760
- [44] Montgomery, D.C. and Peck, E.A.. “Introduction to Linear Regression Analysis”, John Wiley and Sons, New York, 1982.
- [45] Chow, V.T. and Kariotis S.J.. “Analysis of stochastic hydrologic systems”, *Water Resour. Res*, 1970, 6: 1569-1582.
- [46] Sokal, R.R. and Rohlf, F.J.. “Biometry: the principles and practice of statistics” in biological research. Fourth ed. W.H. Freeman and Co. New York, 1995.
- [47] Meek, D.W. and Prueger, J.H.. “Solutions for three regression problems commonly found in meteorological data analysis”, In: *Proceeding of the 23rd Conference on Agricultural Forest Meteorology*. 1998: 141-145. (American Meteorological Society: Albuquerque)
- [48] Denmead, D.T. and Shaw, R.J.. “Availability of soil water to plants as affected by soil moisture content and meteorological conditions”, *Agron. J*, 1962, 54:

- 385-390.
- [49] Keenan, T., Rutledge, S., Carbone, R., Wilson, J., Takanashi, T., May, P., Tapper, N.J., Platt, M., Hacker, J., Skelsky, S., Moncrieff, M.W., Saito, K., Holland, G.J., Crook, A. and Cage, K.. “The marine continent thunderstorm experiment (MCTEX): overview and some results”, *B. Am. Meteorol. Soc.*, 2000, 81: 2433-2455.
- [50] Xinmei, H., Lyons, T.J. and Smith, C.G.. “Meteorological impact of replacing native perennial vegetation with annual agricultural species”, *Hydrological Processes*, 1995, 9: 645-654.
- [51] Beringer, J., Hutley, L.B., Tapper, N.J., Coutts, A., Kerley, A and, O’Grady, A.P.. “Fire impacts on surface heat, moisture and carbon fluxes from a tropical savanna in north Australia”, *Inter. J. Wildland Fire*, 2003, 12: 333-340.
- [52] Maitelli, G.T. and Miranda, A.C.. “Evapotranspiração e fluxos de energia no cerrado - estação chuvosa”, *An. Acad. Bras. Cienc.*, 1991, 63: 265-272.
- [53] Miranda, A.C., Miranda, H.S., Lloyd, J., Grace, J., McIntyre, J.A., Meir, P., Riggan, P., Lockwood, R. and Brass, J.. “Carbon Dioxide Fluxes over a Cerrado sensu stricto in Central Brazil”, In: Gash, J.H.C., Nobre, C.A., Roberts, J.M., Victoria, R. (Eds.), *In Amazonia Deforestation and Climate*. John Wiley & Sons, Chichester, 1996: 353-363.
- [54] Santos, A.J., Silva, G.T., Miranda, H.S., Miranda, C. and Lloyd, J.. “Effects of fire on surface carbon, energy and water vapour fluxes over campo sujo savanna in Central Brazil”, *Funct. Ecol.*, 2003, 17: 711-719.
- [55] Oliveira, R.S., Bezerra, L., Davidson, E.A., Pinto, F., Klink, C.A., Nepstad, D.C. and Moreira, A.. “Deep root function in soil water dynamics in cerrado savannas of Central Brazil”. *Funct. Ecol.*, 2005, 19: 574-581.
- [56] Giambelluca, T.W., Scholz, F.G., Bucci, S.J., Meinzer, F.C., Goldstein, G., Hoffmann, W.A., Franco, A.C. and Buchert, M.P.. “Evapotranspiration and energy balance of Brazilian savannas with contrasting tree density”, *Agri. Forest Meteorol.*, 2009, 149: 1365-1376.
- [57] Santos, A.J., Quesada, C.A., da Silva, G.T., Maia, J.F., Miranda, H.S., Miranda, A. and Lloyd, L.. “High rates of net ecosystem carbon assimilation by *Brachiaria* pasture in the Brazilian cerrado”, *Glob. Change Biol.*, 2004, 10: 877-885.
- [58] Hutley, L., O’Grady, A. and Eamus, D.. “Evapotranspiration from Eucalypt open-forest savanna of Northern Australia”, *Funct. Ecol.*, 2000, 14: 183-194.
- [59] Bucci, S.J., Scholz, F.G., Goldstein, G., Hoffman, W.A., Meinzer, F.C. Franco, A.C., Giambelluca, T. and Miralles-Wilhelm F.. “Controls on stand transpiration and soil water utilization along a tree density gradient in a Neotropical savanna”, *Agri. Forest Meteorol.*, 2008, 148: 839-849.
- [60] Baldocchi, D.D., Xu, L. and Kiang, N.Y.. “How plant functional-type, weather, seasonal drought, and soil physical properties alter water and energy fluxes of an oak-grass savanna and an annual grassland”, *Agri. Forest Meteorol.*, 2004, 123: 13-39.
- [61] Lewis, D.C.. “Annual hydrologic response to watershed conversion from oak woodland to annual grassland”, *Water Resour. Res.*, 1968, 4: 59-72.
- [62] Ramier, D., Boulan, N., Cappelaere, B., Timouk, F., Rabanit, M., Lloyd, C.R., Boubkraoui, S., Metayer, F., Descroix, L. and Wawrzyniak, V.. “Toward an understanding of coupled physical and biological processes in the cultivated Sahel. 1. Energy and water”, *J. Hydrol.*, 2009, 375: 204-216.
- [63] Mattos, J.L., Gomide, J.A., Martinez, J. and Huaman, C.A.. “Crescimento de espécies do gênero *Brachiaria*, sob déficit hídrico, em casa de vegetação”, *Rev. Bras. Zootecn.*, 2005, 34: 746-754.
- [64] Bittman, S. and Simpson, G.M.. “Drought effects on water relations of three cultivated grasses”, *Crop Sci.*, 1989, 29: 992-999.
- [65] Bagayoko, F., Yonkeu, S., Elbers, J. and Van de Griesse, N.. “Energy partitioning over the West African savanna: Multi-year evaporation and surface conductance measurements in Eastern Burkina Faso”, *J. Hydrol.*, 2007, 334: 545-559.
- [66] Fonseca, A.S.. “Identificación de los cuerpos silíceos de las gramíneas de la sabana de *Trachypogon* de los llanos Altos Centrales”, *Bol. Soc. Venez. Ci. Nat.*, 1983, 141: 17-83.
- [67] Baruch, Z., Ludlow, M.M. and Davis, R.. “Photosynthetic responses of native and introduced C₄ grasses from Venezuelan savannas”, *Oecologia*, 1985, 67: 288-293.
- [68] Eamus, D. and Cole, S.. “Diurnal and seasonal comparisons of assimilation, phyllode conductance and water potential, of three *Acacia* and one *Eucalyptus* species in the wet-dry tropics of Australia”, *Aust. J. Bot.*, 1997, 45: 275-290.
- [69] Prior, L.D., Eamus, D. and Duff, G.. “Seasonal and diurnal patterns of carbon assimilation, stomatal conductance and leaf water potential” in *Eucalyptus tetradonta* saplings in a wet-dry savanna in northern Australia, *Aust. J. Bot.*, 1997, 45: 241-258.
- [70] Eamus, D., Myers, B., Duff, G. and Williams, D.. “Seasonal changes in photosynthesis of eight savanna tree species”, *Tree Physiol.*, 1999, 19: 665-671.

- [71] Whitley, R., Taylor, D., Macinnis-Ng, C., Zeppel, M., Yunusa, I., O'Grady, A., Froend, R., Medlyn, B. and Eamus, D.. "Developing an empirical model of canopy water flux describing the common response of transpiration to solar radiation and VPD across five contrasting woodlands and forests", *Hydrol. Process*, 2012.
DOI: 10.1002/hyp.9280
- [72] San José, J.J., Montes, R.. "Management effects on stocks and fluxes across the Orinoco savannas", *Forest Ecol. Manag.*, 2001, 150: 293-311.
- [73] Sellers, P.J., Randall, D.A., Collatz, G.J., Berry, J.A., Field, C.B., Dazlich, D.A., Zhang, C., Collelo, G.D. and Bounoua, L.. "A revised land surface parameterization (SiB2) for atmospheric GCMs. Part I: Model formulation", *J. Climate*, 1996, 9: 676–705.
- [74] Ham, J.M. and Knapp, A.K.. "Fluxes of CO₂, water vapour, and energy from a prairie ecosystem during the seasonal transition from carbon sink to carbon source", *Agri. Forest Meteorol.*, 1998, 89: 1-14.
- [75] Zeng, N. and Neelin, J.D.. "The role of vegetation-climate interaction and interannual variability in shaping the African savanna", *J. Climate*, 2000, 13: 2665–2669.
- [76] Schaeffer, M., Eickhout, B., Hoog Wijk, M., Strengers, B., van Vuuren, D., Leemans, R. and Opteegh, T.. "CO₂ and albedo climate impacts of extratropical carbon and biomass plantations", *Glob. Biogeochem. Cy.* 20, GB2020, 2006.
DOI: 10.1029/2005GB002581
- [77] Joffre, R. and Rambal, S.. "How tree cover influences the water balance of Mediterranean rangelands", *Ecology*, 1993, 74: 570-582.
- [78] Hoffmann, W.A. and Jackson, R.B.. "Vegetation-climate feedbacks in the conversion of tropical savanna to grassland", *J. Climate*, 2000, 13: 1593-1602.



ARTICLE

Climatology of Winter Extratropical Cyclones over the Coastal Waters of China

Naru Xie^{1,2} Meng Gao^{1*} Zhiqiang Gao¹

1. Key Laboratory of Coastal Zone Environmental Processes and Ecological Remediation, Yantai Institute of Coastal Zone Research, Chinese Academy of Sciences, Yantai 264003, China
2. University of Chinese Academy of Sciences, Beijing 100049, China

ARTICLE INFO

Article history

Received: 7 March 2019

Accepted: 28 March 2019

Published Online: 12 April 2019

Keywords:

Extratropical cyclones
Atmospheric circulation
Cluster analysis
Precipitation

ABSTRACT

The East China coast is one major cyclogenesis region of extratropical cyclones (ETCs) in boreal winter. In this study, the climatological characteristics of winter ETCs passing over the coastal water of China are analyzed by using clustering and composite analysis. Automated cyclone detection and tracking algorithm are used to identify the ETCs, which are further classified into subgroups according to their trajectory features by using the probabilistic clustering algorithm. Six distinct types of straight moving or recurving trajectories with different climatological characteristics are identified in the clustering analysis. Accordingly, the composite analyses also present six distinct synoptic patterns corresponding to cyclogenesis as well as the impact of ETCs on terrestrial precipitation. The spatio-temporal characteristics of winter ETCs' origination, movement, and impact are revealed by the clustering and composite analyses.

1. Introduction

Extratropical cyclone (ETC), also called wave cyclone or midlatitude cyclone, is a type of storm system in middle or high latitudes that transports huge amounts of moisture and energy poleward to reduce the meridional temperature gradient^[1-2]. The passage of ETC is usually associated with strong winds, excessive precipitation, and temperature changes^[3-5]. Therefore, studying the characteristics and paths of ETCs are of great importance both in terms of understanding variations of local weather and for a characterization of climate^[3].

There have been a lot of studies on ETCs including

their life cycle from initiation, growing, to their impacts as well as the identification, tracking, and clustering algorithms^[3-10]. The formation and evolution mechanisms of ETCs have been extensively studied using a wide range of observational, theoretical, and modeling approaches (reviewed in^[4]). The main focus of this study start from the identification and tracking of winter ETCs to their climatological characteristics and impacts.

In the early times, the identification and tracking of cyclones were based on manual analysis of synoptic weather charts^[11, 12]. Such analysis was very time-consuming, and could only be applied to a limited number of maps. With the increase of computer capacity in recent decades, new automatic and semi-automatic meth-

*Corresponding Author:

Meng Gao,

Key Laboratory of Coastal Zone Environmental Processes and Ecological Remediation, Yantai Institute of Coastal Zone Research, Chinese Academy of Sciences, Yantai 264003, China;

Email: mgao@yic.ac.cn

ods are developed to objectively detect ETCs based on sea level pressure, geopotential height, or vorticity fields^[13-17]. The tracked ETCs are usually described as a set of moving objects that follow various tracks and have distinct individual lifecycle characteristics. Cluster analysis provides a natural way to analyze sets of trajectories and their relationships with the larger-scale atmospheric circulation, by decomposing large sets of trajectories into subgroups with similar spatio-temporal characteristics^[18,19]. Then, the synoptic characteristics of the clustered ETCs could be easily revealed by the following composite analysis^[20,21].

East Asia, especially the East China coast, is a major cyclogenesis region in the Northern Hemisphere^[22,23]. These ETCs move mainly eastward over the coastal waters of China and Northern Pacific^[22]. A few of recent studies have focused on the climatological characteristics of ETCs, particularly those generated at East China coast. Objective identification and tracking methods were widely used to study the features of ETCs in spring^[24-26]. ETCs over East Asia and Western Pacific exhibit obvious seasonal variability, and stronger ETCs more frequently occurred in winter and spring than in summer and autumn^[9]. Qin et al.^[25] found that China's offshore ETC tracks tend to shift northward in recent decades, characterized by increased (decreased) cyclone number at the northern (southern) part of the East China Sea. Zhang et al.^[26] applied the k-means clustering method to identify the dominating trajectories of ETCs over East Asia, and studied their climatological characteristics in the period 1958-2001. Due to the spatio-temporal homogeneity of ETCs, the k-means clustering method was not the proper algorithm for clustering ETC trajectories^[18]. Zhang et al.^[23] proposed to classify the developing of ETCs into two types according to the central pressure deepening rate, and studied the inter-annual variability of ETC number and the possible causes.

This study firstly applies an improved winter ETC detection and tracking algorithm based on vorticity fields to identify the ETCs over the coastal waters of China. Then, the probabilistic clustering method is used to classify the ETCs according to their trajectory features. The climatological characteristics as well as the larger-scale atmospheric circulations are also analyzed by using the composite analysis. Moreover, the impacts of ETCs on terrestrial precipitation are also studied. The study is organized as follows: Section 2 presents the data and methodology used in this study. The ETC identification, tracking, and classification along with the composite daily means and anomalies of the synoptic pattern, are presented as results in Section 3. Finally the discussion

and conclusions are given in Section 4 and Section 5, respectively.

2. Data and Methods

2.1 Data

This study adopts the European Centre for Medium range Weather Forecasts (ECMWF) re-analysis data (ERA-Interim for 1979–2017), with a $0.75^{\circ} \times 0.75^{\circ}$ horizontal resolution and 6-h time interval^[27]. The vorticity fields at 850 hPa level within the region of 20° – 60° N, 60° – 160° E extracted from the ERA-I reanalysis dataset are used for ETC identification and tracking. Other synoptic variables related to large scale atmospheric circulations are 500hPa zonal and meridional wind, geopotential height, air temperature at 850 hPa level, and mean sea level pressure. The daily anomaly fields of all synoptic variables are calculated by subtracting the seasonal cycles (calendar-day mean) for each grid cell. The seasonal cycle is defined from 1979 to 2017, and a 5-day running average is applied to reduce day to day variation.

The daily total precipitation data on a $0.5^{\circ} \times 0.5^{\circ}$ grid within the study area EAME are provided by the National Oceanic and Atmospheric Administration Climate Prediction Center (U.S.A.). The daily mean climatology for precipitation has been firstly calculated for each grid during the period 1979-2017, and a 5-day running average is also applied for the purpose of reducing the day to day variation. Then, the smoothed mean precipitation is divided by the daily precipitation, and the ratio represents the precipitation anomaly^[28].

2.2 Methods

In this study, the objective algorithm presented in^[17] is used to identify and track winter ETCs (Dec., Jan., and Feb.) based on the vorticity fields at 850 hPa level. The algorithm includes two independent steps, where the first step is devoted to the identification of the cyclone centers, which are combined into a track in the second step. A Matlab toolbox named CycloTRACK (v1.0) could be accessed from the corresponding author of reference^[17]. The spurious paths of cyclones moving upstream/westward over five longitude degrees or having a lifetime less than 24 h are eliminated for the purpose of getting rid of local warm season thermal lows^[29] and some tropical cyclones moving westward from Northern Pacific^[30]. Moreover, only ETCs originating or entering the regions 35 – 41° N, 117 – 127° E and 25 – 35° N, 120 – 130° E are considered in this study. Besides the latitude and longitude of cyclone centers, the lifetime, central sea

level pressure, and travel distances of all ETCs are also recorded. The normalized central pressure deepening rate is also computed using the following equation^[31]:

$$R = (P_{t-12} - P_{t+12}) / 24hPa \times [(\sin 60^\circ) / \sin \phi], \quad (1)$$

where P_{t-12} and P_{t+12} are the central pressures of the cyclone before 12h and 12h after current time, respectively; the parameter ϕ denotes the latitude of the cyclone center. The unit of R is “bergeron” (referred to as B). A positive value of R corresponds to developing cyclone, and more specifically the cyclone with R exceeding 1 B is considered as an explosive cyclone^[23, 25, 26, 31].

Like Gaffney et al.^[18], the probabilistic clustering algorithm is used to classify the identified winter ETCs. In this algorithm, a regression mixture model is applied to describe the longitude-time and latitude-time propagation of the ETCs. Each ETC track is assumed to be generated by one of K different regression models. The clustering problem is actually to assign each track to the mixture component (and thus the cluster) that is most likely to have generated that track. Sometimes, the latitude and longitude measurements are normalized before clustering. In this study, we omit the preprocessing step such as the normalization of ETC tracks. Instead, the ETC tracks are clustered directly, so that the produced results become easy to interpret^[20]. The optimum number of clusters is determined by balancing inter-cluster and within cluster variability. The log-likelihood values are also computed as the goodness-of-fit metric^[18]. The procedure for model selection is as follows: we randomly select the training sets of trajectories, and then compute the log-probability of unseen “test” trajectories under each model. This calculation has been repeated ten times over multiple training-test partitions of the data to generate average out-of-sample log-probability (or log-likelihood) scores as the basis of model selection. Here, we only give a simple summary of the clustering algorithm, and detailed description can be found in references^[18, 20] with an application of the clustering method to ETCs over the North Atlantic. A Matlab toolbox of the above-mentioned clustering algorithm for trajectory clustering is available online at <http://www.datalab.uci.edu/resources/CCT>

3. Results

3.1 Climatological Characteristics of Winter ETCs

The study identified 291 winter ETCs passing over the coastal water of China in the period 1979-2017, and 171 of them are explosive cyclones. All winter ETCs includ-

ing the tracks and the genesis locations are shown in Figure 1. The cyclogenesis location ranges from Mongolia to southeast coast of China. More specifically, these winter ETCs passing over the coastal water of China more frequently originate from the east coast of China. In addition, Figure 2 below shows the time series of ETC and explosive ETC numbers in winter seasons. There is obvious inter-annual variation of the number of ETC or explosive ETC. During the period 1979-2017, the average number of ETCs passing over the coastal water of China is 7.5, and 4.3 of them are explosive ones. No significant temporal trend has been detected for either ETC or explosive ETC time series.

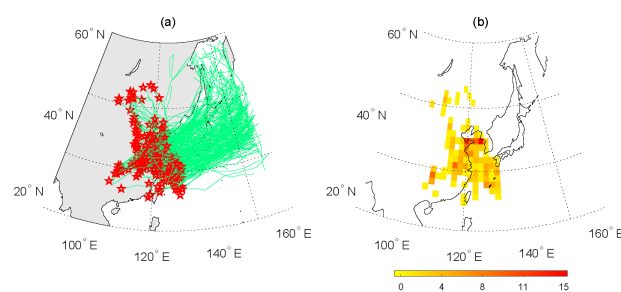


Figure 1. (a) Tracks and cyclogenesis positions of winter ETCs passing over the coastal water of China identified from the European Centre for Medium range Weather Forecasts (ECMWF) re-analysis data (1979–2017); (b) Spatial distribution of cyclogenesis positions in $1.5^\circ\text{lat} \times 1.75^\circ\text{lon}$ rectangle

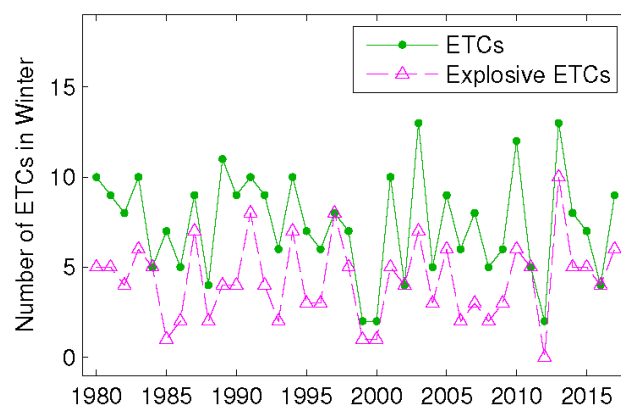


Figure 2. Annual time series of winter ETC number and explosive ETC number

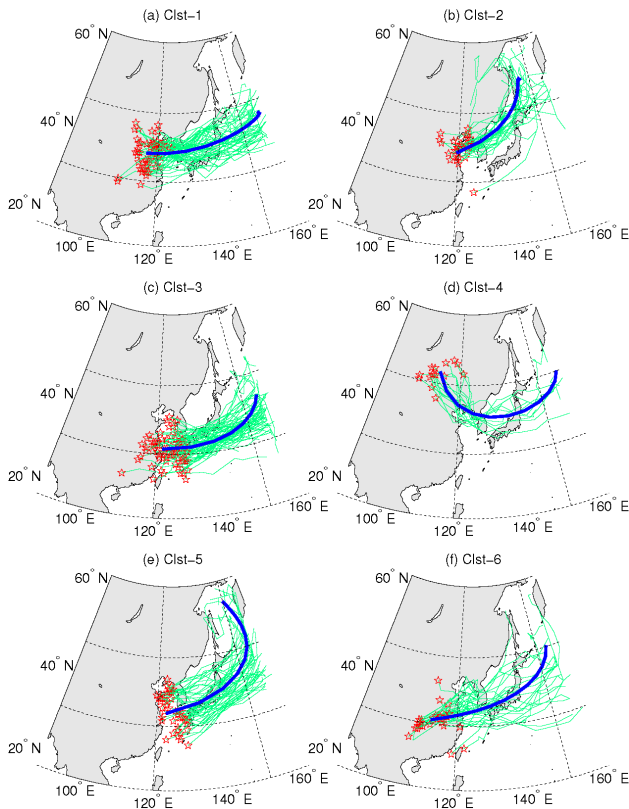


Figure 3. The classified Winter ETCs tracks (green) passing over the coastal water of China during the period 1979–2017 and the mean regression curve (blue curves) in each of the six clusters

In this study, a quadratic polynomial in the probabilistic clustering algorithm has been selected for the ETC tracks by visually inspecting the ETC shape (not shown as figures). The candidate cluster numbers from 4 to 9 have been evaluated, and we find that the clustering results are not sensitive to the choices between 6 and 8. The final choice of cluster number is 6 since the trajectory shapes and cyclogenesis positions could be easily distinguished. Figure 3 shows the clustered ETC tracks as well as the mean regression trajectories. The ETC tracks in cluster-1 are typical straight and usually cross Korean Peninsula and Japan. The cyclogenesis positions for ETCs in cluster-2 are similar to those in cluster-1. However, the ETCs in cluster -2 usually move northeastward rather than eastward in cluster-1. ETCs firstly cross the Korean Peninsula, then move to the Japan Sea, and decay over the Okhotsk Sea. The typical ETC tracks in cluster-3 are very similar to those in cluster-1, but the mean curve is localized farther to the south and crossing the south border of Japan. The typical tracks in clusters 4 and 5 are both recurved trajectories. ETCs in cluster-4 originate at Mongolia and move southeastward firstly, then recurve after entering China’s coastal water and move eastward similar to ETCs

in cluster-1. The recurring cluster-5 is more diffuse since the genesis positions occupy almost the whole east coast-al waters including the Bohai Sea, Yellow Sea, and East China Sea. A few of ETCs in this cluster change their directions after entering the Northwest Pacific. The last cluster-6, also the most diffuse cluster, represents ETCs those originate at the Asian continent and move eastward to the Pacific Ocean. Figure 4 below shows all explosive ETCs for each cluster. Most explosive ETCs in winter occur at the Pacific coast or Northwest Pacific. The ratios of explosive ETCs to all ETCs in the 6 clusters are 54%, 69%, 52%, 47%, 92%, and 32%, respectively.

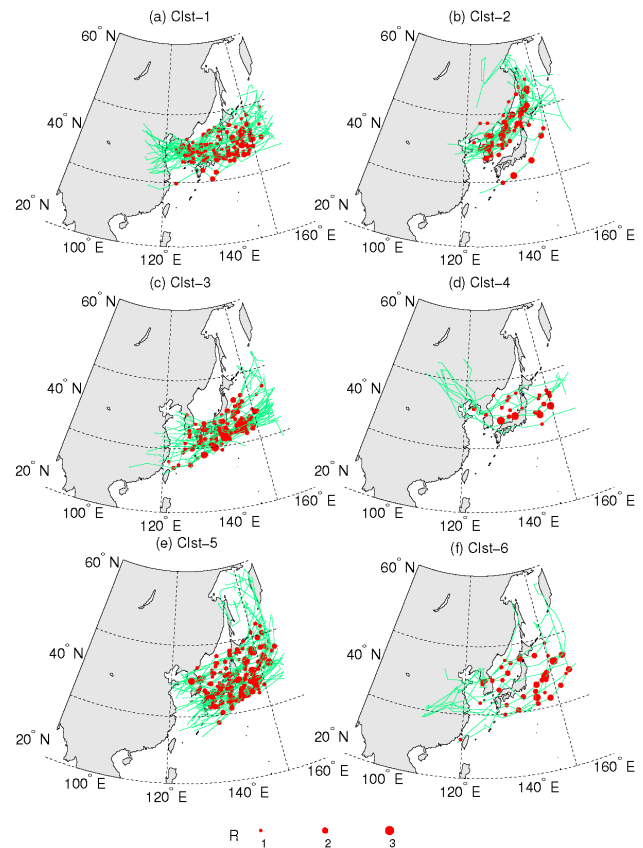


Figure 4. The explosive ETCs in each of the six clusters. The red dots indicate the positions with $R \geq 1$

The distributions of the ETC’s lifetime, track length, minimum central SLP, and maximum deepening rate for each cluster as well as their pairwise correlations are shown in Figure 5. The smoothed probability density functions (PDFs) shown in the diagonal subplots represent the distributions of the 4 climatological characteristics. Except the lifetime and track length in cluster 3 and 5, the other distributions are dissimilar and some PDFs are bio-modal or multi-modal. The lower triangular subplots are the scatterplots, while the upper triangular subplots show the corresponding pairwise spearman correlations for the 6 clusters. Unsurprisingly, the positive correlations

between the lifetime and track length are consistent in all 6 clusters. Significant negative correlations for lifetime vs. minimum central SLP, track length vs. minimum central SLP, and minimum central SLP vs. maximum deepening rate are also identified in all 6 clusters. The maximum deepening rate is also positively correlated to lifetime and track length in 5 clusters except for in cluster-2.

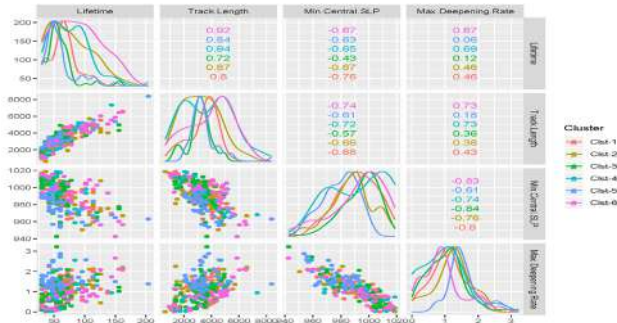


Figure 5. The distributions of the ETC’s lifetime, track length, minimum central SLP, and maximum deepening rate for each cluster as well as their pairwise correlations.

Diagonal subplots: probability distributions of the 4 climatological characteristics; lower triangular subplots: pairwise scatterplots; upper triangular subplots: pairwise spearman correlations for the 6 clusters

3.2. Synoptic Patterns of Winter ETCs

In this study, the synoptic patterns associated with each cluster are obtained by constructing the composite maps of atmospheric variables. For each composite map, the time steps that correspond to either the cyclogenesis position or the whole life cycle are composited. Figures 6-8 show the composite anomalies of geopotential height (500hPa level), air temperature (500hPa level), and mean SLP corresponding to the cyclogenesis days, respectively. Obviously, the cyclogenesis positions for each cluster shown in Figure 3 are consistent with the negative anomalies of geopotential height and low pressure shown in Figure 6 and 7. Moreover, the cyclogenesis positions are also consistent with the cold fronts shown in Figure 8. Since the movement of cyclone is largely determined by the large scale steering winds at mid-tropospheric level (700hPa or 500hPa). The anomalous winds composites at 500hPa during the whole life cycle of ETCs in each cluster are shown in Figure 9. The influence of the steering winds on the mean regression trajectory in each cluster is clearly revealed by the composite wind fields.

The influences of ETCs on terrestrial precipitation are also revealed by the composite maps of anomalous terrestrial precipitation during the whole life cycle of ETCs (Figure 10) in each cluster. Generally, the excessive

precipitation anomalies are consistent with cyclogenesis positions or tracks. In cluster-1, the region with excessive precipitation is located at the rim of the Bohai Sea and Yellow Sea including the Korean Peninsula. However, no excessive precipitation is brought to Japan. In cluster-2, ETCs cause excessive precipitation to Korean Peninsula when moving northeastward. The influence of ETCs in cluster-3 on terrestrial precipitation is over the East China, Korean Peninsula, and South Japan. ETCs in cluster-4 originate at Mongolia and move southeastward to North China associated with excessive terrestrial precipitation anomalies. ETCs in cluster-5 mainly originate over the whole east coastal waters of China, so the influence of ETCs on precipitation anomalies is only located at the Korean Peninsula and the three southern islands of Japan. On the contrary, ETCs in cluster-6 mainly originate at the Central China and move eastward, so that the influence of ETCs on terrestrial precipitation is located at East China.

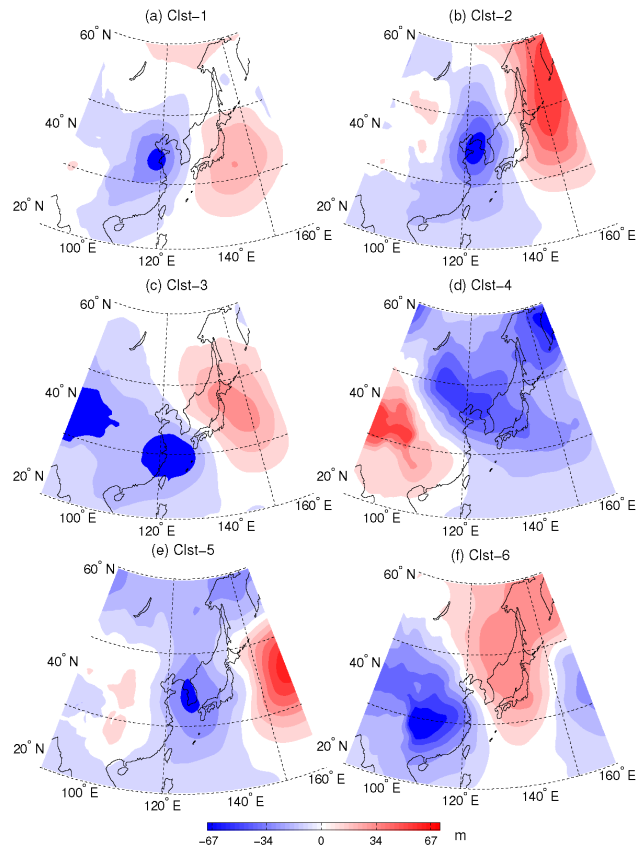


Figure 6. Composite of geopotential height anomalies (red and blue shading) at 500hPa level for each cluster in the period 1979-2017, based on genesis day only

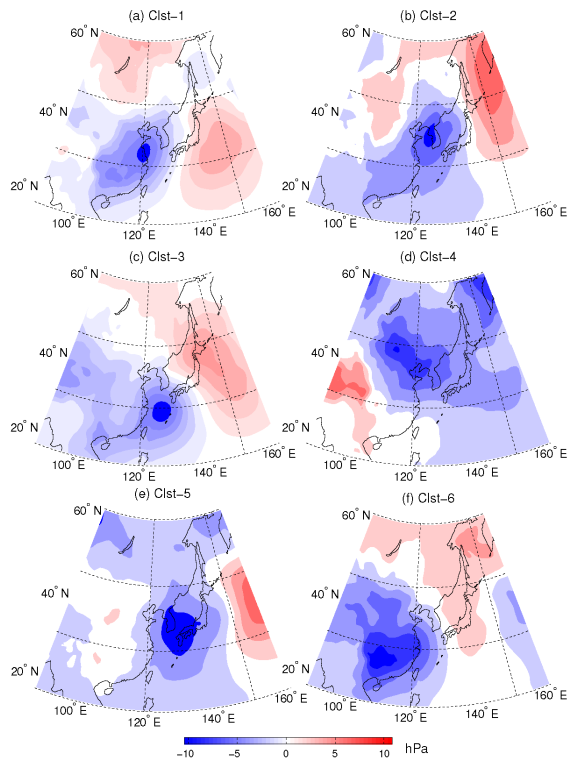


Figure 7. Composite of mean sea level pressure anomalies (red and blue shading) for each cluster in the period 1979-2017, based on genesis day only

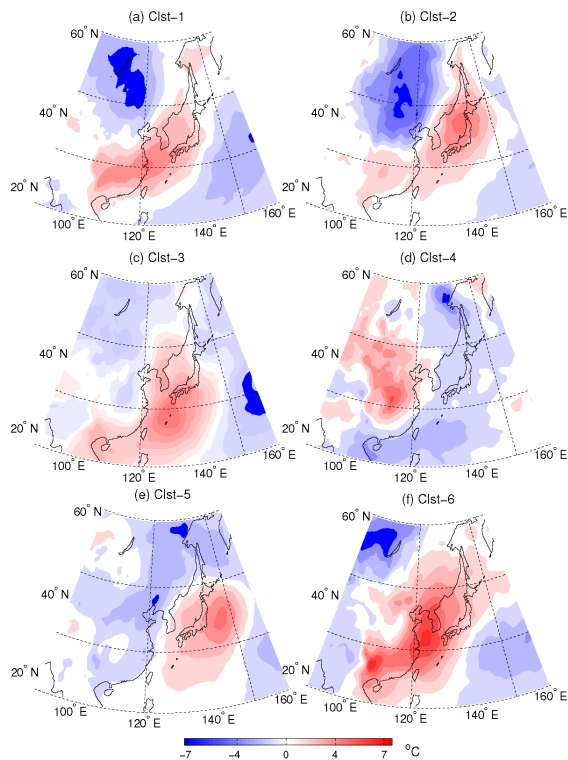


Figure 8. Composite of air temperature anomalies (red and blue shading) at 500hPa level for each cluster in the period 1979-2017, based on genesis day only

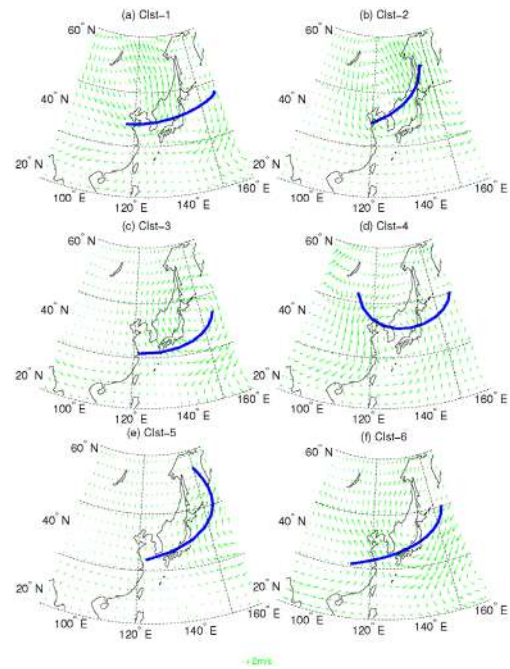


Figure 9. Composite of anomalous wind fields (green vectors) at 500hPa level during the whole life cycle of ETCs in each cluster for the period 1979-2017 and the mean regression curve (blue curves)

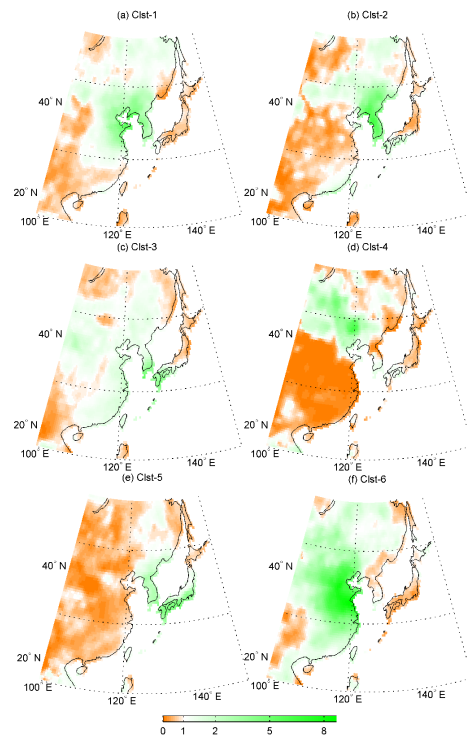


Figure 10. Composite of anomalous terrestrial precipitation (orange and green shading) during the whole life cycle of ETCs in each cluster for the period 1979-2017. The value of ratio smaller than one means precipitation is lower than normal years, while the value of ratio larger than one means precipitation is higher than normal years

4. Discussion

The East coast of China is a vital cyclogenesis region in East Asia^[22]. The climatological characteristics of ETCs passing over the coastal water of China in winter season and their impacts of terrestrial precipitation were the major objective of this study. Previous studies show that ETCs occur in the strong baroclinic zones and thermal advection often trigger the initial development of ETCs^[2-9]. The ETCs developing at the East China coast might be attributable to the atmospheric baroclinicity from continent to ocean.

In this study, the ETC centers were defined in terms of relative vorticity and the tracks are obtained by combining the cyclone centers. The advantage and disadvantage of the use of relative vorticity for cyclone identification and tracking have been discussed in numerous studies^[10, 17, 32, 33]. Vorticity allows for more accurate identification of the cyclone generation at stages earlier than those revealed by SLP. However, the relative vorticity is sensitive to the horizontal resolution of the data set since it is a wind-based field. The algorithm for ETC identification and tracking in this study was presented in reference^[17], where all potential disadvantages have been properly considered and corrected. Zhang et al.^[26] showed that there were two major cyclogenesis regions for winter ETCs in East Asia. In this study, our results are basically consistent with the previous findings. ETCs passing over China's coastal water mainly originate at the East coast of China. Other ETCs are from Mongolia and moving southeastward to the Bohai Sea and Yellow Sea. There was no significant temporal trend for the annual time series of ETC number or explosive ETC number, although there were evidence for the change of ETC frequencies and characteristics over the world^[3]. Wang et al.^[8] found that there was no trend over Northern Europe in the winter. Actually, the changes of ETCs were very complex including the interannual variability of ETC number and the spatial shift of ETC tracks. The changes of ETC frequencies and characteristics for a larger region, i.e. the East Asia or North Hemisphere, deserve a deeper study to a better understanding of the impacts of global climate change on cyclone activities.

ETCs have localized coherent spatial structures that generally propagate toward the east driven by the westerly^[34]. The ETC population is thus most naturally described as a set of moving objects that follow various tracks and have differing individual lifecycle characteristics^[18]. However, the commonly used method in atmospheric sciences such as the principal component analysis (PCA) is not suitable to analyze the cyclone trajectories, which are inherently localized in space in any given timeframe

^[18]. On the contrary, cluster analysis provides a natural way to analyze sets of ETC tracks and their relationships with the larger-scale atmospheric circulations, by classifying cyclone tracks into subgroups with homogeneous spatio-temporal characteristics^[18,19]. Several studies have applied clustering to classify cyclone tracks including tropical cyclones and ETCs. A proper classification of ETCs is helpful to reduce case-to-case variability and allows for a highly realistic representation of specific cyclone features in composite analysis. The roles of atmospheric baroclinicity and thermal advection in triggering the development of ETCs were confirmed by the composite maps for each cluster. Previous studies also verified the passive role of sea surface temperature (SST) gradient in triggering the ETCs originating over the Gulf Stream^[33]. Over China's coastal water, the influence of SST anomalies on ETC activities was verified in^[9, 10, 22]. The role of SST anomalies especially the Kuroshio extension on ETC activities were not covered in this study. Much more detailed and in-depth work should be done in the future. In addition, the composite analysis also showed that anomalous wind fields at mid-tropospheric level partly explained the shapes of mean regression trajectory. An interesting finding of this study was that ETCs did not always cause excessive terrestrial precipitation during their whole lifespan. This question will be answered by a simultaneous analysis of ETC movement and vapor transportation in the next work.

5. Conclusions

In this study, the climatological characteristics of winter ETCs over the coastal water of China are analyzed by using clustering analysis and composite analysis. Using an objective cyclone detection and tracking algorithm, 291 ETCs have been identified from the ERA-I reanalysis dataset (1979-2017) in the study area. The ETCs are classified into 6 clusters according to their trajectory features by using the probabilistic clustering method. The synoptic patterns as well as the impact of ETC on terrestrial precipitation are presented by the composite maps. Major conclusions are summarized as follows.

The cyclogenesis positions of winter ETCs passing over the coastal water of China range from Mongolia to southeast coast of China. Most ETCs are usually weak over the coastal waters but deepening after entering the Pacific coast or Northwest Pacific. No significant temporal trend has been detected in the annual time series of ETC number. There are obvious differences for the features of ETCs in the 6 clusters. Generally, the ETC lifetime is positively correlated to track length and maximum deepening rate, but negatively correlated to minimum central

SLP (Figure 5). The composite analyses show that the cyclogenesis positions are consistent with the strong baroclinic zones and cold fronts. The large scale steering winds at mid-tropospheric level partly determine the ETC movement. The composite analysis also reveals the tight association between ETCs and excessive precipitation. In summary, the clustering of ETCs is basically successful since ETCs with similar spatio-temporal characteristics have been classified into one cluster.

Author Contributions

Conceptualization, M.G.; methodology, M.G. and N.X.; software, M.G. and N.X.; validation, M.G., N.X. and Z.G.; formal analysis, M.G.; data curation, M.G.; writing—original draft preparation, M.G.; writing—review and editing, N.X. and Z.G.; supervision, M.G. and Z.G.

Funding

This work was partly supported by the Youth Innovation Promotion Association of CAS (2016195) and National Natural Science Foundation of China (31570423).

Conflicts of Interest

The authors declare no conflict of interest.

References

- [1] Zhang, Y.C.; Rossow, W.B.. Estimating meridional energy transports by the atmospheric and oceanic general circulations using boundary fluxes. *J. Clim.*, 1997, 10: 2358–2373.
- [2] Chang, E.K.M.; Lee, S.; Swanson, K.L.. Storm track dynamics. *J. Clim.*, 2002, 15: 2163–2183.
- [3] Ulbrich, U.; Leckebusch, G.C.; Pinto, J.G.. Extra-tropical cyclones in the present and future climate: a review. *Theor. Appl. Climatol.*, 2009, 96: 117–131.
- [4] Catto, J.L.. Extratropical cyclone classification and its use in climate studies. *Rev. Geophys.*, 2016, 54: 486–520.
- [5] Hawcroft, M.K.; Shaffrey, L.C.; Hodges, K.I.; Dacre, H.F.. How much Northern Hemisphere precipitation is associated with extratropical cyclones? *Geophys. Res. Lett.*, 2012, 39: L24809.
- [6] Wang, X.L.; Feng, Y.; Chan, R.; Isaac, V.. Inter-comparison of extra-tropical cyclone activity in nine reanalysis datasets. *Atmos. Res.*, 2016, 181: 133–153.
- [7] Wang, X.L.; Feng, Y.; Compo, G.P.; Swail, V.R.; Zwiers, F.W.; Allan, R.J.; Sardeshmukh, P.D.. Trends and low frequency variability of extra-tropical cyclone activity in the ensemble of twentieth century reanalysis. *Clim. Dyn.*, 2013, 40: 2775–2800.
- [8] Wang, X.L.; Swail, V.R.; Zwiers, F.W.. Climatology and changes of extratropical cyclone activity: comparison of ERA-40 with NCEP–NCAR reanalysis for 1958–2001. *J. Clim.*, 2006, 19: 3145–3166.
- [9] Yoshida, A.; Asuma, Y.. Structures and environment of explosively developing extratropical cyclones in the northwestern Pacific region. *Mon. Weather Rev.*, 2004, 132: 1121–1142.
- [10] Sinclair, M.R.. Objective Identification of Cyclones and Their Circulation Intensity, and Climatology. *Weather Forecast.*, 1997, 12: 595–612.
- [11] Reitan, C.H.. Frequencies of cyclones and cyclogenesis for North America, 1951–1970. *Mon. Wea. Rev.*, 1974, 102: 861–868.
- [12] Zishka, K.M.; Smith, P.J.. The climatology of cyclones and anticyclones over North America and surrounding ocean environs for January and July, 1950–1977. *Mon. Wea. Rev.*, 1980, 108: 387–401.
- [13] Lambert, S. J.. A cyclone climatology of the Canadian climate centre general circulation model. *J. Clim.*, 1988, 1: 109–115.
- [14] Hodges, K.I.. A general method for tracking analysis and its application to meteorological data. *Mon. Wea. Rev.*, 1994, 122: 2573–2586.
- [15] Haak, U.; Ulbrich, U.. Verification of an objective cyclone climatology for the North Atlantic. *Meteor. Z.*, 1996, 5: 24–30.
- [16] Pinto, J.G.; Spanghel, T.; Ulbrich U., et al.. Sensitivities of a cyclone detection and tracking algorithm: Individual tracks and climatology. *Meteor. Z.*, 2005, 14: 823–838.
- [17] Flaounas, E.; Kotroni, V.; Lagouvardos, K.; Flaounas, I.. CycloTRACK (v1.0) – tracking winter extratropical cyclones based on relative vorticity: sensitivity to data filtering and other relevant parameters. *Geosci. Model Dev.*, 2014, 7: 1841–1853
- [18] Gaffney, S.J.; Robertson, A.W.; Smyth, P.; Camargo, S.J.; Ghil, M.. Probabilistic clustering of extratropical cyclones using regression mixture models. *Clim. Dyn.*, 2007, 29: 423–440.
- [19] Yang, F.; Wu, G.; Du, Y.; Zhao, X.. Trajectory data mining via cluster analyses for tropical cyclones that affect the South China Sea. *ISPRS Int. J. Geo-Inf.*, 2017, 6: 210.
- [20] Camargo, S.J.; Robertson, A.W.; Gaffney, S.J.; Smyth, P.; Ghil, M.. Cluster analysis of typhoon tracks. Part I: general properties. *J. Clim.*, 2007, 20: 3635–3653.
- [21] Catalano, A.J.; Broccoli, A.J.. Synoptic Characteristics of surge-producing extratropical cyclones along the Northeast Coast of the United States. *J. Appl.*

- Meteor. Climatol., 2018, 57: 171-184.
- [22] Chen, S.J.; Kuo, Y.H.; Zhang, P.Z.; Bai, Q.F.. Climatology of explosive cyclones off the east Asian coast. *Mon. Weather Rev.*, 1992, 120: 3029–3035.
- [23] Zhang, J.; Xu, H.; Ma, J.; Deng, J.. Interannual variability of spring extratropical cyclones over the Yellow, Bohai, and East China Seas and possible causes. *Atmosphere*, 2019, 10: 40.
- [24] Yao, S.; Zhang, Y.; Zhou, T.. Climatic characteristics of extratropical cyclone frequency and its variations over East Asia during recent 50 years in spring. *J. Nanjing Institute of Meteorology*, 2003, 26: 317–323. (in Chinese with English Abstract)
- [25] Qin, T.; Wei, L.X.. The statistic and variance of cyclones entering coastal waters of China in 1979-2012. *Chin. Acta Oceanol. Sin.*, 2015, 37: 43–52.
- [26] Zhang, Y.X.; Ding, Y.H.; Li, Q.P.. A climatology of extratropical cyclones over East Asia during 1958–2001. *Acta Oceanol. Sin.*, 2012, 26(3): 261–277.
- [27] Dee, D.P.; Uppala, S.M.; Simmons, A.J.; Berrisford, P.; Poli, P.; Kobayashi, S.; Andrae, U.; Balmaseda, M.A.; Balsamo, G.; Bauer, P.; et al.. The ERA-Interim reanalysis: configuration and performance of the data assimilation system. *Q. J. R. Meteorol. Soc.*, 2011, 137: 553–597.
- [28] Loikith, P.C.; Lintner, B.R.; Sweeney, A.. Characterizing large-scale meteorological patterns and associated temperature and precipitation extremes over the northwestern United States using self-organizing maps. *J. Clim.*, 2017, 30: 2829-2847.
- [29] Wang, X.; Zhai, P.; Wang, C.. Variations in extratropical cyclone activity in northern East Asia. *Adv. Atmos. Sci.*, 2009, 26(3): 471–479.
- [30] Zhu, Q.; Lin, J.; Shou, S.; et al.. Principles of Synoptic Meteorology. China Meteorological Press: Beijing, China, 2000: 133–143. (in Chinese)
- [31] Sanders, F.; Gyakum, J.R.. Synoptic-dynamic climatology of the “Bomb”. *Mon. Weather Rev.*, 1980, 108: 1589–1606.
- [32] Hodges, K.I.; Hoskins, B.J.; Boyle, J.; Thorncroft, C.. A comparison of recent reanalysis datasets using objective feature tracking: Storm tracks and tropical easterly waves. *Mon. Wea. Rev.*, 2003, 131: 2012–2037.
- [33] Rudeva, I.; Gulev, S.K.. Composite analysis of North Atlantic extratropical cyclones in NCEP–NCAR reanalysis Data. *Mon. Wea. Rev.*, 2011, 139: 1419–1446.
- [34] Simmons, A.J.; Hoskins, B.J.. The life cycles of some nonlinear baroclinic waves. *J. Atmos. Sci.*, 1978, 35: 414-432.



REVIEW

Exploration and Research on Fault Maintenance System of New Generation Weather Radar

Haitao Yan*

Meteorological Bureau of Tai'an, Tai'an, Shandong, 271000, China

ARTICLE INFO

Article history

Received: 19 February 2019

Accepted: 25 February 2019

Published Online: 12 April 2019

Keywords:

New Generation Weather Radar

Fault

Maintenance System

Exploration and Research

ABSTRACT

In order to improve the standardization, specialization, intelligence and timeliness of the new generation weather radar fault repair, the technical threshold of radar fault repair is greatly reduced, so that the general operators can carry out radar fault repair work. In order to achieve this goal, this paper designs a new generation weather radar fault repair system, which aims to solve two problems: one is to solve the causes and locations of the new generation weather radar faults which can be quickly and accurately detected and diagnosed[1]; the other is to solve the problem that the grass-roots radar operational staff are inexperienced in maintenance and will not be repaired, and to provide visual through the maintenance system. Maintenance methods and steps with expert intelligence level [2], so that general radar operators can operate radar fault repair according to video steps, and have the technical level of maintenance experts, to achieve breakthroughs in technical difficulties of radar fault repair, to achieve both disease detection and treatment effect, to improve the efficiency of the use of new generation weather radar and to achieve modern technical equipment support. Chemistry plays an important role and significance.

Classification Number of Chinese Map: P415.2

Document identification code: A

1. Introduction

The sudden change of wind and cloud generally indicates that there will be rapid and intense weather changes. To effectively deal with the unexpected weather, advanced technology and equipment should be used as support. The advanced equipment for dealing with short-term severe convective weather in meteorology should belong to the new generation weather radar. It can monitor and detect the sudden short-term severe convective weather system and grasp its development and change

trend in real time. The internal condition and intensity of the severe convective weather system are continuously tracked and detected to provide reliable basis for forecasting, early warning and disaster prevention. However, all of these are based on the function that the new generation weather radar can play in the absence of faults and normal operation. Long-term operation of machinery and equipment will always lead to faults. Finding the causes of faults, rapid positioning and timely repairing are very important safeguards. The existing fault self-checking system of the new generation weather radar has been

*Corresponding Author:

Haitao Yan,

Meteorological Bureau of Tai'an, Tai'an, Shandong, 271000, China;

Email: 617849141@qq.com

running for more than ten years, and its technology and functions have been improved. At present, there are two difficulties in the rapid diagnosis and timely maintenance of the new generation weather radar faults. One is that the existing self-inspection system of the new generation weather radar faults urgently needs to be updated, perfected, supplemented and upgraded. The other is that the new generation weather radar fault repair technology requires a high threshold and lacks one to provide technical support for timely repair. Standardized and intellectualized maintenance system can greatly reduce the technical barrier of maintenance, so that when the new generation weather radar breaks down, it can not only quickly detect the location and determine the cause of the breakdown, but also have the ability to eliminate the breakdown in time and quickly restore the normal working state of the radar. This research is to develop a standardized and intellectualized maintenance step that can provide visual function. The maintenance system plays an important role in ensuring the normal operation of radar and realizing the modernization of radar.

2. The Reason Why the Troubleshooting of the New Generation Weather Radar has Become a Technical Difficulty

Fault detection and maintenance of new generation weather radar are two main reasons for technical difficulties.

2.1 Fault Detection and Diagnosis of New Generation Weather Radar

2.1.1 Fault Diagnosis Technology

Fault diagnosis is to use various inspection and testing methods to find out whether there is a fault in the system and equipment. The process of further determining the roughly location of the fault is fault location. Fault detection and fault location belong to the category of network survivability. The process of locating the fault to the replaceable product level (replaceable unit) when repairing is called fault isolation.

System fault diagnosis is to detect the system running state and abnormal situation, analyze and judge the type, location and cause of the system fault, and take the judgment results as the basis of system fault recovery, give solutions to achieve fault recovery.

2.1.2 Development of Fault Diagnosis Technology

From the end of the 19th century to the beginning of the 20th century, fault diagnosis is in its infancy. Experts in various fields depend on their senses to obtain the state

information of equipment. They also need to make direct judgments based on their own experience. This is a simple and practical method for fault diagnosis of some simple equipment. Since 1960s, due to the development and application of reliability theory and the gradual development of sensor technology, it has become easier to measure various diagnostic systems and data, especially the development of artificial intelligence technology, which makes expert intelligent system widely used in the field of fault diagnosis. This concept will gradually replace the diagnostic process, which used to be based on numerical computation and signal processing, with knowledge processing and knowledge reasoning as its core. At present, intelligent diagnosis technology has become a new direction of the current development of diagnosis technology. The development of modern fault diagnosis technology has formed a new comprehensive subject of "fault diagnosis", and fault diagnosis has also produced a variety of classification methods, and each has its own characteristics.

2.1.3 Fault Diagnosis Method

At present, the mature and effective fault diagnosis methods are: fault tree analysis and diagnosis method, diagnosis method based on fuzzy theory, diagnosis method based on statistical theory, expert system fault diagnosis method, neural network fault diagnosis method, data fusion fault diagnosis method and integration technology fault diagnosis method, and each has its own advantages and disadvantages. The most suitable fault diagnosis method can be selected according to the characteristics of equipment. A combined fault diagnosis method.

Expert system diagnosis method is one of the most noticeable development directions in the field of fault diagnosis. It is also a kind of intelligent diagnosis technology with the most research and application. It has roughly gone through two stages of development: the fault diagnosis system based on expert experience knowledge in shallow knowledge field and the fault diagnosis system based on model knowledge of deep knowledge diagnosis object.

2.1.4 Current Fault Detection System of New Generation Weather Radar

The new generation weather radar fault self-detection system has been in use for more than ten years. It is developed and set up by professionals according to the common fault cases that appeared or may appear in the past, but it has not been fully supplemented, improved and upgraded. At present, fault detection technology and fault analysis and diagnosis technology have made great prog-

ress, and the existing new generation weather radar equipment gradually shows aging fatigue, and the failure rate gradually increases. After that, although some high-level weather radar personnel and maintenance personnel have studied several new generation weather radar fault self-detection and diagnosis schemes, they have not been popularized and applied. Both technology and function need to be upgraded in order to provide more effective basis and guarantee for the new generation weather radar to maintain normal use and fault repair.

2.2 Weather Radar Fault Maintenance

The new generation weather radar is a fusion of multidisciplinary advanced technology products. The technical threshold of radar fault maintenance is very high. It is necessary to master a variety of technical knowledge and rich maintenance practice experience to be competent. Most of the existing radar operators only carry out single-disciplinary systematic learning and training. Daily duty and simple faults can be dealt with without docking knowledge. There are too many points, too many blind areas, many radar attendants are not familiar with the internal structure and components of the radar, and they have never seen what the components of any specifications look like. Even if the weather radar fault location and causes are found out by the self-inspection system, they will not repair it. Most radar operators do not even know the sequence and steps of the fault repair and installation, and improper disposal may cause greater damage, and stations are often damaged. Because of the absence of maintenance personnel when the radar fails, it will delay the rush repair time, affect the radar observation work, greatly limit the timeliness of the repair of radar failures, and also affect the efficiency of the new generation weather radar. At present, radar maintenance is basically divided into station level, provincial level and manufacturer level.

The existing fault self-detection system of new generation weather radar is no longer suitable for the needs of radar operation, and it also needs to be updated, perfected, supplemented and upgraded urgently. Especially the existing radar fault self-examination system is only responsible for seeing a doctor, regardless of the treatment, even the prescription is not opened, which allows the radar watchman who is not proficient in maintenance to watch the observation period slip past in front of his eyes, sweating on his head and anxious in his heart. At present, the grassroots radar station lacks an expert intelligent maintenance system which can automatically provide general radar operators with fault information and guide fault maintenance after fault location and causes are diagnosed by fault self-inspection system when weather radar fails.

3. Solutions of Difficulties in Fault Maintenance of New Generation Weather Radar

3.1 Solution of the Fault Detection Shortcomings and Diagnosis of New Generation Weather Radar

The existing new generation weather radar fault self-detection system has been used for more than ten years. In order to better integrate with the new generation weather radar fault self-detection system, the existing radar fault self-detection system can be optimized, upgraded, and its old appearance can be changed. In order to improve the ability of fault detection, analysis and diagnosis for the new generation weather radar, more advanced system and equipment self-inspection analysis and diagnosis methods are selected to be used in combination, so as to provide accurate location and cause for the maintenance of weather radar faults in time, and to improve the accuracy and timeliness of diagnosis.

To adapt to the requirements of new weather radar fault detection technology, the existing database of new generation weather radar fault cases is reformed, perfected, supplemented and upgraded.

3.2 Maintenance Method for Solving Fault of New Generation Weather Radar

Strengthen the relevant technical training of the new generation weather radar operators, accumulate experience, gradually improve their familiarity with each part of the new generation weather radar system and equipment, and improve the operational level and response ability of radar fault maintenance.

If we want to achieve the timely and rapid repair of the new generation weather radar faults, we should try to reduce the technical threshold of radar fault maintenance. We can research and develop an advanced expert intelligent system for fault maintenance of the new generation weather radar. This system can automatically select the optimal maintenance scheme according to the fault information of the radar fault self-examination system. Provides, realizes the self-inspection system to find out the fault has the corresponding repair plan, and provides the radar fault repair plan to enable the general business personnel to understand, according to this plan everybody can carry on the fault repair, it should be the visual version of the maintenance plan with maintenance steps and maintenance tools and the required accessories physical image, this plan must have the maintenance expert level, and according to According to the fault repair plan, everyone can repair, which will change the current state of only responsible for seeing a doctor, regardless of treatment, so

that the new generation of weather radar fault repair problems can be solved.

4. Design Scheme of Fault Maintenance System for New Generation Weather Radar

The new generation weather radar fault maintenance system consists of two subsystems: radar fault detection subsystem and radar fault maintenance subsystem.

4.1 Fault Detection Subsystem of New Generation Weather Radar

New generation weather radar fault detection subsystem^[3], including radar monitor and radar fault detection device, radar monitor is connected with fault signal input interface circuit and operation state input interface. Radar monitor will acquire weather radar fault signal from fault signal input interface circuit and weather radar operation state signal from operation state input interface circuit. The signal is transmitted to the radar fault detection device.

Radar fault detection device, including the first processor, the first memory and the first remote communication device, the first processor is connected with the first memory^[4], the first remote communication device; the first processor is used to query the fault location and fault of weather radar according to the weather radar fault signal transmitted by the radar monitor and the weather radar operation status signal in the first memory. The technical parameters of the cause are diagnosed by expert intelligent system^[5], and the weather radar fault information is transmitted to the first memory to store and send out alarm signals. The weather radar fault information includes weather radar fault signal, weather radar operational status signal, fault location and fault cause diagnosis results of weather radar; the radar fault detection device will process the first one. The weather radar fault information inquired by the device is transmitted to the radar fault maintenance subsystem through the first remote communication device.

4.2 Fault Maintenance Subsystem of New Generation Weather Radar

The new generation weather radar fault maintenance subsystem includes the second processor, the second memory, the second remote communication device and the display. The second processor is connected with the second memory, the second remote communication device and the display. The second processor receives the weather radar fault information transmitted by the first remote communication device through the second remote communication device. The second processor also receives the weather radar fault information transmitted by the first remote

communication device according to the second processor. The weather radar fault information received by the second remote communication device is searched in the second memory according to the radar fault information for the corresponding radar maintenance scheme, from which intelligent optimal screening is carried out, and the selected radar maintenance scheme and steps are pushed to the staff through the display to display and store, thus realizing the function of automatic analysis, search and screening the corresponding maintenance scheme, and also realizing the radar. Maintenance system is standardized, intelligent and professional.

4.3 Working Principle of Fault Maintenance System for New Generation Weather Radar

Working Principle of New Generation Weather Radar Fault Maintenance System (see Figure 1): When weather radar fails or runs abnormally, the radar monitor of Weather Radar Fault Detection Subsystem starts. It will acquire the weather radar fault signal from the fault signal input interface circuit and the weather radar running status signal from the runtime input interface circuit to the radar. The first processor of the radar fault detection device inquires the technical parameters of the weather radar fault location in the first memory according to the weather radar fault signal transmitted by the radar monitor and the weather radar operation status signal, and compares them. The expert intelligent system is used to diagnose the fault location and the fault reason diagnosis results are stored and sent out. The alarm signal can automatically supplement and update the weather radar fault information system in the first memory. At the same time, the radar fault detection device transmits the above results to the radar fault maintenance subsystem through the first remote communication device. After the second processor of the weather radar fault maintenance subsystem receives the weather radar fault information transmitted by the first remote communication device through the second remote communication device, it inquires the fault maintenance scheme according to the radar fault information in the second memory, and intelligently optimizes the best scheme from the fault maintenance subsystem, and visualizes the fault maintenance scheme and steps to the staff through the display. Push display and storage. Radar operators carry out fault repair according to the maintenance scheme of the radar fault maintenance system. After repair, the fault detection system is retested. If other faults are not repaired, the maintenance system provides a new scheme again, and then repairs until the weather radar resumes normal work.

The new generation weather radar fault overhaul sys-

tem realizes the functions of automatic detection, fault diagnosis, automatic case storage, alarm and automatic pushing visual radar fault repair schemes and procedures to the staff. It also realizes the automatic supplement and improvement of radar fault overhaul system, which makes the system standardized, intelligent and professional, and guarantees the realization of the system. Modernization plays an important role in promoting development.

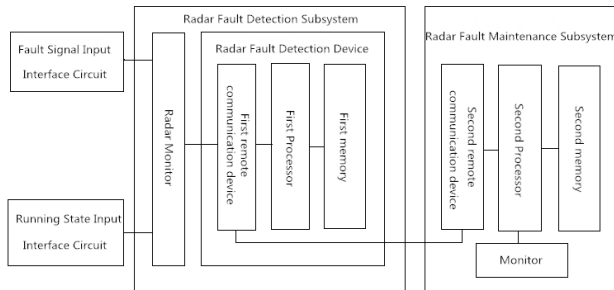


Figure 1. Icon Schematic diagram of fault maintenance system for new generation weather radar

5. Conclusion

The most prominent feature of the new generation weather radar fault overhaul system is that the system automatically provides the visual step maintenance plan according to the fault detection and diagnosis results. In the maintenance plan, the required tools, spare parts parameters and physical images are provided with visual images, and the scheme provided has the level of experts, which can greatly reduce the requirements of maintenance work for professional maintenance technology and experience. Threshold improves the timeliness of the new generation weather radar fault repair, and correspondingly improves the normal operation efficiency of the new generation weather radar.

The existing fault self-detection system of the new generation weather radar is no longer suitable for the needs of radar operation, and it also needs to be updated, perfected, supplemented and upgraded urgently. Especially the existing radar fault self-detection system has the characteristics of "only responsible for seeing a doctor, regardless of treatment", and cannot provide the corresponding repair methods. When the radar malfunction is also diagnosed the location and cause, which makes the radar watchman who is not proficient in maintenance, watching the observation period slip by in front of his eyes, sweating on his head and anxious in his heart. The establishment and application of the new generation weather radar fault repair

system is conducive to strengthening the standardization, intellectualism and specialization of the new generation weather radar fault repair, and can achieve the effect of both seeing a doctor and treating a disease.

The new generation weather radar fault overhaul system has the function of expert intelligence system and self-supplementing, perfecting and upgrading case plan database, which improves the reliability, security and advancement of the system itself.

For the first complex new faults, new causes and solutions, the new generation weather radar fault overhaul system will carry out intelligent fitting analysis selection and expert scheme comparison and optimization input. The system will also automatically supplement and upgrade, Self-Summarize and accumulate experience, in order to achieve intelligent self-improvement mechanism, so as to maintain the new generation weather radar fault overhaul system has always been specialized. Home level.

The new generation weather radar fault overhaul system has an innovative design scheme which can automatically provide visual function. It also needs to select enough pilot units to carry out operational inspection and constantly improve the system in order to provide a good technical support function for the new generation weather radar.

Reference

- [1] Xiong Guohua, Lai Weiguo. Brief Introduction of Fault Diagnosis Technology for New Generation Weather Radar [J]. Jiangxi Meteorological Science and Technology, 2001, (02): 41-44.
- [2] Liu Xiaodong, Chai Xiumei, Zhang Weiquan, et al. Technology and method of new generation weather thunder overhaul [J]. Meteorological Science and Technology, 2006, 34 (S1): 111-114.
- [3] He Jianxin. Research on testing and fault detection technology of new generation weather radar [J]. Chinese scientific and technological achievements, 2016, 17(01): 20-20.
- [4] Wang Zhiwu, Lu Xinglai, Chen Hao. Design and application of weather radar test and maintenance database [J]. Meteorological Science and Technology, 2016, 44(06): 896-901.
- [5] Bian Zhi, Jia Hankui, Kang Guihong, et al. Several fault analysis and troubleshooting methods for the new generation weather radar (CINRAD/CD) [J]. Meteorological and Environmental Science, 2010, 33 (1): 85-88.



ARTICLE

Microbial Community Diversity and Vertical Distribution in a Columnar Sediment of Maluku Strait

Yan Wang^{1,2} Fuchao Li^{2,3*} Jin Zhao^{2,3} Huaxin Chen^{2,3} Peng Jiang^{2,3} Xuexi Tang^{1*}

1. College of Marine Life Science, Ocean University of China, Qingdao 266100, China

2. Key Laboratory of Experimental Marine Biology, Institute of Oceanology, Chinese Academy of Sciences, Qingdao 266071, China

3. Laboratory for Marine Biology and Biotechnology, Qingdao National Laboratory for Marine Science and Technology, Qingdao 266071, China

ARTICLE INFO

Article history

Received: 20 March 2019

Accepted: 4 April 2019

Published Online: 12 April 2019

Keywords:

Maluku Strait

Sediment

16S rRNA

Microbial community

Spatial distribution

ABSTRACT

The sediment samples were collected from Maluku Strait at a depth of 1250 m, which is influenced by Mindanao Current and Indonesian Throughflow. Based on 16S rRNA clone libraries, the community structure and vertical distribution of archaea and bacteria were studied in a columnar sediment of 2m in length. From the surface sediment, 16S sequences were derived from fourteen bacterial phyla (Gammaproteobacteria, Planctomycetes, Alphaproteobacteria, Deltaproteobacteria were dominant), but were limited to two groups of archaea: Crenarchaeota (99%) and Euryarchaeota (1%). Besides, 90% of the archaea clones were ammonia oxidation-related which indicated that the ammonia-oxidizing archaea might make a significant contribution to the chemosynthesis in the surface sediment. Contrastively in the bottom sediment, six bacterial phylogenetic groups were obtained (Gammaproteobacteria and Firmicutes were absolutely dominant), however no archaea 16S rRNA was detected. The microbial diversity of surface sediment was much higher than the bottom and seven unique bacterial phyla were obtained from two sediment respectively. The geochemical elements analysis revealed that the content of C, TOC and S in the surface sediment was much higher than the bottom, but the content of P is contrary. The microbial communities might be in response to the geochemical substance transfer and deposit influenced by the ocean current and it deserves further study compared with the other sediment samples in this area.

*Corresponding Author:

Fuchao Li,

Key Laboratory of Experimental Marine Biology, Institute of Oceanology, Chinese Academy of Sciences, Qingdao 266071, China;
Laboratory for Marine Biology and Biotechnology, Qingdao National Laboratory for Marine Science and Technology, Qingdao 266071, China;

Email: wang_summer@126.com

Xuexi Tang,

College of Marine Life Science, Ocean University of China, Qingdao 266100, China;

Email: wang_summer@126.com

1. INTRODUCTION

The deep-sea sediments are one of the most important situations of the global nutrition and geochemical cycling. In recent years, chemical properties and biome distribution especially microbial communities at the sediment from diverse environment attracted the attention of researchers^[1,2]. The recycling of organic input into the oceanic sediments is closely related to the benthic microbial communities^[3]. Compared to the other sediments, the unique physical and chemical conditions of deep-sea sediment may result in different microbial population structure. Previous studies showed that anaerobic methanotroph Archaea (ANME-1 and ANME-2) dominate in the carbonate sediments at the methane seeps in the Black Sea^[4, 5]. Similar results have been obtained in other kind of sediments, a study about microbial community distribution of the permanently cold marine sediments showed certain characteristics which adapt them to the environment^[6]. Recently, Tamara studied jelly-like microbial mats over subsurface fields of gas hydrates at the St. Petersburg methane seep, and the chemical composition and phylogenetic structure of the microbial community showed that the life activity of the mat occurs because of methane and its derivatives involved^[7]. Besides, deep-sea sediments are formed by the deposition year by year, so spatial distribution should be taken into consideration to know how the environment shapes community structure. A research about the spatial structure of the microbial community in sandy carbonate sediment of Hawaii suggested that the microbial community structure was correlated to local physico-chemical conditions in the sediment and that spatio-temporally heterogeneous redox conditions resulted in an increased microbial diversity^[8]. As the depths increase, the structure of the microbial community structure also changes. Due to the opaque and no dissolved oxygen in the sediment, microbial diversity of the bottom sediment declined rapidly but certain phyla may increase^[9]. This means that even at the same sites, particular depths make the microbial structure different which let the vertical comparison be significant. Above researches help us to know the relationship between organisms and environment in the deep sea where we studied little before.

We choose the Maluku Strait as the research object has certain reasons. Area of 30.7 square kilometers, with a series of trench basin and ridge, the depth of the water in Maluku Strait is about 1000-2000 meters. The deepest area of the water in the southeast is 4970 meters. As reported, a magnitude 7.5 earthquake erupted on 21th January, 2007 in Maluku Strait (01°12' N, 126°30' E) where is very close to the sample collection site (02°00' N,

126°14' E). Furthermore, the velocity of flowing current in Maluku Strait is fast which means that rich nutrient will be brought here. Influenced by the Mindanao Current and Indonesian Throughflow (ITF), seawater of the Maluku Strait is the mixture of upper thermocline circulation originate from the North Pacific and low thermocline circulation originate from the South Pacific^[10]. The Mindanao Current carried with the nutrients from the North Equatorial Current (NEC) is mixed with terrigenous water forming the mixing deposits which may shape the distinctive microbial communities. To our knowledge, the spatial structure of microbial communities of the sediment in the Maluku Strait has not been studied especially in relation to biogeochemistry. The dominant archaea and bacterial phylogenetic groups are still unknown. Above all, we focus on this area and believe that special microbial structure and environmental factors may be observed.

The objective of this study was to examine vertical variation in microbial community in relation to the environmental factors. So in this study, we chose the surface and bottom layer of a two meters depth columnar sediment in Maluku Strait as the samples. Variations in the distribution of archaea and bacterial communities in different layers will play a vital role in the further research like functional genes study and the mechanism of deep-sea organisms adapted to the environment.

2. Materials and Methods

2.1 Sample Collection

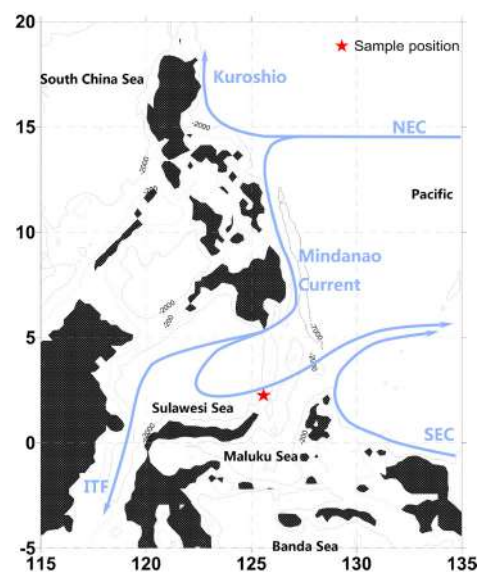


Figure1. Sample position and current information in Maluku Sea. NEC: North Equatorial Current. SEC: South Equatorial Current. ITF: Indonesian Throughflow

The sediment samples were collected from Maluku Strait

(02°00' N, 126°14' E) at a depth of 1250 m (Figure1) during the cruise of physical oceanography research by RV KEXUE YI HAO from November to December, 2012. Sediment samples were stored at -80 °C for DNA extractions and 16S rRNA gene amplification. We took both ends of the two meters columnar sediments which were named U for the surface layer and D for the bottom layer.

2.2 Geochemical Analysis

Granularity and elements (C, TOC, N, P, S, Fe, Co, Ni) content of two sediment samples (U and D) were determined by the Analysis and Testing Center in the Institute of oceanology, Chinese Academy of Sciences. Granularity is measured by C11as-940 Laser Particulate Size Description Analyser (USA). The elements (P, Fe, Co, Ni) and (C, TOC, P, S) content was determined by the Optima 7300DV Inductively Coupled Plasma Atomic Emission Spectrometer (ICP-AES) (USA) and Vanio MACRO Elemental Analyser (GER) separately.

2.3 Total DNA Extractions, PCR Amplification and Sequencing

Environmental DNA from the samples was extracted from the two samples using the MoBio PowerSoil™ DNA kit (MoBio, USA). The DNA was used as a template in PCR that contains modified 27F/1390R bacterial and A21F/A958R archaea primer pairs as previously described^[11, 12]. PCR was carried out using respective environmental DNA templates, EasyTaq DNA polymerase (TransGen, China), 10×EasyTaq Buffer (Mg²⁺), dNTP, primers 27F (5'-AGA GTT TGA TCA TGG CTC AG-3'), 1390R (5'-ACG GGC GGT GTC TAC AA-3') or A21F (5'-TTC CGG TTG ATC CYG CCG GA-3'), A958R(5'-YCC GGC GTT GAM TCC AAT T-3') and the following program: 94 °C (5 min), followed by 30cycles of 94 °C (1 min), 56 °C for bacteria or 61.5°C for archaea (1min), 72 °C (1 min) and a 10-min extension step at 72 °C. Through connection and conversion, the 16S rRNA gene clone libraries of archaea and bacteria were constructed respectively. They are named as UA (archaea 16S rRNA gene clone library of the surface layer), UB (bacterial 16s rRNA gene clone library of the surface sediment) and DB (bacterial 16s rRNA gene clone library of the bottom sediment).

2.4 Sequences Analysis

All 16S rRNA gene sequences were checked for possible chimeric artifact using Bellerophon (available http://greengenes.lbl.gov/cgi-bin/nph-bel3_interface.cgi) and the chimeric sequences were not included in the following analysis. Operational taxonomic units (OTUs) were gen-

erated by using the MOTHUR program at 97% sequence similarity cut off for archaea and bacteria respectively as previously described^[13]. Basic diversity estimates including Shannon-Wiener index and Chao 1 estimator were calculated for each sample. The Shannon-Wiener diversity index (H')^[14] was calculated according to the equation $H' = -\sum(\pi_i)(\ln\pi_i)$, where π_i was the number of ribotypes in each operational taxonomic unit (OTU) group, as defined by 97% similarity, divided by the total number of ribotypes in each library. Non-parametric Chao1 estimator^[15] was calculated using the MOTHUR program^[13]. To study the differences between individual groups of OTUs, the representative sequences were subjected to phylogenetic analysis. Archaea and bacterial phylogenetic trees of the two samples were respectively constructed from the resulting distance matrix by the NJ method with the MEGA 4 package^[16]. BLASTN similarities of all sequences were determined by NCBI nucleotide database search.

3. Results

3.1 Environmental Factors

The content of elements and granularity (Table1) was obtained to find out the compositions of the sediment and the chemical differences between the surface (U) and the bottom (D) sediment. The content of C, TOC and S in the U is much higher than D, but the content of P is contrary. Metallic elements like Fe, Co and Ni are on the normal level in contrast to the other marine sediment^[17,18,19]. The surface sediment is clayed silt (6% of sand, 71% of silt and 23% of clay) while the bottom sediment is silt (3% of sand, 78% of silt and 19% of clay)^[20].

Table1. Chemistry of the surface (U) and bottom (D) sediment

Content	U	D
C(mg/g)	18.02	26.35
TOC(mg/g)	2.25	4.23
N(mg/g)	1.08	1.04
P(mg/g)	0.23	0.14
S(mg/g)	3.30	10.02
Fe(mg/g)	20.03	20.40
Co(mg/g)	0.018	0.019
Ni(mg/g)	0.063	0.078
granularity	Clayed silt	Silt

3.2 Clone Libraries and Diversity Analysis

An archaea 16S rRNA gene clone library (UA) and two bacterial 16S rRNA gene clone libraries (UB and DB)

were constructed (Table 2). 74,207 and 130 clones which belong to 22, 162 and 21 OTUs (defined by 97% similarity) were obtained from UA, UB and DB. The Shannon and Chao1 estimators of UB shows the highest diversity among the three clone libraries, and rarefaction curves (Figure 2) of the UB did not reach a plateau while the UA and DB did. All the sequences were deposited in the GenBank database with the accession numbers KM454184-KM454205 for archaea and KM454206-KM454388 for Bacteria.

Table 2. Description of the 16S rRNA gene libraries and diversity estimators

Clone library	Category	Sequenced clones	OTUs	Shannon index	Chao1 estimator
UA	Archaea	74	22	2.76	36
UB	Bacteria	207	162	4.95	1142
DB	Bacteria	130	21	1.68	77

Note: All the 16S rRNA gene libraries were constructed except DA because no archaea 16S rRNA gene was detected in the bottom sediment.

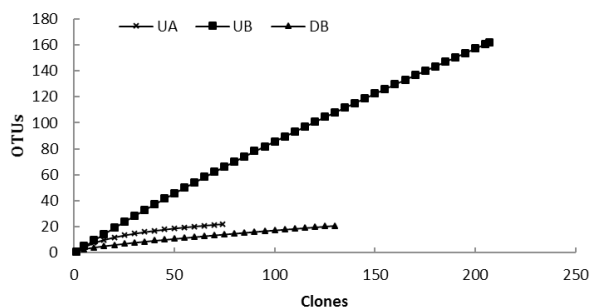


Figure 2. Rarefaction curves calculated at evolutionary distance of 3% of the three 16S rRNA gene clone libraries. UA: archaea 16s rRNA gene clone library of the surface sediment (U). UB: bacterial 16s rRNA gene clone library of the surface sediment (U). DB: bacterial 16s rRNA gene clone library of the bottom sediment (D)

3.3 Phylogenetic Analysis of Archaea

16S rRNA gene of archaea was amplified only in the surface sediment but no one was detected in the bottom layer of the columnar sediment. Only one clone library of 74 sequences from the UA was constructed. All the sequences fell into 22 OTUs uniformly. With the phylogenetic analysis (Figure 3), twenty-two unique OTUs representing two phyla: Crenarchaeota (99%) and Euryarchaeota (1%). Although all the sequences lacked cultivated representatives in the database, *Nitrosopumilales* (Crenarchaeota)-related sequences constituted a major fraction (90%) of the library, which suggested the oxidation of ammonia into nitrite was performed in the surface sediment. BLASTN analysis showed 52 sequences were most closely related

(99% gene identity) to the uncultured *Nitrosopumilales* archaeon (EF069366) (Figure 3). According to the previous research, two ammonia-oxidizing archaea [21], *Nitrosopumilus maritimus* and *Nitrososphaera viennensis*, have been isolated and described [22]. Ammonia-oxidizing archaea dominate in both soils and marine environments [23] which suggesting that Crenarchaeota may be a greater contributor to ammonia oxidation in these environments. Moreover, five sequences (UA-90, UA-24, UA-12, UA-77, UA-97) showed maximum identity of 97% to the sequences which were already deposited in the GenBank database (Figure 3). On the contrary, no archaea 16S gene clone obtained from sample D showed that the archaea richness in the bottom was much lower than the surface sediment.

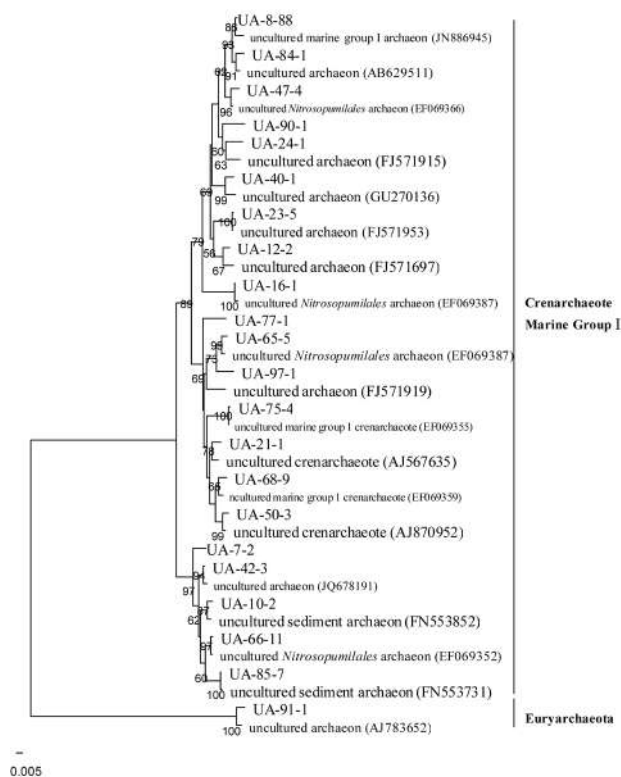


Figure 3. Phylogenetic affiliation of 16S rRNA sequences received from the surface sediment related to the Archaea

3.4 Phylogenetic Analysis of Bacteria

The 207 sequences and 130 sequences was obtained from the surface (U) and the bottom (D) sediment. 162 unique OTUs were retrieved from 207 sequences from the UB clone library and one of the OTUs represents 140 sequences. All the sequences fell into the following phyla (Figure 4a): Gammaproteobacteria (16%), Planctomycetes (15%), Alphaproteobacteria (14%), Deltaproteobacteria (13%), Bacteroidetes (8%), Acidobacteria (8%), Chlorof-

lexi (7%), Actinobacteria (6%), Gemmatimonadetes (5%), Nitrospira (3%), Verrucomicrobia (2%), Betaproteobacteria (1%), Elusimicrobium (1%) and unclassified phylum. Twenty-one unique OTUs were obtained from 130 sequences from the DB clone library and 65 sequences belonged to a unique OTU. Firmicutes (53%) and Gammaproteobacteria (32%) were dominant in the assemblage (Figure 4b) which also included four unclassified sequences. According to the phylogenetic analysis of the total bacterial sequences from the U and D sediment, we figured out the dominant phyla. All the sequences were affiliated with fourteen phyla (Figure 5). Comparing the bacterial community structure of UB to DB, the diversity of the UB is much higher than DB and we find out that Deltaproteobacteria, Bacteroidetes, Acidobacteria, Actinobacteria, Gemmatimonadetes, Nitrospira, Verrucomicrobia, Elusimicrobium are only obtained from the surface sediment, whereas, Firmicutes from the bottom sediment is unique (Figure 4c).

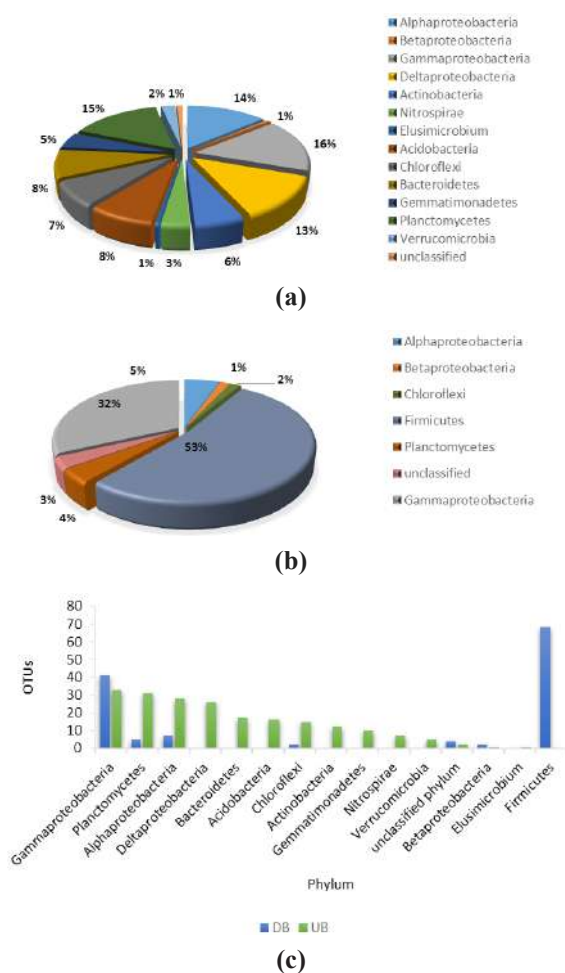


Figure 4. Taxonomical classification

Note: (a) bacterial 16S rRNA gene library clones of U (UB) (n=207, 162OTUs); (b) bacterial 16S rRNA gene library clones of D (DB) (n=130, 21OTUs); (c) Comparison of bacterial community structure of UB and DB

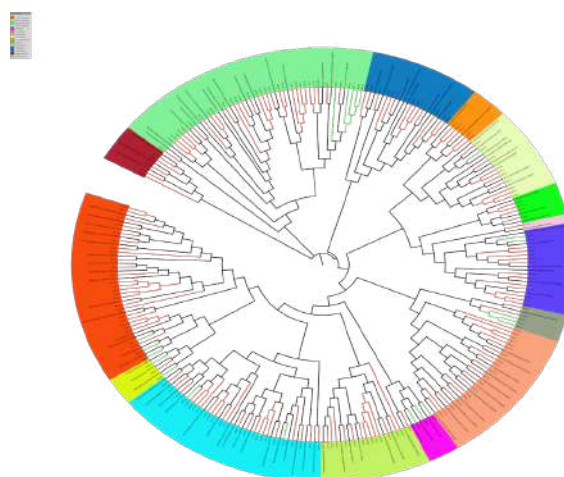


Figure 5. Phylogenetic affiliation of 16S rRNA sequences received from the surface (UB) and bottom (DB) sediment related to the Bacteria.

Note: The green clades and red clades are sequences from the UB and DB clone library. The black clades are reference sequences. Different color ranges represent different phyla. In a clockwise direction, Verrucomicrobia, Planctomycetes, Bacteroidetes, Gemmatimonadetes, Actinobacteria, Nitrospira, Elusimicrobium, Chloroflexi, unclassified, Acidobacteria, Firmicutes, Deltaproteobacteria, Alphaproteobacteria, Betaproteobacteria, Gammaproteobacteria were shown successively.

4. Discussion

4.1 Archaea Diversity

Members of archaea phylogenetic group are rarely cultured so that we can only infer that they might play a special role in anoxic metabolism. Only one of the uncultured sequence is affiliated to the Euryarchaeota and most of them fall into Marine Group I: Crenarchaeota (Figure 3). The Crenarchaeota is a well-defined branch of the archaeal domain and abundant form of all known Archaea, as they occupy several different habitats and ecological niches [24]. Usually, Group I Crenarchaeota is the most widely distributed archaea community and this area is no exception. Overall, the diversity of archaea communities obtained from the sediment especially the bottom layer is lower than the other marine sediment [25,26] and 90% of the archaea sequences from UA clone library are most related to ammonia-oxidizing archaea which indicate that the activities of ammonia oxidation may make a significant contribution to the chemosynthesis. Along with the distribution of the bacterial phylum (Nitrospira) which play a role in the nitrite oxidation process, we infer that the cycle of nitrogen is active in the sediment especially in the surface layer. In our data, the distribution of archaea might

reflect different physical and chemical factors in different sediment layer such as anaerobic conditions, elements content and different granularity. The result that archaea 16S rRNA is not detected in the bottom sediment (Table.2) may be due to the low amount of archaeal DNA, leaving part of groups under detection as a result of the limitation of the research methods and phylogenetic analysis. But this procedure has been employed successfully as a sensitive tool for the spatial gradients in surface water^[2] and marine sediments. Lack of further evidence, no archaea harbors in the bottom sediment cannot be concluded but this results shows that archaea diversity in this layer is extremely low at the very least.

4.2 Bacterial Diversity

Low archaea diversity but high bacterial diversity (Figure 2) is the remarkable microbial characteristics of the surface sediment. Crenarchaeota is the absolute archaea dominant phylum while the sequences related to the bacteria fall into the diverse phyla, indicating that the surface sediment in this area harbors a distinctive microbial community. The most frequently derived sequences in this study belong to Gammaproteobacteria clustered in different groups which are widely distributed in the surface and the bottom sediment (Figure4c). Planctomycetes, Alphaproteobacteria and Chloroflexi are the other widespread phyla in both surface and bottom sediments following Gammaproteobacteria. From the UB clone library, 60% of the sequences which have the maximum identity to Deltaproteobacteria (dominant group) are related to the organic compounds degradation and iron and sulfur cycling in the sediment^[27,28]. All the sequences affiliated with the phylum Nitrospira are related to the nitrification. Nitrification is the oxidation of ammonia to nitrite by the ammonia-oxidizing archaea and bacteria mentioned before and oxidation of the nitrite to nitrate by bacteria in the genus *Nitrospira*. *Nitrospira* is part of a nitrification process which is important in the biogeochemical nitrogen cycle. Furthermore, it is deserved to mention that three of the sequences affiliated with the phylum Verrucomicrobia only have the 90% maximum identity to the sequences deposited. In the DB clone library, sequences related to the unique phylum Firmicutes (dominant group) have the 99% maximum identity to *Staphylococcus hominis*^[29], *Bacillus subtilis subsp. inaquosorum*^[30] and *Bacillus aquimaris*^[31] which are dominant species. Above all, we can conclude that special bacterial communities inhabit in the surface and bottom sediment respectively. Compared with the two sediment samples, intense changes have been observed in microbial community in virtue of the variation in the composition of the bacterial phyla and the dominant groups.

This will be a vital basis to the further research.

4.3 Microbial Community Structure Related to the Environmental Factors

With the results of environmental factors, the relation between environment and microbial communities have been found. These unique phyla like Deltaproteobacteria and Bacteroidetes from the surface sediment are mostly composed with organic compounds degradation-related sequences which may be the reason that TOC content in the surface is much lower than the bottom (Table.1). Like *Desulfatibacillum alkenivorans* AK-01 is a deltaproteobacterium capable of utilizing C13-C18 alkanes as growth substrates (So and Young, 1999). In the bottom sediment, Firmicutes (53% in the DB clone library) is the dominant phylogenetic group (Figure4b) though there is much lower heterogeneity. Most sequences affiliated with Firmicutes are related to *Bacillus aquimaris*, indicating a wide distribution in the bottom sediment. *Bacillus aquimaris* which were derived from seawater and deep-sea sediments before can utilize diverse kinds of carbon sources^[31] which match the high content of carbon in the bottom sediment (Table.1). Combining the results of the microbial community and environmental factors, biology is specific to the environment is proved again and this will provide important clues to find functional genes from deep-sea microorganisms.

5. Conclusion

Based on the findings of this study, we have the first insight into the marine sediments in the Maluku Strait and study microbial community structure in relation to biogeochemistry. This is just primary research but the foundation to the further studies. Later, research of functional genes and the mechanism of deep-sea organisms adapted to the environment is deserved which can help us to take a step forward toward the deep-sea sediment.

6. Acknowledgements

We would like to thank Dr. Zheng Wang at Institute of Oceanology, Chinese Academy of Sciences to provide the ocean current information. This work was supported by the Strategic Priority Research Program of the Chinese Academy of Sciences (XDA11030404), the National High Technology Research and Development Program of China (2012AA092103), National Natural Science Foundation of China (31300365), the Knowledge Innovation Project of the Chinese Academy of Sciences (KZCX2-YW-JC201), the Open Project Program of the Key Laboratory of Marine Bio-resources Sustainable Utilization, SCSIO,

CAS (LMB121006), and the Scientific and Technological Innovation Project financially supported by Qingdao National Laboratory for Marine Science and Technology (2015ASKJ02).

References

- [1] Schwarz JI, Eckert W, Conrad R.. Community structure of Archaea and Bacteria in a profundal lake sediment Lake Kinneret (Israel). *Syst Appl Microbiol.*, 2007, 30: 239-254.
- [2] Gao Z, Wang X, Hannides AK, Sansone FJ, Wang G.. Impact of redox-stratification on the diversity and distribution of bacterial communities in sandy reef sediments in a microcosm. *Chinese Journal of Oceanology and Limnology*, 2011, 29: 1209-1223.
- [3] Aller RC, Hall POJ, Rude PD, Allera JY.. Biogeochemical heterogeneity and suboxic diagenesis in hemipelagic sediments of the Panama Basin. *Deep-Sea Res.*, 1998, 45:133–165.
- [4] Lein AY, Ivanov MV, Pimenov NV, Gulin MB.. Geochemical characteristics of the carbonate constructions formed during microbial oxidation of methane under anaerobic conditions. *Microbiology*, 2002, 71:89–103.
- [5] Treude T, Orphan V, Knittel K, Gieseke A, House CH, Boetius A.. Consumption of methane and CO₂ by methanotrophic microbial mats from gas seeps of the anoxic Black Sea. *Appl Environ Microbiol*, 2007, 73:2271–2283.
- [6] Teske A, Durbin A, Ziervogel K, Cox C, Arnosti C.. Microbial community composition and function in permanently cold seawater and sediments from an arctic fjord of svalbard. *Appl Environ Microbiol*, 2011, 77: 2008-2018.
- [7] Tamara IZ, Anna VL, Olga VS, Tatiana VP, Igor VM, Svetlana MC, Tatiana YS, Olegm K, Alexander VE.. Jelly-like microbial mats over subsurface fields of gas hydrates at the St. Petersburg methane seep (Central Baikal). *Geomicrobiology Journal*, 2015, 32: 89–100.
- [8] Ketil BS, Brian G, Angelos H, Eric G.. Spatial structure of the microbial community in sandy carbonate sediment. *Marine Ecology Progress Series*, 2007, 346:61-74.
- [9] Sørensen KB, Glazer B, Hannides A, Gaidos E.. Spatial structure of the microbial community in sandy carbonate sediment. *Marine Ecology Progress Series*, 2007, 346: 61-74.
- [10] Du Y, Fang G.. Progress on the study of the Indonesian Seas and Indonesian Throughflow. *Advances in Earth Science*, 2011, 26: 1131-1142.
- [11] Li XR, Du B, Fu HX, Wang RF, Shi JH, Wang Y, Mike SMJ, Quan ZX.. The bacterial diversity in an anaerobic ammonium-oxidizing (anammox) reactor community. *Syst Appl Microbiol.*, 2009, 32: 278-289.
- [12] Delong EF.. Archaea in coastal marine environments. *P Natl Acad Sci USA.*, 1992, 89: 5685-5689.
- [13] Youssef NH, Couger MB, Elshahed MS.. Fine-scale bacterial beta diversity within a complex ecosystem (Zodletone Spring, OK, USA): the role of the rare biosphere. *PLoS One.*, 2010, 5: e12414.
- [14] Li YX, Li FC, Zhang XW, Qin S, Zeng ZG, Dang HY, Qin YS.. Vertical distribution of bacterial and archaeal communities along discrete layers of a deep-sea cold sediment sample at the East Pacific Rise (~13°N). *Extremophiles*, 2008, 12:573-585.
- [15] Chao A.. Nonparametric-estimation of the number of classes in a population. *Scand j Stat.*, 1984, 11: 265-270.
- [16] Tamura K, Dudley J, Nei M, Kumar S.. MEGA4: Molecular Evolutionary Genetics Analysis (MEGA) software version 4.0. *Mol Biol Evol*, 2007, 24: 1596-1599.
- [17] Xu Z, Li A, Jiang F, Meng Q, Liu J.. Characteristics and origin of the new-type ferromanganese crusts from deepwater areas of the east Philippine Sea. *Marine Geology & Quaternary Geology*, 2006, 26: 91-98.
- [18] Fang X, Shi X, Wang K, Cheng Z, Wang X.. Geochemical characteristics of surficial sediment elements from the sea area east of the Ryukyu Islands. *Advances in Marine Science*, 2006, 24: 9-16.
- [19] Lv R, Zhu M, Li T, Yang G, Deng F.. Speciation of solid-phase iron in mud sediments collected from the shelf of the East China Sea: Constraints on diagenetic pathways of organic matter, iron, and sulfur. *Geochimica*, 2011, 40: 363-371.
- [20] Shepard F P.. Nomenclature based on sand-silt-clay ratios. *Journal of Sedimentary Petrology*, 1954, 24: 151-158.
- [21] Treusch AH, Leininger S, Kletzin A, Schuster SC, Klenk HP, Schleper C.. Novel genes for nitrite reductase and Amo-related proteins indicate a role of uncultivated mesophilic crenarchaeota in nitrogen cycling. *Environ Microbiol*, 2005, 7: 1985-1995.
- [22] Martens-Habbena W, Berube PM, Urakawa H, de la Torre JR, Stahl DA.. Ammonia oxidation kinetics determine niche separation of nitrifying Archaea and Bacteria. *Nature*, 2009, 461: 976-979.
- [23] Leininger S, Urich T, Schlöter M, Schwark L, Qi J, Nicol GW, Prosser JI, Schuster SC, Schleper C.. Archaea predominate among ammonia-oxidizing pro-

- karyotes in soils. *Nature*, 2006, 442: 806-809.
- [24] Lysnes K, Thorseth IH, Steinsbu BO, Ovreas L, Torsvik T, Pedersen RB.. Microbial community diversity in seafloor basalt from the Arctic spreading ridges. *FEMS Microbiol Ecol.*, 2004, 50: 213-230.
- [25] Wang P, Xiao X, Wang F.. Phylogenetic analysis of Archaea in the deep-sea sediments of west Pacific Warm Pool. *Extremophiles*, 2005, 9: 209-217.
- [26] Vetriani C, Jannasch HW, MacGregor BJ, Stahl DA, Reysenbach AL.. Population structure and phylogenetic characterization of marine benthic Archaea in deep-sea sediments. *Appl Environ Microbiol*, 1999, 65: 4375-4384.
- [27] Cravo-Laureau C, Matheron R, Jouliau C, Cayol JL, Hirschler-Rea A.. *Desulfatibacillum alkenivorans* sp. nov., a novel n-alkene-degrading, sulfate-reducing bacterium, and emended description of the genus *Desulfatibacillum*. *Int J Syst Evol Microbiol.*, 2004, 54: 1639-1642.
- [28] Reichenbach H, Lang E, Schumann P, Sproer C.. *Byssovorax cruenta* gen. nov., sp. nov., nom. rev., a cellulose-degrading myxobacterium: rediscovery of 'Myxococcus cruentus' Thaxter 1897. *Int J Syst Evol Microbiol.*, 2006, 56: 2357-2363.
- [29] Shah MM, Iihara H, Noda M, Song SX, Nhung PH, Ohkusu K, Kawamura Y, Ezaki T.. DnaJ gene sequence-based assay for species identification and phylogenetic grouping in the genus *Staphylococcus*. *Int J Syst Evol Microbiol.*, 2007, 57: 25-30.
- [30] Rooney AP, Price NP, Ehrhardt C, Swezey JL, Bannan JD.. Phylogeny and molecular taxonomy of the *Bacillus subtilis* species complex and description of *Bacillus subtilis* subsp. *inaquosorum* subsp. nov. *Int J Syst Evol Microbiol.*, 2009, 59: 2429-2436.
- [31] Yoon JH.. *Bacillus marisflavi* sp. nov. and *Bacillus aquimaris* sp. nov., isolated from sea water of a tidal flat of the Yellow Sea in Korea. *Int J Syst Evol Microbiol.*, 2003, 53: 1297-1303.

Author Guidelines

This document provides some guidelines to authors for submission in order to work towards a seamless submission process. While complete adherence to the following guidelines is not enforced, authors should note that following through with the guidelines will be helpful in expediting the copyediting and proofreading processes, and allow for improved readability during the review process.

I . Format

- Program: Microsoft Word (preferred)
- Font: Times New Roman
- Size: 12
- Style: Normal
- Paragraph: Justified
- Required Documents

II . Cover Letter

All articles should include a cover letter as a separate document.

The cover letter should include:

- Names and affiliation of author(s)

The corresponding author should be identified.

Eg. Department, University, Province/City/State, Postal Code, Country

- A brief description of the novelty and importance of the findings detailed in the paper

Declaration

v Conflict of Interest

Examples of conflicts of interest include (but are not limited to):

- Research grants
- Honoria
- Employment or consultation
- Project sponsors
- Author's position on advisory boards or board of directors/management relationships
- Multiple affiliation
- Other financial relationships/support
- Informed Consent

This section confirms that written consent was obtained from all participants prior to the study.

- Ethical Approval

Eg. The paper received the ethical approval of XXX Ethics Committee.

- Trial Registration

Eg. Name of Trial Registry: Trial Registration Number

- Contributorship

The role(s) that each author undertook should be reflected in this section. This section affirms that each credited author has had a significant contribution to the article.

1. Main Manuscript

2. Reference List

3. Supplementary Data/Information

Supplementary figures, small tables, text etc.

As supplementary data/information is not copyedited/proofread, kindly ensure that the section is free from errors, and is presented clearly.

III. Abstract

A general introduction to the research topic of the paper should be provided, along with a brief summary of its main results and implications. Kindly ensure the abstract is self-contained and remains readable to a wider audience. The abstract should also be kept to a maximum of 200 words.

Authors should also include 5-8 keywords after the abstract, separated by a semi-colon, avoiding the words already used in the title of the article.

Abstract and keywords should be reflected as font size 14.

IV. Title

The title should not exceed 50 words. Authors are encouraged to keep their titles succinct and relevant.

Titles should be reflected as font size 26, and in bold type.

IV. Section Headings

Section headings, sub-headings, and sub-subheadings should be differentiated by font size.

Section Headings: Font size 22, bold type

Sub-Headings: Font size 16, bold type

Sub-Subheadings: Font size 14, bold type

Main Manuscript Outline

V. Introduction

The introduction should highlight the significance of the research conducted, in particular, in relation to current state of research in the field. A clear research objective should be conveyed within a single sentence.

VI. Methodology/Methods

In this section, the methods used to obtain the results in the paper should be clearly elucidated. This allows readers to be able to replicate the study in the future. Authors should ensure that any references made to other research or experiments should be clearly cited.

VII. Results

In this section, the results of experiments conducted should be detailed. The results should not be discussed at length in

this section. Alternatively, Results and Discussion can also be combined to a single section.

VIII. Discussion

In this section, the results of the experiments conducted can be discussed in detail. Authors should discuss the direct and indirect implications of their findings, and also discuss if the results obtain reflect the current state of research in the field. Applications for the research should be discussed in this section. Suggestions for future research can also be discussed in this section.

IX. Conclusion

This section offers closure for the paper. An effective conclusion will need to sum up the principal findings of the papers, and its implications for further research.

X. References

References should be included as a separate page from the main manuscript. For parts of the manuscript that have referenced a particular source, a superscript (ie. [x]) should be included next to the referenced text.

[x] refers to the allocated number of the source under the Reference List (eg. [1], [2], [3])

In the References section, the corresponding source should be referenced as:

[x] Author(s). Article Title [Publication Type]. Journal Name, Vol. No., Issue No.: Page numbers. (DOI number)

XI. Glossary of Publication Type

J = Journal/Magazine

M = Monograph/Book

C = (Article) Collection

D = Dissertation/Thesis

P = Patent

S = Standards

N = Newspapers

R = Reports

Kindly note that the order of appearance of the referenced source should follow its order of appearance in the main manuscript.

Graphs, Figures, Tables, and Equations

Graphs, figures and tables should be labelled closely below it and aligned to the center. Each data presentation type should be labelled as Graph, Figure, or Table, and its sequence should be in running order, separate from each other.

Equations should be aligned to the left, and numbered with in running order with its number in parenthesis (aligned right).

XII. Others

Conflicts of interest, acknowledgements, and publication ethics should also be declared in the final version of the manuscript. Instructions have been provided as its counterpart under Cover Letter.



**BILINGUAL
PUBLISHING CO.**
Pioneer of Global Academics SINCE 1984

Journal of Atmospheric Science Research

Aims and Scope

Journal of Atmospheric Science Research publishes original research papers that offers a rapid review and publication that freely disseminates research findings in areas of Remote Sensing, Weather Extremes, Air Pollution, Satellite Meteorology and more. The Journal focuses on innovations of research methods at all stages and is committed to providing theoretical and practical experience for all those who are involved in these fields.

Journal of Atmospheric Science Research aims to discover innovative methods, theories and studies in all aspects of Atmospheric Science by publishing original articles, case studies and comprehensive reviews.

The scope of the papers in this journal includes, but is not limited to:

- Remote Sensing
- Climate Dynamics
- Air Chemistry
- Hydrological Cycle
- Satellite Meteorology
- Ocean Dynamics
- Climate Change
- Weather Extremes
- Air Pollution
- Weather and Climate Prediction
- Climate Variability

Bilingual Publishing Co. (BPC)

Tel:+65 65881289

E-mail:contact@bilpublishing.com

Website:www.bilpublishing.com

About the Publisher

Bilingual Publishing Co(BPC) is an international publisher of online, open access and scholarly peer-reviewed journals covering a wide range of academic disciplines including science, technology, medicine, engineering, education and social science. Reflecting the latest research from a broad sweep of subjects, our content is accessible worldwide – both in print and online.

BPC aims to provide an analytics as well as platform for information exchange and discussion that help organizations and professionals in advancing society for the betterment of mankind. SP hopes to be indexed by well-known databases in order to expand its reach to the science community, and eventually grow to be a reputable publisher recognized by scholars and researchers around the world.

BPC adopts the Open Journal Systems, see on <http://ojs.s-p.sg>

Database Inclusion



National Library, Singapore



Asia & Pacific area Science Citation Index



China National Knowledge Infrastructure



Creative Commons



Google Scholar



Crossref



J-Gate



My Science Work

National Library of Singapore

NLB manages the National Library, 26 Public Libraries and the National Archives.

NLB promotes reading, learning and information literacy by providing a trusted, accessible and globally-connected library and information service through the National Library and a comprehensive network of Public Libraries. By forging strategic partnerships to cultivate knowledge sharing, the libraries also encourage appreciation and awareness of Singapore's history through their wide range of programmes and collection on Singapore and regional content. The National Archives of Singapore oversees the collection, preservation and management of public and private archival records, including government files, private memoirs, maps, photographs, oral history interviews and audio-visual materials.

Established on 1 September 1995 as a statutory board, NLB is an agency under the Ministry of Communications and Information (MCI).



Bilingual Publishing Co. is a company registered in Singapore in 1984, whose office is at 12 Eu Tong Sen Street, #08-169, Singapore 059819, enjoying a high reputation in Southeast Asian countries, even around the world.

Tel: +65 65881289
E-mail: contact@bilpublishing.com
Website: www.bilpublishing.com



**BILINGUAL
PUBLISHING CO.**
Pioneer of Global Academics Since 1984

